MSc thesis in Civil Engineering

Computational Homogenisation for Delamination in Composite Laminates

Pascalle Essed

2024

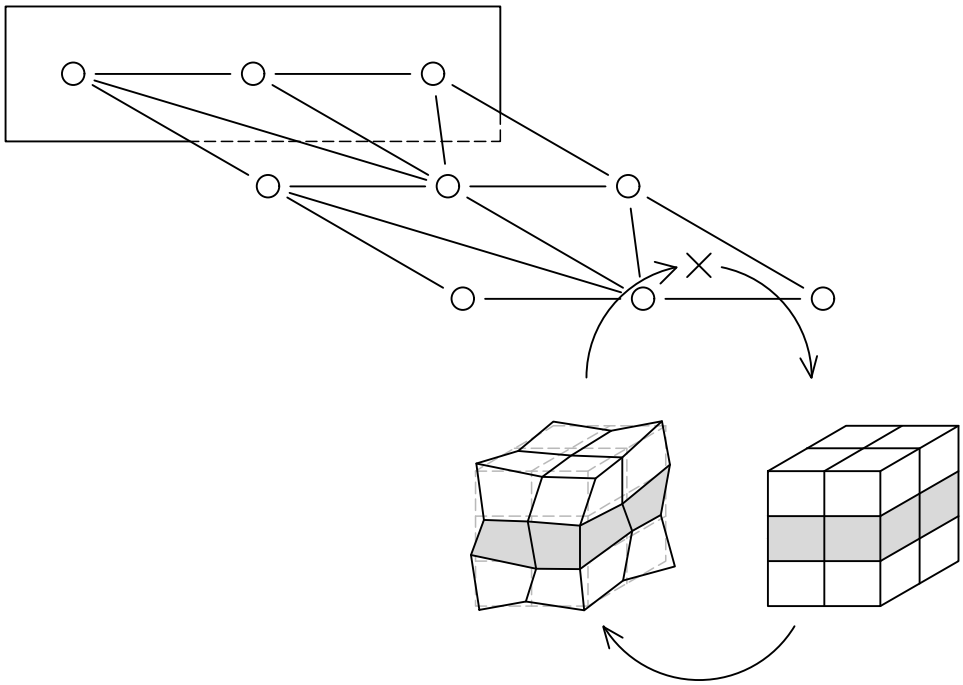

TU Delft

MSc thesis in Civil Engineering

Computational Homogenisation for Delamination in Composite Laminates

Pascalle Essed

January 2024

A thesis submitted to the Delft University of Technology in partial fulfillment of the requirements for the degree of Master of Science in Civil Engineering

Pascalle Essed: *Computational Homogenisation for Delamination in Composite Laminates* (2024)
An electronic version of this thesis is available at http://repository.tudelft.nl/.

The work in this thesis was carried out in the:

Computational Mechanics Group
Delft University of Technology

and

Department of Naval & Offshore Structures
TNO

Chair:	Prof.dr.ir. F.P. van der Meer
Supervisors:	Dr.ir. I.B.C.M. Rocha
	Dr.ir. J.H.A. Schipperen
Co-reader:	Dr. B. Chen

Abstract

Military vehicles are often subjected to dynamic loads from mines. To protect these vehicles, steel plating underneath the vehicle is applied. However, these steel plates can be quite heavy, resulting in a slower vehicle. *Composite laminates*, however, are much lighter and also prove to be capable of protecting these vehicles from mines.

During an explosion, the energy released from the blast will be absorbed by the composite material. This often results in the *delamination* of plies within the laminate. Due to the delamination, bending loads will be taken over by membrane loads. This is proven advantageous for composite materials as they are stronger in membrane loading.

Unfortunately, modelling sizeable composite structures with a *Direct Numerical Simulation* (DNS) requires the use of a lot of elements. This, in turn, results in long computational times, particularly for non-linear analyses. *Multiscale modelling* is a possible solution to this problem.

This study explores the method of *Computational Homogenisation* for delamination in composite laminates as an alternative to 3D DNS modelling. Two-dimensional *Shell-Interface-Shell elements* (SIFS elements) are introduced on the *macroscale*. These double-layered shell elements consist of two stacked Mindlin-Reissner shell elements with an interface element connecting the two shells. Each integration point of a SIFS element is linked to a *mesoscopic* 3D *coupled Representative Volume Element* (cRVE), which is also split into two shells with an interface in between. By applying linear and periodic boundary conditions that incorporate the macroscopic strains on the cRVE, mesoscopic stresses are determined, leading to macroscopic stresses and the macroscopic stiffness matrix.

The proposed multiscale framework is validated by a set of load cases with different ply configurations. The results are then compared to those of a 3D DNS. The multiscale framework performs reasonably well; however, it is not without its limitations.

Firstly, the cRVE exhibits width dependence, requiring the implementation of a sufficiently narrow cRVE for accurate results. Additionally, SIFS elements may lack kinematic consistency with 3D solid elements, constraining certain deformations and resulting in overly stiff responses for SIFS analyses. The proposed multiscale framework might not perform as accurately as the 3D DNS in specific load cases, one of which is explored in this work.

Returning to the original goal of this work for the multiscale model, certain extensions still need to be implemented to design composite laminates for blast protection. Implementation of the arc-length method will provide insight into snapback behaviour that could occur during loading. Next, the macroscale and mesoscale models need to be adapted for multiple delaminations over the height of a laminate. Furthermore, the implementation of dynamic loading is a necessary step, as blast loads induce strong dynamic behaviour. Finally, the integration of Artificial Intelligence / Machine Learning into the framework could improve the model by further reducing computational time.

Acknowledgements

This thesis would not have been possible without the help of certain individuals to whom I'd like to express my gratitude.

Firstly, I'd like to thank my thesis committee. My heartfelt gratitude goes out to Frans for your invaluable role in introducing me to the intricate realm of computational mechanics. I wanted a thesis topic with FEM and programming applications, and that's exactly what I got when I asked you if there were any assignments available with these applications.

Special thanks go to Iuri, my daily supervisor at the TU, and Ingrid, my daily supervisor at TNO.

Iuri, thank you for challenging me with difficult questions at every meeting we had. Our meetings always pushed me to think further and more critically.

Ingrid, my sincere thanks for your assistance in processing and interpreting results with me. Your insights significantly contributed to the clarity and depth of my findings.

Lastly, Boyang, we haven't had much contact as you took on the role of co-reader right before my Greenlight meeting; however, your thoughtful engagement and valuable feedback during the meeting certainly elevated the overall quality of my work.

I would also like to thank the people of the Department of Naval & Offshore Structures at TNO. I very much enjoyed working alongside you in the office. You certainly made my time working on this thesis more enjoyable.

Next, I'd like to thank my families, both on Aruba and in Hoogvliet, for their steadfast support. Your unwavering belief in my capabilities has been a constant motivator throughout this academic journey.

Finally, I extend my deepest gratitude to my family at home, Max and Archie, for providing the necessary distractions that offered moments of respite. Your love and understanding have been indispensable in maintaining balance during the challenges of thesis completion.

Contents

List of Figures

List of Tables

1. Introduction

1.1. Background

During warfare, a common method to disable military vehicles involves the use of mines. For the protection of these vehicles and their occupants, blast protection mechanisms, typically in the form of steel plates, are strategically placed underneath the vehicle [11, 17]. The primary objective of these steel plates is to mitigate the impact of the blast by undergoing plastic deformation, thereby absorbing the released energy. However, this defensive measure can still result in severe physical injury to the individuals within the vehicle. Additionally, the substantial weight of these steel plates contributes to diminished vehicle speed and fuel efficiency. Consequently, more lightweight, energy-absorbing materials are considered for these plates [4].

Among the potential alternatives, composite laminates show good energy-absorbing behaviour. Often, the energy from a blast is absorbed by a failure mechanism known as *delamination*. Delamination occurs when a force in the material tears two plies apart, see Figure 1.1. This separation can manifest in various modes, namely in the normal direction (Mode-I: opening), in a tangent direction due to either a sliding shear load (Mode-II: in-plane shear) or a tearing shear load (Mode-III: out-of-plane shear), or a combination of the normal and transverse modes (Mixed-Mode). When delamination occurs, a single shell will be torn into two (or more) shells on top of each other. Where first bending stresses were dominant, membrane stresses will take over. This is ideal for composite laminates because composites exhibit greater strength in membrane loading compared to bending due to the fibres within the material.

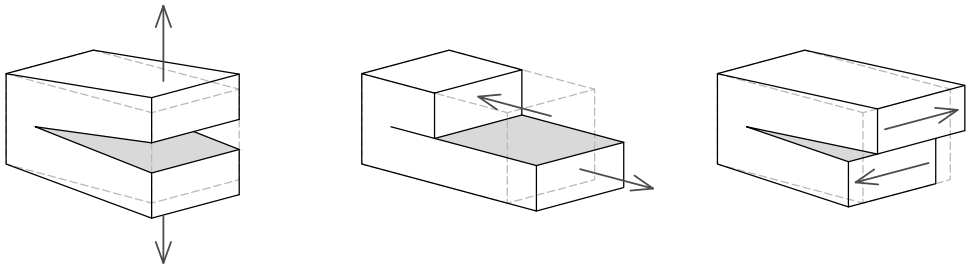

Figure 1.1.: Delamination modes of composite laminates

When it comes to composite laminates, a distinction can be made between three scales, see Figure 1.2. At the highest level is the *macroscale*, which consists of the entire layup of

the structure, known as a laminate. The macroscale is often used when analysing large composite structures. Although, at this scale, failure can be included, delaminations cannot. Descending to a finer scale, the *mesoscale* is characterised by the individual layers, or plies, that form the structure. These layers can be defined by the orientation at which the plies are set. Here, delamination can be described. Lastly, there's the *microscale*, which entails the fibres and the matrix of the composite.

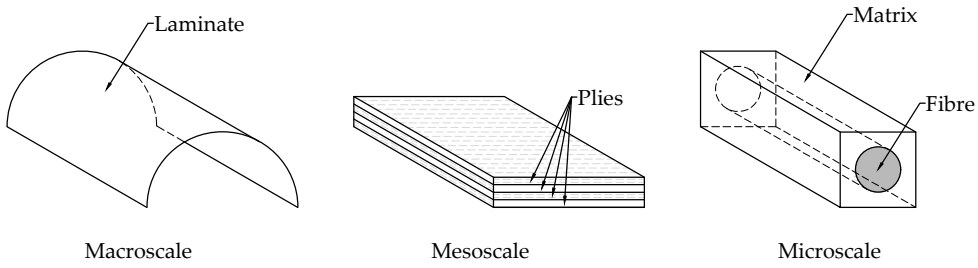

Figure 1.2.: Three-scale approach to composite laminates, adapted from [21]

The intricate composition of matrix and fibres in composite laminates contributes to the material's classification as highly complex. Additionally, due to its recent emergence, a complete comprehension of the material is still undergoing development. Besides delamination, multiple other failure mechanisms can be identified for composite laminates, such as matrix cracking, fibre breakage, and fibre-matrix debonding. Unfortunately, traditional numerical modelling techniques for simulating such failures demand substantial time and computational resources. Addressing delaminations in composite laminates necessitates modelling each individual ply at the mesoscale. Furthermore, to properly capture the variations in stress, strain, and deformations, multiple elements are necessary through the thickness of a structure. This approach, however, can be very computationally intensive.

A different approach is to analyse mesoscopic plies on the macroscale by applying shell elements, for which the material model utilises a through-thickness integration of the material to account for the different plies and their offset from the shell's midplane [18, 6]. However, the complex intricacies of the microscale are not captured by this approach. Delamination, in turn, can be accounted for by applying interface elements between shell elements.

A relatively new alternative approach to simulate failure in heterogeneous materials such as composite laminates is to implement a *multiscale framework* in a finite element analysis. By applying a multiscale framework, computational time can be greatly reduced while still accurately capturing the complexities of the material on the lower scales. The implementation of the multiscale framework allows for analyses of multiple failure mechanisms of composite laminates on the different scales that can be evaluated on the macroscale [12]. Additionally, the multiscale framework shows promising prospects for combining multiphysics analyses on these different scales [19]. The implementation of delamination in a multiscale framework is, however, not yet fully understood. Combining the properties of the different scales in analyses can give a more comprehensive understanding of the mate-

rial. Therefore, this thesis will investigate the application of a multiscale framework for the modelling of delaminations in composite laminates.

The multiscale framework in this thesis will couple 3D *Representative Volume Elements*, or RVEs, of the mesoscale of a composite laminate to Mindlin-Reissner shell elements of the macroscale to include delamination at the macroscale without explicit modelling of that delamination at that scale. This thesis is carried out as a continuation of Wieringa's master thesis [23], where 2D RVEs are coupled to Timoshenko beam elements.

1.2. Research Goal

As mentioned in Section 1.1, this work is a continuation of Wieringa's thesis [23]. Wieringa's thesis describes a number of steps to reach the research goal, which is "to develop a numerical analysis tool for designing blast protectors made out of composite laminates". These steps are updated for this work in Figure 1.3.

The first step, which is including delamination in a multiscale framework, is implemented in Wieringa's thesis. 2D isotropic plane stress elements are coupled to 1D Timoshenko beam elements, and a single delamination interface is introduced in the RVEs.

This work will focus on the second step, which is to extend the framework to a 2D-3D coupling and add the composite ply material models. 3D solid elements will be coupled to 2D Mindlin-Reissner shell elements, and a material model for composite laminates consisting of orthotropic plies will be implemented in the framework. The goal of this work is to develop a multiscale finite element framework for delamination in composite laminates that performs accurately when compared to a 3D monoscale *Direct Numerical Simulation* (DNS).

To create a numerical model with a multiscale framework to simulate delaminations in composite laminates, the following three steps will be performed:

1. Computational homogenisation of shell elements with an isotropic material model
2. Computational homogenisation of shell elements with orthotropic material models
3. Inclusion of a single delamination interface over the height of the shell

To perform the numerical analyses, the Dynaflow Jem / Jive C++ libraries will be used.

The next crucial steps to achieve the research goal are to extend the model for multiple delaminations over the height of the shell and to implement dynamic loading in the framework. This will not be included in this work.

Optionally, Artificial Intelligence / Machine Learning could be introduced to the framework for further optimisation. This will also not be included in this work.

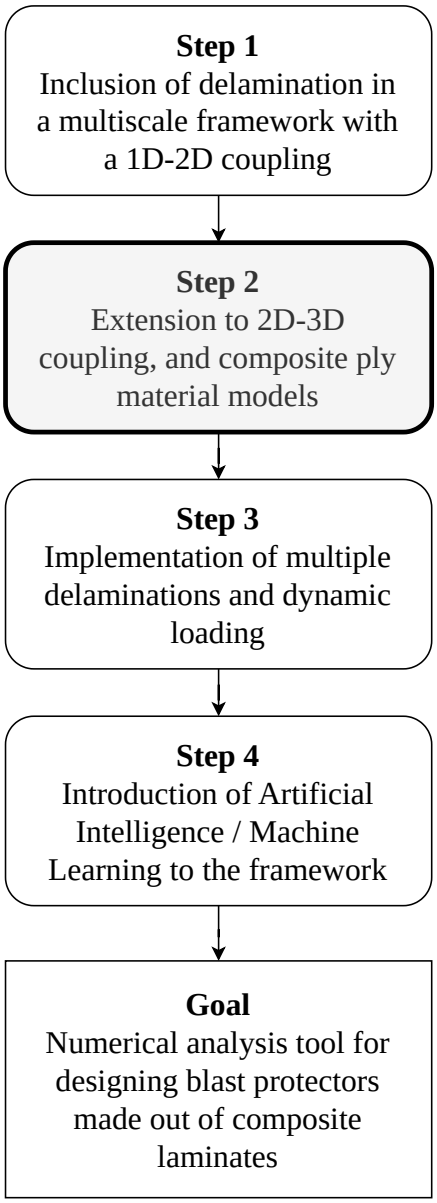

Figure 1.3.: Updated steps for designing load protectors made out of composite laminates

1.3. Thesis Outline

The rest of Chapter 1 will include a summarised literature study. Section 1.4 will contain a short explanation of the basics of the *Finite Element Method*. Section 1.5 presents the isotropic and orthotropic *material models* applied in this work. Section 1.6 is about *multiscale modelling*. Different approaches to the multiscale framework are explored. Section 1.7 will explain the modelling of the delamination according to the *discrete crack approach*.

Chapter 2 will include the first step of the methodology, where the multiscale framework will be assembled for a Mindlin-Reissner shell element. Linear elastic analyses will be performed on different load cases with an isotropic material model to verify the framework. Furthermore, mesh sensitivity and RVE width sensitivity will be analysed. The following load cases will be evaluated:

- Cantilever extension beam
- Cantilever bending beam
- Three-point bending beam

Chapter 3 will include the second step of the methodology, where the multiscale framework is assessed for RVEs with orthotropic material models. Again, mesh sensitivity and RVE width sensitivity studies will be performed, following the load cases presented in Chapter 2. The following composite ply configurations will be evaluated:

- 0
- $0/90_2/0$
- 45/-45

Chapter 4 will include the last step of the methodology, where a single delamination interface will be added to the multiscale framework on the mesoscale. The macroscale will also have to be expanded with double-layered *Shell-Interface-Shell* elements to simulate the cracking. The framework will first be analysed for Unit Tests with an isotropic material model and compared to analytical results. Next, the following load cases will be evaluated for both an isotropic material model and different ply configurations with orthotropic material models:

- Double-cantilever beam
- End-notched flexure
- Single-leg bending

Chapter 5 will test the multiscale framework on a Double-Cantilever Beam Test conform to the standards of ASTM [2]. Following additional sensitivity studies in Appendix A, the Double-Cantilever Beam will be discretized. The results of the DCB Test following the multiscale framework will be compared to the results of a 3D DNS analysis.

Lastly, Chapter 6 will include the conclusion and future perspectives for the framework.

1.4. The Finite Element Method

The *Finite Element Method* (FEM) is a numerical analysis method where an equilibrium equation for a field problem is solved. The field is discretized into a finite number of elements, hence the name.

The basic principles behind FEM are summarised by Van der Meer [21]. In the case of a static or quasi-static displacement field analysis, a force equilibrium needs to be solved, where the internal force in a body has to be equal to the external force applied to the body:

$$\mathbf{f}^{int} = \mathbf{f}^{ext} \tag{1.1}$$

Together with a set of boundary conditions, which describe the prescribed displacements (*Dirichlet boundary conditions*) and applied loads (*Neumann boundary conditions*), the force equilibrium can be solved.

As mentioned, the field problem is split into a number of elements, which are defined by nodes with coordinates $\mathbf{x}$. These nodes have a set of degrees of freedom, which will express the solution to the field problem. By applying *interpolation functions*, or *shape functions* $\mathbf{N_e}(\mathbf{x})$, the degrees of freedom of the element, $\mathbf{u_e}(\mathbf{x})$, can be described with the degrees of freedom of the nodes, or the nodal displacements $\mathbf{a_e}$:

$$\mathbf{u_e}(\mathbf{x}) = \mathbf{N_e}(\mathbf{x})\mathbf{a_e} \tag{1.2}$$

For a 3D solid model, $\mathbf{x}$, $\mathbf{u_e}(\mathbf{x})$, $\mathbf{N_e}(\mathbf{x})$ and $\mathbf{a_e}$ are defined as:

$$\mathbf{x} = \begin{bmatrix} x & y & z \end{bmatrix}^T \tag{1.3}$$

$$\mathbf{u_e}(\mathbf{x}) = \begin{bmatrix} u & v & w \end{bmatrix}^T \tag{1.4}$$

$$\mathbf{N_e}(\mathbf{x}) = \begin{bmatrix} N_1 & 0 & 0 & ... & N_n & 0 & 0 \\ 0 & N_1 & 0 & ... & 0 & N_n & 0 \\ 0 & 0 & N_1 & ... & 0 & 0 & N_n \end{bmatrix} \tag{1.5}$$

$$\mathbf{a_e} = \begin{bmatrix} a_1^u & a_1^v & a_1^w & ... & a_n^u & a_n^v & a_n^w \end{bmatrix}^T \tag{1.6}$$

where n corresponds to the number of nodes in the element. Following the fact that strains can be defined as the derivatives of the displacement; the strains in the element can be expressed as:

$$\boldsymbol{\epsilon_e} = \mathbf{B_e}(\mathbf{x})\mathbf{a_e} \tag{1.7}$$

$\boldsymbol{\epsilon_e}$, and $\mathbf{B_e}(\mathbf{x})$ are defined as follows for a 3D solid model:

$$\boldsymbol{\epsilon_e} = \begin{bmatrix} \epsilon_{xx} & \epsilon_{yy} & \epsilon_{zz} & 2\epsilon_{xy} & 2\epsilon_{yz} & 2\epsilon_{xz} \end{bmatrix}^T \tag{1.8}$$

and

$$\mathbf{B_e}(\mathbf{x}) = \begin{bmatrix} N_{1,x} & 0 & 0 & ... & N_{n,x} & 0 & 0 \\ 0 & N_{1,y} & 0 & ... & 0 & N_{n,y} & 0 \\ 0 & 0 & N_{1,z} & ... & 0 & 0 & N_{n,z} \\ N_{1,y} & N_{1,x} & 0 & ... & N_{n,y} & N_{n,x} & 0 \\ 0 & N_{1,z} & N_{1,y} & ... & 0 & N_{n,z} & N_{n,y} \\ N_{1,z} & 0 & N_{1,x} & ... & N_{n,z} & 0 & N_{n,x} \end{bmatrix} \tag{1.9}$$

where the subscript $,i$ denotes a derivative with respect to i. By applying *Hooke's Law* for stress and strain, $\sigma = D\epsilon$, the internal force vector of an element can be rewritten as:

$$\mathbf{f_e}^{int} = \int_{\Omega_e} \mathbf{B_e}(\mathbf{x})^T \mathbf{D} \mathbf{B_e}(\mathbf{x}) d\Omega_e \mathbf{a_e} \tag{1.10}$$

where $\mathbf{D}$ is the *material stiffness matrix* and Ω_e is the domain of the element. Furthermore, the element stiffness matrix $\mathbf{K_e}$ can be defined as:

$$\mathbf{K_e} = \int_{\Omega_e} \mathbf{B_e}(\mathbf{x})^T \mathbf{D} \mathbf{B_e}(\mathbf{x}) d\Omega_e \tag{1.11}$$

which leads to (1.10) being rewritten to:

$$\mathbf{f_e}^{int} = \mathbf{K_e} \mathbf{a_e} \tag{1.12}$$

Next, the global stiffness matrix, global displacement vector, and global (external) force vector are assembled:

$$\mathbf{K a} = \mathbf{f}^{ext} \tag{1.13}$$

Now that all the components have been derived for a static analysis, the following equation solves the unknowns of the field problem:

$$\mathbf{a} = \mathbf{K}^{-1} \mathbf{f}^{ext} \tag{1.14}$$

For a quasi-static analysis, fictional time steps, or load steps, are introduced, where in each step, there is a load increment. This is necessary to describe damage (such as delamination) in an analysis. Now, instead of applying the material stiffness matrix $\mathbf{D}$, a so-called *material tangent stiffness matrix*, or *material tangent*, $\mathbf{T}$, is applied:

$$\mathbf{T} = \frac{\partial \sigma / \partial t}{\partial \epsilon / \partial t} = \frac{\partial \sigma}{\partial \epsilon} \tag{1.15}$$

Now the material tangent $\mathbf{T}$ is applied to assemble the global tangent matrix $\mathbf{K}$, and an iterative solution procedure is used to find the solution vector:

$$\mathbf{a}_j = \mathbf{a}_{j-1} + \mathbf{K}_{j-1}^{-1} (\mathbf{f}^{ext} - \mathbf{f}^{int}(\mathbf{a}_{j-1})) \tag{1.16}$$

Equation 1.16 shows the *Newton-Raphson solution procedure* for solving the solution vector. Here, j represents an iteration. The solution procedure moves on to the next load step when a specified residual for $\mathbf{K}^{-1}(\mathbf{f}^{ext} - \mathbf{f}^{int})$ is achieved.

1.5. Material Models

In this work, both isotropic and orthotropic material models will be explored. Orthotropic material models will be applied for the plies of a composite laminate.

Following *Hooke's Law* for stress and strain, $\boldsymbol{\sigma} = \boldsymbol{D\epsilon}$, the stiffness matrices for isotropic (Equation 1.19) and orthotropic (Equation 1.21) materials can be defined with the *compliance matrix* $\mathbf{C}$ [6]:

$$\boldsymbol{\epsilon} = \mathbf{C}\boldsymbol{\sigma} \tag{1.17}$$

$$\mathbf{C}_{iso} = \frac{1}{E}\begin{bmatrix} 1 & -\nu & -\nu & 0 & 0 & 0 \\ -\nu & 1 & -\nu & 0 & 0 & 0 \\ -\nu & -\nu & 1 & 0 & 0 & 0 \\ 0 & 0 & 0 & 2(1+\nu) & 0 & 0 \\ 0 & 0 & 0 & 0 & 2(1+\nu) & 0 \\ 0 & 0 & 0 & 0 & 0 & 2(1+\nu) \end{bmatrix} \tag{1.18}$$

$$\mathbf{D}_{iso} = \mathbf{C}_{iso}^{-1} \tag{1.19}$$

$$\mathbf{C}_{ortho} = \begin{bmatrix} \frac{1}{E_1} & -\frac{\nu_{21}}{E_2} & -\frac{\nu_{31}}{E_3} & 0 & 0 & 0 \\ -\frac{\nu_{12}}{E_1} & \frac{1}{E_2} & -\frac{\nu_{32}}{E_3} & 0 & 0 & 0 \\ -\frac{\nu_{13}}{E_1} & -\frac{\nu_{23}}{E_2} & \frac{1}{E_3} & 0 & 0 & 0 \\ 0 & 0 & 0 & \frac{1}{G_{12}} & 0 & 0 \\ 0 & 0 & 0 & 0 & \frac{1}{G_{23}} & 0 \\ 0 & 0 & 0 & 0 & 0 & \frac{1}{G_{31}} \end{bmatrix} \tag{1.20}$$

$$\mathbf{D}_{ortho} = \mathbf{C}_{ortho}^{-1} \tag{1.21}$$

with

$$\boldsymbol{\epsilon} = \begin{bmatrix} \epsilon_{11} & \epsilon_{22} & \epsilon_{33} & 2\epsilon_{12} & 2\epsilon_{23} & 2\epsilon_{31} \end{bmatrix}^T \tag{1.22}$$

and

$$\boldsymbol{\sigma} = \begin{bmatrix} \sigma_{11} & \sigma_{22} & \sigma_{33} & \sigma_{12} & \sigma_{23} & \sigma_{31} \end{bmatrix}^T \tag{1.23}$$

For an isotropic material, only two material properties are necessary to define the stiffness matrix, namely the Young's modulus, E, and the Poisson's ratio, ν. For an orthotropic material, nine material properties are necessary, namely three Young's moduli, E_1, E_2, and E_3, three Poisson's ratios, ν_{12}, ν_{23}, and ν_{31} (with their respective inverses: ν_{21}, ν_{32}, and ν_{13}), and three shear moduli, G_{12}, G_{23}, and G_{31}.

Note how the stresses, strains, and material properties for the orthotropic material model are defined with numbers 1, 2, and 3 instead of directions x, y, and z. These numbers correspond to the principal direction in which the material is laid. For composite plies,

direction 1 corresponds to the direction of the fibre, direction 2 is the in-plane transverse direction of the fibre, and direction 3 is the out-of-plane transverse direction of the fibre.

A *transformation matrix*, $\boldsymbol{T}$, is necessary when the orthotropic material is laid at an angle. This transformation matrix relates the principal stresses and strains of the material to the stresses and strains in the global coordinate frame. In this work, the material will only be angled in the x-y plane. The corresponding transformation matrix can then be defined as:

$$\boldsymbol{T} = \begin{bmatrix} \cos^2\theta & \sin^2\theta & 0 & 0 & 0 & 2\sin\theta\cos\theta \\ \sin^2\theta & \cos^2\theta & 0 & 0 & 0 & -2\sin\theta\cos\theta \\ 0 & 0 & 1 & 0 & 0 & 0 \\ 0 & 0 & 0 & \cos\theta & -\sin\theta & 0 \\ 0 & 0 & 0 & \sin\theta & \cos\theta & 0 \\ -\sin\theta\cos\theta & \sin\theta\cos\theta & 0 & 0 & 0 & \cos^2\theta - \sin^2\theta \end{bmatrix} \tag{1.24}$$

where θ is the angle at which the material is laid.

By applying the transformation matrix, the material stiffness matrix can be mapped to the global coordinate system:

$$\mathbf{D}_{global} = \boldsymbol{T}^{-1}\mathbf{D}_{ortho}\boldsymbol{T}^{-T} \tag{1.25}$$

1.6. Multiscale Modelling

In the realm of multiscale modelling, diverse methodologies exist. Among these, *Concurrent Models* and *Homogenisation Techniques* stand out as widely embraced frameworks [15]. Concerning concurrent models, a direct coupling between the higher and lower scales is established. Initially, the domain is characterised by a global coarse mesh, often employing linear elastic material behaviour. Upon violation of specific scale-change criteria, the macroscopic coarse mesh is replaced by a finer mesh, representing the lower scale. This refined mesh captures the non-linear material behaviour effectively [23]. However, in the event of a delamination, the adaptation of the finer mesh throughout the model does not yield a reduction in computational time. Consequently, the homogenisation approach is employed in this study.

Homogenisation is a technique used to analyse the effective or averaged properties of a heterogeneous material at a macroscopic scale. When it comes to homogenisation, three distinct forms can be defined, namely *Analytical / Mathematical Homogenisation*, *Numerical Homogenisation*, and *Computational Homogenisation* [15]. Analytical homogenisation is typically confined to straightforward microscopic geometries and material models, rendering it unsuitable for the scope of this study. Numerical homogenisation is only applied when a precise constitutive relation can be reasonably assumed for the material undergoing homogenisation. This application is constrained, as it is not conducive to cases involving delamination, where an accurate constitutive relation is challenging to establish. Conversely, computational homogenisation serves as a viable solution in scenarios where no explicit constitutive relation can be assumed.

The works of Nguyen, Oddy and Bisschop, and Wieringa [15, 16, 23] give a good overview of the basic principles of computational homogenisation. As the name suggests, the FE^2 method involves using a nested solution procedure. Two scales are linked to compute the

stiffness matrix and stresses on the larger scale, or *macroscale*, from the subscale. As the other name suggests, the material on the subscale, the *mesoscale* or *microscale*, often has a complex, heterogeneous structure that will be homogenised for the macroscale. Computational homogenisation is applied when no constitutive relation can be assumed directly for the macroscale.

An important aspect of the method is the *principle of separation of scales*. The length scale of the subscale, L_m, has to be considerably smaller than the length scale of the macroscale, L_M, or else the strains of the macroscale could change over the length of the subscale:

$$L_m << L_M \tag{1.26}$$

The procedure for computational homogenisation is as follows. For each integration point on the macroscale, a Representative Volume Element, or RVE, is defined on the mesoscale, see Figure 1.4. These RVEs define the material properties of the structure.

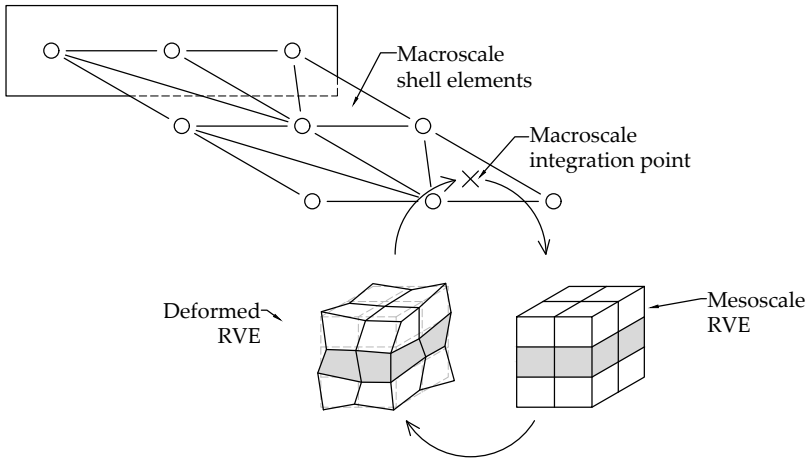

Figure 1.4.: RVEs coupled to macroscale element integration points

The RVEs are constrained by a defined set of boundary conditions. This constraining of the RVE is referred to as *downscaling*. Various types of boundary conditions are applicable to RVEs; however, each type is typically associated with distinct limitations. Several boundary conditions may lead to overconstraining or induce unphysical behaviour within the RVE. This work will focus only on linear and periodic boundary conditions due to the simplicity of these boundary conditions and the mesoscopic model.

Linear boundary conditions are defined by the strains on the macroscale:

$$\mathbf{a_c} = \boldsymbol{A_b \epsilon_M} \tag{1.27}$$

with $\mathbf{a_c}$ denoting the constrained degrees of freedom on the RVE boundary nodes, $\mathbf{A_b}$ denoting a geometric matrix of the boundary nodes, and $\boldsymbol{\epsilon_M}$ denoting the strains of the macroscopic scale.

Periodic boundary conditions link the degrees of freedom of RVEs:

$$a_i = a_j \tag{1.28}$$

with a_i denoting a degree of freedom of node i on the RVE and a_j the degree of freedom of node j.

Solving the boundary value problem, or BVP, on the RVEs results in the stresses, strains, and stiffness of the mesoscale. The stresses and stiffness need to be translated back to the macroscale, also referred to as *upscaling*. This is done using the *Hill-Mandel macro-homogeneity principle*, which states that the macroscopic stresses and strains must be equal to the volume average of the mesoscopic stresses and strains over the RVE. In the case of a 2D shell element linked to 3D RVEs, the volume is actually the in-plane area of the RVE. The Hill-Mandel macro-homogeneity principle is defined as:

$$\sigma_M : \epsilon_M = \frac{1}{|\Omega|} \int_\Omega \sigma_m \epsilon_m d\Omega \tag{1.29}$$

The macroscopic stresses are obtained by volume averaging the mesoscopic stresses:

$$\sigma_M = \frac{1}{|\Omega|} \int_\Omega \sigma_m d\Omega \tag{1.30}$$

with M denoting the macroscale stresses and strains, m the mesoscale stresses and strains, and Ω the area of the RVE.

To solve Equation 1.30, the mesoscopic stiffness matrix $\mathbf{K_m}$ is split into the following sub-matrices:

$$\mathbf{K_m} = \begin{bmatrix} \mathbf{K_{ff}} & \mathbf{K_{fc}} \\ \mathbf{K_{cf}} & \mathbf{K_{cc}} \end{bmatrix} \tag{1.31}$$

so that the following expression relating the displacement vector $\mathbf{a}$ to the external force vector $\mathbf{f}$ can be derived:

$$\begin{bmatrix} \mathbf{K_{ff}} & \mathbf{K_{fc}} \\ \mathbf{K_{cf}} & \mathbf{K_{cc}} \end{bmatrix} \begin{bmatrix} \mathbf{a_f} \\ \mathbf{a_c} \end{bmatrix} = \begin{bmatrix} \mathbf{0} \\ \mathbf{f_c} \end{bmatrix} \tag{1.32}$$

with $\mathbf{a}$ denoting the displacements, $\mathbf{f}$ denoting the forces, subscript $\mathbf{f}$ denoting free nodes, and subscript $\mathbf{c}$ denoting constrained nodes. Stiffness matrices $\mathbf{K_{ff}}$ and $\mathbf{K_{fc}}$ relate the degrees of freedom of free nodes $\mathbf{a_f}$ and of constrained nodes $\mathbf{a_c}$ to the force vector of the free nodes $\mathbf{f_f}$, which by definition is a nulvector: $\mathbf{f_f} = \mathbf{0}$. Then stiffness matrices $\mathbf{K_{cf}}$ and $\mathbf{K_{cc}}$ relate the displacements of free nodes and of constrained nodes to the force vector of constrained nodes $\mathbf{f_c}$, which is the loaded part of the external force vector.

Rewriting Equation 1.30 and Equation 1.32 results in the following:

$$\sigma_M = \frac{1}{|\Omega|} \mathbf{A_b}^T \mathbf{f_c} = \frac{1}{|\Omega|} \mathbf{A_b}^T (\mathbf{K_{cc}} - \mathbf{K_{cf}} \mathbf{K_{ff}}^{-1} \mathbf{K_{fc}}) \mathbf{a_c} \tag{1.33}$$

which can be simplified to:

$$\sigma_M = \frac{1}{|\Omega|} \mathbf{A_b}^T \overline{\mathbf{K}}_{\mathbf{cc}} \mathbf{A_b} \epsilon_M \tag{1.34}$$

with

$$\overline{\mathbf{K}}_{\mathbf{cc}} = \mathbf{K}_{\mathbf{cc}} - \mathbf{K}_{\mathbf{cf}}{\mathbf{K}_{\mathbf{ff}}}^{-1}\mathbf{K}_{\mathbf{fc}} \tag{1.35}$$

and

$$\mathbf{A}_{\mathbf{b}}\epsilon_M = \mathbf{a}_{\mathbf{c}} \tag{1.36}$$

Next, the macroscopic material stiffness matrix, $\mathbf{D}$, can be defined using Hooke's Law:

$$\mathbf{D}_{\mathbf{M}} = \frac{1}{|\Omega|}{\mathbf{A}_{\mathbf{b}}}^{T}\overline{\mathbf{K}}_{\mathbf{cc}}\mathbf{A}_{\mathbf{b}} \tag{1.37}$$

$\overline{\mathbf{K}}_{\mathbf{cc}}$ contains the inverse of a matrix, see Equation 1.35. A probing technique can be applied to get the macroscopic stresses and material stiffness matrix without having to invert $\mathbf{K}_{\mathbf{ff}}$. This probing technique builds the macroscopic material stiffness matrix in a column-wise manner as follows:

For every column of the material tangent ($i = 1, ..., n$), the right-hand side of Equation 1.37 is multiplied with a unit vector $\mathbf{e}_{\mathbf{i}}$:

$$\mathbf{D}_{\mathbf{M,i}} = \frac{1}{|\Omega|}{\mathbf{A}_{\mathbf{b}}}^{T}(\mathbf{K}_{\mathbf{cc}} - \mathbf{K}_{\mathbf{cf}}{\mathbf{K}_{\mathbf{ff}}}^{-1}\mathbf{K}_{\mathbf{fc}})\mathbf{f}_{\mathbf{i}} \tag{1.38}$$

with $\mathbf{f}_{\mathbf{i}} = \mathbf{A}_{\mathbf{b}}\mathbf{e}_{\mathbf{i}}$.

Next, $\mathbf{K}_{\mathbf{cc}}\mathbf{f}_{\mathbf{i}}$ and $\mathbf{K}_{\mathbf{fc}}\mathbf{f}_{\mathbf{i}}$ are calculated as follows:

$$\begin{bmatrix}\mathbf{K}_{\mathbf{ff}} & \mathbf{K}_{\mathbf{fc}}\\ \mathbf{K}_{\mathbf{cf}} & \mathbf{K}_{\mathbf{cc}}\end{bmatrix}\begin{bmatrix}\mathbf{0}\\ \mathbf{f}_{\mathbf{i}}\end{bmatrix} = \begin{bmatrix}\mathbf{K}_{\mathbf{fc}}\mathbf{f}_{\mathbf{i}}\\ \mathbf{K}_{\mathbf{cc}}\mathbf{f}_{\mathbf{i}}\end{bmatrix} = \begin{bmatrix}\mathbf{g}\\ \mathbf{h}\end{bmatrix} \tag{1.39}$$

Then, the following linear system of equations is solved:

$$\begin{bmatrix}\mathbf{K}_{\mathbf{ff}} & \mathbf{K}_{\mathbf{fc}}\\ \mathbf{K}_{\mathbf{cf}} & \mathbf{K}_{\mathbf{cc}}\end{bmatrix}\begin{bmatrix}\mathbf{u}\\ \mathbf{0}\end{bmatrix} = \begin{bmatrix}\mathbf{g}\\ \mathbf{0}\end{bmatrix} \tag{1.40}$$

Note that $\mathbf{K}_{\mathbf{ff}}$ does not need to be inverted to find $\mathbf{u}$.

Now, by applying $\mathbf{u}$, $\mathbf{K}_{\mathbf{cf}}\mathbf{u}$ can be calculated as follows:

$$\begin{bmatrix}\mathbf{K}_{\mathbf{ff}} & \mathbf{K}_{\mathbf{fc}}\\ \mathbf{K}_{\mathbf{cf}} & \mathbf{K}_{\mathbf{cc}}\end{bmatrix}\begin{bmatrix}\mathbf{u}\\ \mathbf{0}\end{bmatrix} = \begin{bmatrix}\mathbf{K}_{\mathbf{ff}}\mathbf{u}\\ \mathbf{K}_{\mathbf{cf}}\mathbf{u}\end{bmatrix} = \begin{bmatrix}\mathbf{m}\\ \mathbf{p}\end{bmatrix} \tag{1.41}$$

Substituting $\mathbf{h}$ and $\mathbf{p}$ into Equation 1.38 gives:

$$\mathbf{D}_{\mathbf{M,i}} = \frac{1}{|\Omega|}{\mathbf{A}_{\mathbf{b}}}^{T}(\mathbf{h} - \mathbf{p}) \tag{1.42}$$

The macroscopic material stiffness matrix can now be assembled by combining the columns $\mathbf{D}_{\mathbf{M,i}}$:

$$\mathbf{D}_{\mathbf{M}} = \begin{bmatrix}\mathbf{D}_{\mathbf{M,1}} & \dots & \mathbf{D}_{\mathbf{M,n}}\end{bmatrix} \tag{1.43}$$

1.7. Delamination Modelling

For the modelling of the delamination, the *Discrete Crack Approach* is employed, integrating a discontinuous displacement field to model the delamination. An essential assumption inherent in this approach is the a priori knowledge of the crack (or delamination) location. This assumption proves advantageous, given that the location of delaminations is predetermined, specifically situated between the plies of a laminate. This method of crack modelling can be described by the *interface elements*, the *Cohesive Zone Model*, and the corresponding *Traction Separation Law* [21, 22, 23].

Interface Elements
Figure 1.5 shows the interface elements for a 3D model. These interface elements can describe a discontinuous jump between two continuum elements. Jumps can be either in the normal direction, a so-called *Mode-I* jump, or in a transverse direction, *Mode-II* for sliding shear and *Mode-III* for tearing shear. A combination of a normal and transverse jump is known as a *Mixed-Mode* jump.

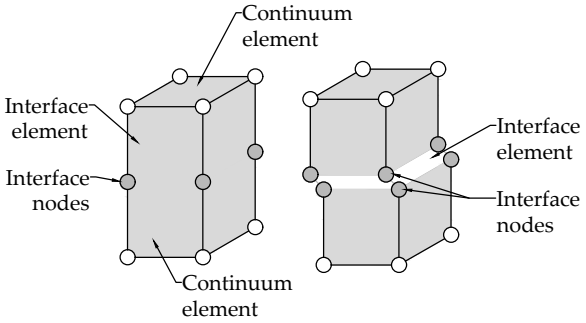

Figure 1.5.: Interface elements

Just like for continuum elements, the degrees of freedom of the interface element can be described with the nodal displacements using the shape functions for interface elements, see Equation 1.2:

$$\mathbf{u_e}(\mathbf{x}) = [\![\mathbf{u}]\!] = \mathbf{N_{e,IF}}(\mathbf{x})\mathbf{a_e} \tag{1.44}$$

with $[\![\mathbf{u}]\!]$ describing the normal and transverse jumps between the top and bottom parts of the element:

$$[\![\mathbf{u}]\!] = \mathbf{u_e^+} - \mathbf{u_e^-} \tag{1.45}$$

The nodal displacements of the element are defined by $\mathbf{a_e}$:

$$\mathbf{a_e} = \begin{bmatrix} u_1^n & u_1^{tx} & u_1^{ty} & \dots & u_n^n & u_n^{tx} & u_n^{ty} \end{bmatrix}^T \tag{1.46}$$

with the subscripts denoting the nodes of the element (1 to n), and the superscripts denoting the jumps in normal (n) and transverse (tx and ty) directions. The shape functions matrix for the element, $\mathbf{N_{e,IF}}$, now looks a bit different than for a continuum element:

$$\mathbf{N_{e,IF}} = \begin{bmatrix} \mathbf{N_{bottom}} & \mathbf{N_{top}} \end{bmatrix} \tag{1.47}$$

with

$$\mathbf{N_{bottom}} = \begin{bmatrix} -N_1 & 0 & 0 & ... & -N_{n/2} & 0 & 0 \\ 0 & -N_1 & 0 & ... & 0 & -N_{n/2} & 0 \\ 0 & 0 & -N_1 & ... & 0 & 0 & -N_{n/2} \end{bmatrix} \tag{1.48}$$

and

$$\mathbf{N_{top}} = \begin{bmatrix} N_{n/2+1} & 0 & 0 & ... & N_n & 0 & 0 \\ 0 & N_{n/2+1} & 0 & ... & 0 & N_n & 0 \\ 0 & 0 & N_{n/2+1} & ... & 0 & 0 & N_n \end{bmatrix} \tag{1.49}$$

Again, just like for continuum elements, the internal force for the interface elements can be defined as:

$$\mathbf{f_{e,IF}}^{int} = \int_\Gamma \mathbf{N_{e,IF}}(\mathbf{x})^T \mathbf{t} d\Gamma \tag{1.50}$$

where $\mathbf{t}$ is the cohesive traction in the element and Γ is the interface surface. The element tangent matrix can then be defined as:

$$\mathbf{K_{e,IF}} = \int_\Gamma \mathbf{N_{e,IF}}(\mathbf{x})^T \mathbf{T} \mathbf{N_{e,IF}} d\Gamma \tag{1.51}$$

where

$$\mathbf{T} = \frac{\delta \mathbf{t}}{\delta [\![\mathbf{u}]\!]} \tag{1.52}$$

Subsequently, the global tangent matrix, global displacement vector, and global (external) force vectors are assembled, and the field problem can be solved.

Cohesive Zone Model
As loading increases on the interface element, the element will crack open. The opening of the crack can be split into three stages, namely undamaged (no crack has been developed yet), damage evolution (the crack begins to open), and fully damaged (the crack is fully open). The Cohesive Zone Model, or CZM, describes the cohesion of the interface element's top and bottom parts. This corresponds to the first two stages of the crack opening. Once the crack is fully open, there is no more cohesion between the elements.

Following the work of Wieringa [23], an initially elastic CZM is applied in this work. A load-displacement curve for an initially elastic CZM is shown in Figure 1.6.

Accompanying the CZM is the Traction Separation Law, or TSL, which describes the softening branch of the CZM. Cohesive traction can be defined as:

$$\mathbf{t} = f([\![\mathbf{u}]\!], \beta) \tag{1.53}$$

with f denoting the TSL, $[\![\mathbf{u}]\!]$ denoting the jumps, and β denoting interlaminar material properties.

Traction Separation Law
The chosen TSL follows a mixed-mode damage model by Turon et al. [20], with later improvements proposed by Van der Meer and Sluys [22]. The TSL is defined as:

$$\mathbf{t} = [\mathbf{I} - \omega_d \mathbf{P}] K_d [\![\mathbf{u}]\!] \tag{1.54}$$

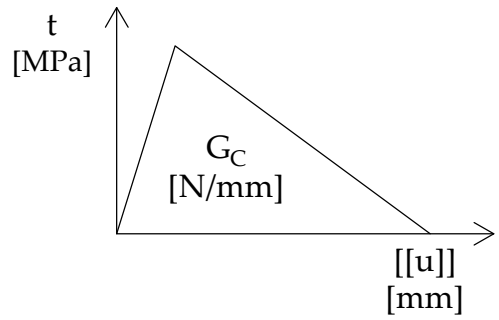

Figure 1.6.: Initially elastic Cohesive Zone Model

where ω_d is a damage variable, $\mathbf{P}$ is a matrix that prevents compressive cohesive tractions, and K_d is the initial stiffness.

$\mathbf{P}$ can be found as follows:

$$\mathbf{P} = \begin{bmatrix} \frac{\langle [\![u]\!]_n \rangle}{[\![u]\!]_n} & 0 & 0 \\ 0 & 1 & 0 \\ 0 & 0 & 1 \end{bmatrix} \tag{1.55}$$

with

$$\langle [\![u]\!]_n \rangle = \frac{[\![u]\!]_n + |[\![u]\!]_n|}{2} \tag{1.56}$$

The damage variable ω_d can be found as follows:

$$\omega_d = \begin{cases} 0, & [\![u]\!]_{eq} \leq [\![u]\!]^0_{eq} \\ \frac{[\![u]\!]^f_{eq}([\![u]\!]_{eq} - [\![u]\!]^0_{eq})}{[\![u]\!]_{eq}([\![u]\!]^f_{eq} - [\![u]\!]^0_{eq})}, & [\![u]\!]^0_{eq} < [\![u]\!]_{eq} < [\![u]\!]^f_{eq} \\ 1, & [\![u]\!]_{eq} \geq [\![u]\!]^f_{eq} \end{cases} \tag{1.57}$$

where $[\![u]\!]_{eq}$ is the equivalent jump, $[\![u]\!]^0_{eq}$ the equivalent jump at the onset of damage, and $[\![u]\!]^f_{eq}$ the equivalent jump after the damage has fully developed. These equivalent jumps are defined as:

$$[\![u]\!]_{eq} = \sqrt{\langle [\![u]\!]_n \rangle^2 + [\![u]\!]^2_t}, \qquad \text{with} \qquad [\![u]\!]_t = \sqrt{([\![u]\!]_{tx})^2 + ([\![u]\!]_{ty})^2} \tag{1.58a}$$

$$[\![u]\!]^0_{eq} = \sqrt{([\![u]\!]^0_n)^2 + \alpha^\eta \left(([\![u]\!]^0_t)^2 - ([\![u]\!]^0_n)^2 \right)} \tag{1.58b}$$

$$[\![u]\!]^f_{eq} = \frac{[\![u]\!]^0_n [\![u]\!]^f_n + \alpha^\eta \left([\![u]\!]^0_t [\![u]\!]^f_t - [\![u]\!]^0_n [\![u]\!]^f_n \right)}{[\![u]\!]^0_{eq}} \tag{1.58c}$$

with

$$\alpha = \frac{[\![u]\!]_t^2}{[\![u]\!]_t^2 + \langle [\![u]\!]_n \rangle^2} \tag{1.59a}$$

$$[\![u]\!]_n^0 = \frac{F_n}{K_d}, \qquad [\![u]\!]_n^f = \frac{2G_{Ic}}{F_n} \tag{1.59b}$$

$$[\![u]\!]_t^0 = \frac{F_t}{K_d}, \qquad [\![u]\!]_t^f = \frac{2G_{IIc}}{F_t} \tag{1.59c}$$

where F_n and F_t are the interlaminar strengths in normal and transverse directions, G_{Ic} and G_{IIc} are the fracture toughness for Mode-I and Mode-II jumps, and η is the Benzeggagh-Kenane interaction parameter [3].

2. Computational Homogenisation of a Mindlin-Reissner Shell

In this chapter, 3D solid RVEs are coupled to 2D Mindlin-Reissner shell elements for isotropic material. First, in Section 2.1, the macro- and mesoscale models will be formulated, and the coupling between the two scales will be explained. Then, a number of load cases will be presented in Section 2.2. The multiscale framework will be tested on these load cases and compared to 3D DNS analyses. For each load case, a mesh sensitivity study on the macroscale and mesoscale will be performed. Additionally, the influence of the RVE widths will be explored. The results of the analyses will be presented in Section 2.3 and lastly, they will also be discussed in Section 2.4.

2.1. Model Formulation

Due to the nature of delamination, Mindlin-Reissner shell elements are introduced in Section 2.1.1 to account for the shear stresses and strains. The three-dimensional RVEs coupled to these shell elements will be formulated in Section 2.1.2. Lastly, the coupling between the macro- and mesoscales will be shown in Section 2.1.3.

2.1.1. Macroscale Model

On the macroscale, Mindlin-Reissner shell elements (MR elements) are applied. The formulation for Mindlin-Reissner shell elements is also known as the *First-Order Shear Deformation Theory* (FSDT) for composite laminates [18]. Figure 2.1 shows a single three-noded triangular MR element with corresponding positive degrees of freedom. The displacements of MR elements are defined only by x and y coordinates:

$$\mathbf{x} = \begin{bmatrix} x & y \end{bmatrix}^T \tag{2.1}$$

Displacements are considered constant over the height of the shell. This is in contrast to 3D solid elements, where displacements are defined by x, y, and z coordinates. This assumption will generally lead to stiffer responses from the MR elements.

MR elements have five degrees of freedom, namely:

$$\mathbf{u_e}(\mathbf{x}) = \begin{bmatrix} u & v & w & \theta_x & \theta_y \end{bmatrix}^T \tag{2.2}$$

The nodal displacements of an element can then be defined as:

$$\mathbf{a_e} = \begin{bmatrix} a_1^u & a_1^v & a_1^w & a_1^{\theta x} & a_1^{\theta y} & \dots & a_n^u & a_n^v & a_n^w & a_n^{\theta x} & a_n^{\theta y} \end{bmatrix}^T \tag{2.3}$$

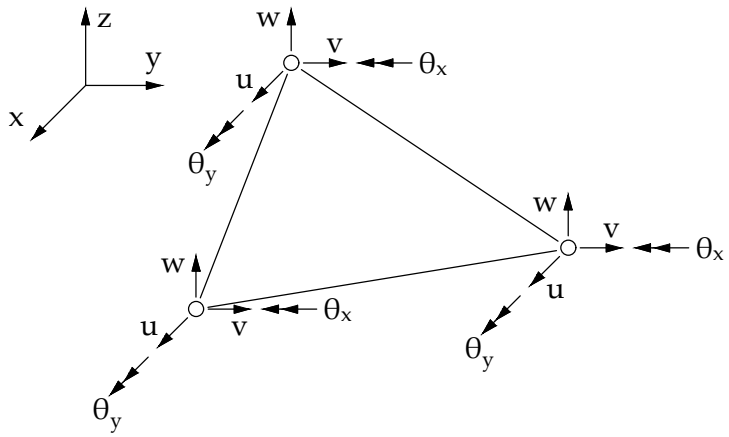

Figure 2.1.: Three-noded triangular Mindlin-Reissner shell element

The strains of MR elements can be defined as:

$$\boldsymbol{\epsilon_e} = \begin{bmatrix} \epsilon_{xx} & \epsilon_{yy} & 2\epsilon_{xy} & \kappa_{xx} & \kappa_{yy} & 2\kappa_{xy} & \gamma_x & \gamma_y \end{bmatrix}^T \tag{2.4}$$

with

$$\epsilon_{xx} = \frac{\partial u}{\partial x} \tag{2.5a}$$
$$\epsilon_{yy} = \frac{\partial v}{\partial y} \tag{2.5b}$$
$$2\epsilon_{xy} = \frac{\partial u}{\partial y} + \frac{\partial v}{\partial x} \tag{2.5c}$$
$$\kappa_{xx} = \frac{\partial \theta_x}{\partial x} \tag{2.5d}$$
$$\kappa_{yy} = \frac{\partial \theta_y}{\partial y} \tag{2.5e}$$
$$2\kappa_{xy} = \frac{\partial \theta_x}{\partial y} + \frac{\partial \theta_y}{\partial x} \tag{2.5f}$$
$$\gamma_x = \frac{\partial w}{\partial x} - \theta_x \tag{2.5g}$$
$$\gamma_y = \frac{\partial w}{\partial y} - \theta_y \tag{2.5h}$$

Following Equation 1.7 this results in the following $\mathbf{B_e}(\mathbf{x})$:

$$\mathbf{B_e}(\mathbf{x}) = \begin{bmatrix} N_{1,x} & 0 & 0 & 0 & 0 & ... & N_{n,x} & 0 & 0 & 0 & 0 \\ 0 & N_{1,y} & 0 & 0 & 0 & ... & 0 & N_{n,y} & 0 & 0 & 0 \\ N_{1,y} & N_{1,x} & 0 & 0 & 0 & ... & N_{n,y} & N_{n,x} & 0 & 0 & 0 \\ 0 & 0 & 0 & N_{1,x} & 0 & ... & 0 & 0 & 0 & N_{n,x} & 0 \\ 0 & 0 & 0 & 0 & N_{1,y} & ... & 0 & 0 & 0 & 0 & N_{n,x} \\ 0 & 0 & 0 & N_{1,y} & N_{1,x} & ... & 0 & 0 & 0 & N_{n,y} & N_{n,x} \\ 0 & 0 & N_{1,x} & N_1 & 0 & ... & 0 & 0 & N_{n,x} & N_n & 0 \\ 0 & 0 & N_{1,y} & 0 & -N_1 & ... & 0 & 0 & N_{n,y} & 0 & -N_n \end{bmatrix} \tag{2.6}$$

The internal force vector, element stiffness matrices, and global stiffness matrix can be assembled following Equation 1.10 through Equation 1.13.

Unlike 3D solid elements, the material stiffness matrix of an MR element includes the height of the shell. The material stiffness matrix for an isotropic material is defined as:

$$\mathbf{D}_{iso} = \begin{bmatrix} \chi t & \nu\chi t & 0 & 0 & 0 & 0 & 0 & 0 \\ \nu\chi t & \chi t & 0 & 0 & 0 & 0 & 0 & 0 \\ 0 & 0 & \frac{1-\nu}{2}\chi t & 0 & 0 & 0 & 0 & 0 \\ 0 & 0 & 0 & \frac{1}{12}\chi t^3 & \frac{1}{12}\nu\chi t^3 & 0 & 0 & 0 \\ 0 & 0 & 0 & \frac{1}{12}\nu\chi t^3 & \frac{1}{12}\chi t^3 & 0 & 0 & 0 \\ 0 & 0 & 0 & 0 & 0 & \frac{1-\nu}{24}\chi t^3 & 0 & 0 \\ 0 & 0 & 0 & 0 & 0 & 0 & kGt & 0 \\ 0 & 0 & 0 & 0 & 0 & 0 & 0 & kGt \end{bmatrix} \tag{2.7}$$

with

$$\chi = \frac{E}{1-\nu^2} \tag{2.8}$$

and

$$G = \frac{E}{2(1+\nu)} \tag{2.9}$$

where E is the Young's modulus, G the shear modulus, ν the Poisson's ratio, t the thickness, and k a shear correction factor. The shear strain over the height of a structure generally isn't constant; however, due to the assumptions made for an MR element, the shear strain is constant over the height. The shear correction factor takes this into account. Due to the added complexity of calculating the shear correction factor for orthotropic composite laminates, in this work, a shear correction factor of $k = 1$ will be applied, resulting in stiffer responses of the MR elements. According to Daniel and Ishai [6], in many cases, it is sufficiently accurate to assume this shear correction factor $k = 1$.

2.1.2. Mesoscale Formulation

On the mesoscale, 3D solid elements are applied. Section 1.4 covers the formulation of these elements. Figure 2.2 shows a single eight-noded hexagonal, or brick, element used in this work. Figure 2.3 shows the mesoscale RVE, consisting of eight-noded brick elements.

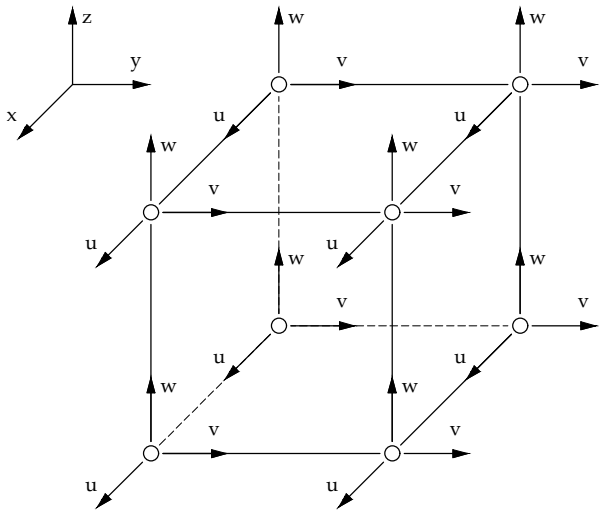

Figure 2.2.: Eight-noded hexagonal 3D solid element

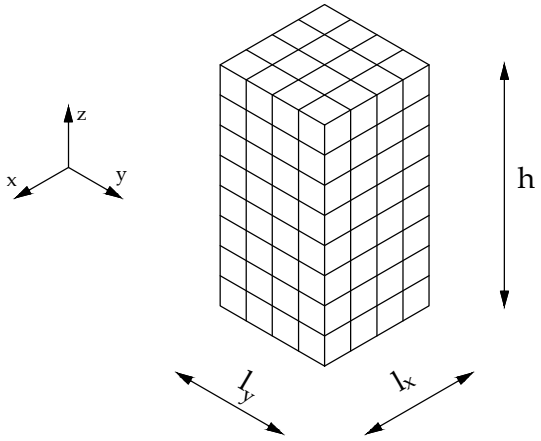

Figure 2.3.: RVE with 3D solid elements

Initially, only the RVEs will capture the material properties and thickness of the laminate. In the case of a fully isotropic material, the RVEs will have the same material properties over the height of the RVE. This height will capture the thickness of the shell, which violates the principle of separation of scales, see Equation 1.26. Macroscopic strain components will be set as boundary conditions on the RVE. However, the strain components of the macroscale are assumed to be constant over the thickness of the shell. This could be problematic for the out-of-plane shear components, which are generally not constant over the height of 3D solid elements.

2.1.3. Scale Coupling

The macro- and mesoscale are coupled by setting boundary conditions on the RVE. These boundary conditions transfer the macroscopic strains to the RVE. Solving the BVP results in mesoscopic stress vector. The macroscopic stresses can then be found using the Hill-Mandel macro-homogeneity principle. Furthermore, the global stiffness matrix of the RVE, together with the geometric matrix that captures the boundary conditions, can define the material stiffness matrix of the macroscopic scale following the Hill-Mandel macro-homogeneity principle and probing method explained in Section 1.6.

The boundary conditions set on the RVE are taken from Gruttmann and Wagner, and Herwig and Wagner [7, 8]. These works use a combination of linear boundary conditions and periodic boundary conditions. Firstly, the deformation on the boundaries of the RVE can be defined using the assumed displacement field for Mindlin-Reissner shell elements:

$$\begin{bmatrix} u_b \\ v_b \\ w_b \end{bmatrix}_m = \begin{bmatrix} \epsilon_{xx} + z\kappa_{xx} & \epsilon_{xy} + z\kappa_{xy} & \gamma_x \\ \epsilon_{xy} + z\kappa_{xy} & \epsilon_{yy} + z\kappa_{yy} & \gamma_y \\ -\frac{1}{2}(\kappa_{xx}x + \kappa_{xy}y) & -\frac{1}{2}(\kappa_{yy}y + \kappa_{xy}x) & 0 \end{bmatrix} \begin{bmatrix} x \\ y \\ z \end{bmatrix}_m \tag{2.10}$$

Rewriting Equation 2.10 with the macroscale strains as the vector gives:

$$\begin{bmatrix} u_b \\ v_b \\ w_b \end{bmatrix}_m = \begin{bmatrix} x & 0 & \frac{1}{2}y & xz & 0 & \frac{1}{2}yz & z & 0 \\ 0 & y & \frac{1}{2}x & 0 & yz & \frac{1}{2}xz & 0 & z \\ 0 & 0 & 0 & -\frac{1}{2}x^2 & -\frac{1}{2}y^2 & \frac{1}{2}xy & 0 & 0 \end{bmatrix}_m \begin{bmatrix} \epsilon_{xx} \\ \epsilon_{yy} \\ 2\epsilon_{xy} \\ \kappa_{xx} \\ \kappa_{yy} \\ 2\kappa_{xy} \\ \gamma_x \\ \gamma_y \end{bmatrix}_M \tag{2.11}$$

However, these linear boundary conditions result in the unphysical behaviour of the RVE due to the prevention of the contractions of the material over the height at the edges. This will lead to an overly stiff response, which can be interpreted as an upper bound solution [10]. The boundary conditions need to be loosened. This is done by removing the boundary

conditions for the vertical displacement, w_b:

$$\begin{bmatrix} u_b \\ v_b \end{bmatrix}_m = \begin{bmatrix} x & 0 & \frac{1}{2}y & xz & 0 & \frac{1}{2}yz & z & 0 \\ 0 & y & \frac{1}{2}x & 0 & yz & \frac{1}{2}xz & 0 & z \end{bmatrix}_m \begin{bmatrix} \epsilon_{xx} \\ \epsilon_{yy} \\ 2\epsilon_{xy} \\ \kappa_{xx} \\ \kappa_{yy} \\ 2\kappa_{xy} \\ \gamma_x \\ \gamma_y \end{bmatrix}_M \tag{2.12}$$

However, now the RVE is underconstrained. The RVE is not fixed in its vertical direction and will also be able to endlessly rotate about its x and y axes. To overcome these problems, the RVE needs to be fixed in the vertical direction, and periodic boundary conditions are applied to the boundaries to overcome the rotation about the x and y axes. To fix the RVE in vertical direction, the vertical translational degree of freedom of a single node is set to zero. This could be any node. This work will take the middle node of the RVE:

$$w(x,y,z)_m = 0, \qquad x = y = z = 0 \tag{2.13}$$

Furthermore, the periodic boundary conditions applied in this work set the vertical displacement of an edge equal to the vertical displacement of the opposite edge in an anti-symmetric way:

$$w_m(L_x/2, y, z) = w_m(-L_x/2, -y, z) \tag{2.14a}$$
$$w_m(x, L_y/2, z) = w_m(-x, -L_y/2, z) \tag{2.14b}$$

Figure 2.4 shows the proposed deformations of the RVE, following the applied boundary conditions.

This work applies a second-order computational homogenisation framework, where thick shell elements are coupled to 3D RVEs. By applying this framework to the aforementioned linear and periodic boundary conditions, the RVE will show size dependency. There are numerous ways to remove this size dependency. The work of Hii and El Said [9] proposes a different type of boundary condition for the RVE, namely a volumetric constraint on the fluctuation moment field, which removes the size dependency on the mesoscale. Another approach to removing this size dependency is to apply the Irving-Kirkwood theory, as opposed to the Hill-Mandel principle mentioned in Section 1.6. This approach does not constrain the RVE with boundary conditions but instead applies a global constraint that links the strains between the macro- and mesoscales [14]. Lastly, the method of *Variationally Consistent Homogenisation* could also prove to solve this size dependency. In this method, the macroscale and mesoscale problems are both derived from a single, fully resolved problem [5]. These are just a few of the newly discovered approaches to further improve the multiscale framework approach; however, they will not be further explored in this work, as the size dependency of the RVE is not an issue. The material properties of the RVE do not change over the widths of the RVE; thus, applying a very narrow RVE that fully captures the material properties is possible. In Section 2.3.3, the size dependency of the RVE is further explored. Optionally, these different approaches could be explored to reduce the number of elements in the RVE. In order to maintain a proper aspect ratio of height to width for the elements within the RVE, many elements will be necessary over the height of the RVE. Eliminating the size dependency will solve this issue and result in faster analyses due to fewer elements being applied.

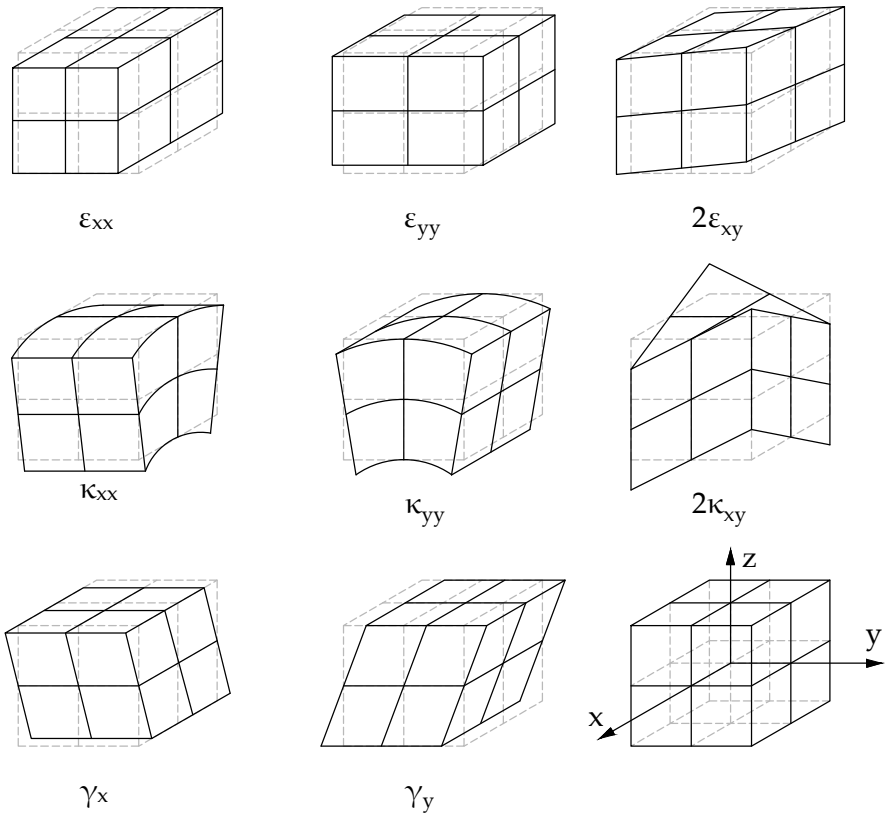

Figure 2.4.: RVE kinematics

2.2. Load Cases

To verify the multiscale framework, three load cases are introduced, which will be tested on the framework. The following load cases will be analysed:

- Cantilever extension beam
- Cantilever bending beam
- Three-point bending beam

Figure 2.5 shows the load cases that will be tested. Table 2.1 shows the corresponding geometry of the beam for the load cases and the material properties of the isotropic material applied in the analyses.

Cantilever extension beam
The top of Figure 2.5 shows the configuration for the cantilever beam in extension for the 3D, shell, and FE^2 analyses. The cantilever beam will be fixed at one end and loaded in horizontal x direction at the other end. For the 3D analysis, this means that the degrees of freedom u, v and w will be set to 0 at the clamp, and u at the other end will have a prescribed

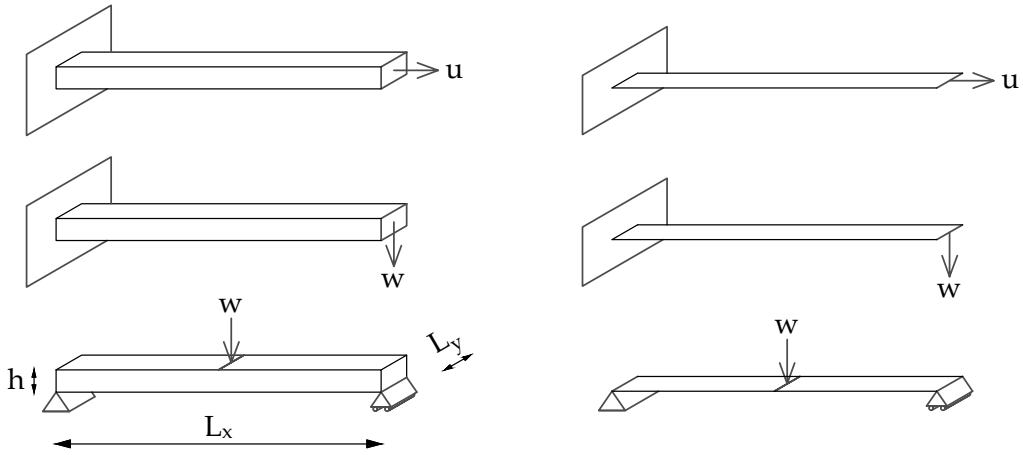

(a) Load cases for 3D analyses

(b) Load cases for shell and FE^2 analyses

Figure 2.5.: Load cases

	Variable	Value	Unit
Geometry	L_x	100	mm
	L_y	4	mm
	h	8	mm
Isotropic material properties	E	122,700	N/mm^2
	ν	0.25	-
	G	49,080	N/mm^2

Table 2.1.: Parameter list

deformation. For the Mindlin-Reissner analysis, the degrees of freedom u, v, w, and θ_x will be set to 0 at the clamp, and u at the other end will have a prescribed deformation. The rotation θ_y could optionally also be set to 0 at the clamp; however, constraining the vertical displacement w over the length L_y guarantees that this rotation will be 0. The prescribed deformation u is 5 mm.

Cantilever bending beam
The middle of Figure 2.5 shows the configuration for the cantilever beam in bending for the 3D, shell, and FE^2 analyses. The support conditions for both the 3D and Mindlin-Reissner analysis are the same for the cantilever extension beam; however, at the loaded end, a prescribed deformation in the z direction will be applied. For the 3D analysis, the load is applied at the end surface area of the beam as a prescribed deformation w. For the Mindlin-Reissner analysis, the load is applied at the end of the beam as a prescribed deformation w. The prescribed deformation w is 10 mm.

Three-point bending beam
The bottom of Figure 2.5 shows the configuration for the three-point bending beam for the 3D, shell, and FE^2 analyses. The three-point bending beam will be constrained at both

bottom ends in the z direction and only at the bottom left end in the x and y directions. Furthermore, a prescribed deformation in the z direction is applied at the top of the beam in the middle. For the 3D analysis, this means that the degrees of freedom u, v, and w will be set to 0 at the bottom left edge, and w will be set to 0 at the bottom right edge. The load, in the form of a prescribed deformation, is applied at the top of the beam in the middle. For the Mindlin-Reissner analysis, the degrees of freedom u, v, and w are set to 0 at the left edge, w is set to 0 at the right edge, and w is set to the prescribed deformation in the middle of the shell. Due to the assumption that the displacements are constant over the height of the MR elements, the Mindlin-Reissner analyses will result in much stiffer responses for the three-point bending beam than the 3D analyses. To somewhat overcome this problem, the 3D analyses could also be constrained in w over the height of the beam or in the centre of the beam height; however, these analyses are physically unrealistic or uncommon; therefore, the proper configuration for the three-point bending test, as performed in physical tests, will be applied for the 3D analyses. The prescribed deformation w is 10 mm.

2.3. Results

The first step to verifying the multiscale framework is to set a proper mesh size. A mesh sensitivity study is performed in Section 2.3.1 for 3D DNS analyses and for Mindlin-Reissner shell analyses, not yet applying the multiscale framework. Section 2.3.2 will continue with a mesh sensitivity study on the mesoscale. Lastly, the influence of the width of the RVE will be explored in Section 2.3.3.

2.3.1. Macroscale Mesh Sensitivity Study

A mesh sensitivity study on both macro- and mesoscales will be performed to determine the proper mesh sizes. A beam with dimensions L_x = 100 mm, L_y = 4 mm and h = 8 mm will be discretized into $n_{elems,x}$ elements in the x-direction, $n_{elems,y}$ elements in the y-direction, and for the 3D analyses, also $n_{elems,z}$ elements in the z-direction. This discretization results in element sizes of d_x in the x-direction, d_y in the y-direction, and for the 3D analyses, also d_z in the z-direction. For the Mindlin-Reissner analyses, triangular elements are applied, which means twice the total amount of elements are applied ($n_{elems,T3} = 2n_{elems,x}n_{elems,y}$). The number of triangular elements in the Mindlin-Reissner analyses is $n_{elems,T3}$, and the number of hexagonal elements in the 3D analyses is $n_{elems,H8}$. MR_M is the *Macroscale Mesh Refinement* number, where doubling the MR_M results in doubling the amount of elements in x, y, and z directions. This doubling of the MR_M is shown in Figure 2.6 for 3D solid elements and MR shell elements. Table 2.2 shows the macroscale mesh refinement parameters.

Figure 2.7 shows the results of the mesh refinement for the Mindlin-Reissner and 3D analyses. The x-axis shows the Macroscale Mesh Refinement number, MR_M. The y-axis shows the load as a percentage of the load for the 3D analysis at MR_M = 8. All models show the expected downward convergence of the force with respect to the MR_M number. Surprisingly, the cantilever beams in extension and bending show stiffer results for the 3D analyses than for the MR analyses. This is possibly due to the boundary conditions of the 3D analyses also constraining the beam in the z-direction over the height, where it would contract due to the non-zero Poisson's ratio. Furthermore, the convergence rate of the 3D analyses is much steeper than the Mindlin-Reissner analyses for the cantilever bending beam and the

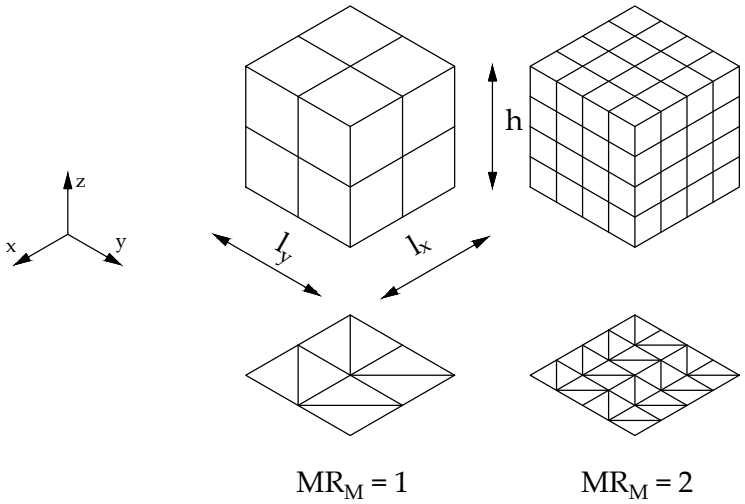

Figure 2.6.: Example of the MR_M for 3D solid (top) and MR shell (bottom) elements

	Variable	Value	Unit		Variable	Value	Unit
MR_M 1	$n_{elems,x}$	50	-	MR_M 4	$n_{elems,x}$	200	-
	$n_{elems,y}$	2	-		$n_{elems,y}$	8	-
	$n_{elems,z}$	4	-		$n_{elems,z}$	16	-
	d_x	2	mm		d_x	0.5	mm
	d_y	2	mm		d_y	0.5	mm
	d_z	2	mm		d_z	0.5	mm
	$n_{elems,T3}$	200	-		$n_{elems,T3}$	3,200	-
	$n_{elems,H8}$	400	-		$n_{elems,H8}$	25,600	-
MR_M 2	$n_{elems,x}$	100	-	MR_M 8	$n_{elems,x}$	400	-
	$n_{elems,y}$	4	-		$n_{elems,y}$	16	-
	$n_{elems,z}$	8	-		$n_{elems,z}$	32	-
	d_x	1	mm		d_x	0.25	mm
	d_y	1	mm		d_y	0.25	mm
	d_z	1	mm		d_z	0.25	mm
	$n_{elems,T3}$	800	-		$n_{elems,T3}$	12,800	-
	$n_{elems,H8}$	3,200	-		$n_{elems,H8}$	204,800	-

Table 2.2.: Macroscale mesh refinement parameters

three-point bending beam. This is due to the mesh being refined in an extra dimension (z-direction) as well for the 3D analyses. The number of elements for the Mindlin-Reissner analyses is four times as much when doubling the MR_M number, whereas for the 3D analyses, there are eight times as many elements when doubling the MR_M number. For the cantilever extension beam, only the number of elements in the x-direction is relevant, so the convergence rates are quite similar.

The cantilever beams in extension and bending give quite good results, differing only by 0.08% and 0.19% for MR_M = 8. The three-point bending beam, however, differs a bit more by 1.13% for MR_M = 8. This is greatly due to the assumption that the three-point bending beam is only constrained at the bottom left and right and loaded only at the top middle of the beam for the 3D analyses. This results in more localised deformations at the boundary conditions for the 3D model, which is more realistic, especially for thicker beams. However, the displacements of the Mindlin-Reissner analyses are equal over the height of the beam, so the boundary conditions are applied over the full height of the beam, resulting in a stiffer response.

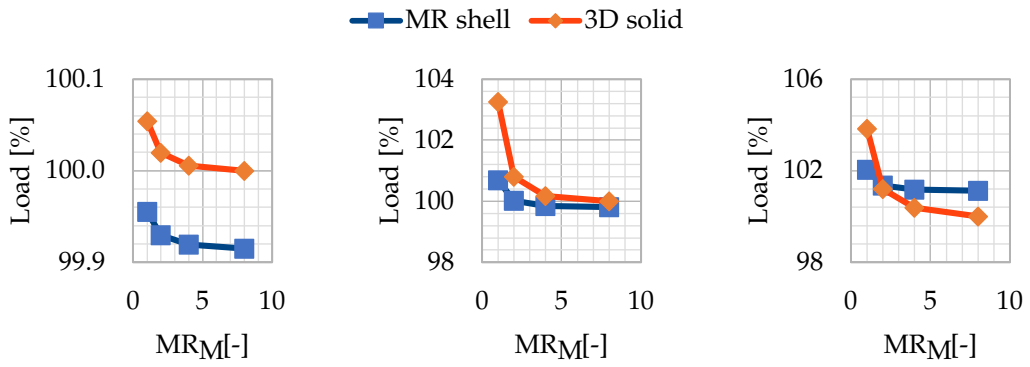

(a) Cantilever extension beam (b) Cantilever bending beam (c) Three-point bending beam

Figure 2.7.: Load-MR_M number for the macroscale mesh refinement

2.3.2. Mesoscale Mesh Sensitivity Study

For the mesoscale mesh refinement, the Macroscale Mesh Refinement number is set at MR_M = 2, so 100 elements in the x-direction and 4 elements in the y-direction on the macroscale. Now, the RVE with dimensions $L_x = L_y = 1$ mm and h = 8 mm will be discretized in $n_{elems,x\&y}$ elements in x and y directions, and $n_{elems,z}$ elements in z direction. This discretization results in element sizes of $d_{x\&y}$ in the x and y directions, and d_z in z direction. Note that an aspect ratio of 4 is applied for the height-to-width ratio of the elements of the RVE to save on computational time. This means that the height of the elements is four times the width of the elements. The number of hexagonal elements in an RVE is $n_{elems,H8}$. Now, MR_m is the *Mesoscale Mesh Refinement* number, where doubling the MR_m results in doubling the amount of elements in x, y, and z directions for the RVE. Table 2.3 shows the mesoscale mesh refinement parameters.

	Variable	Value	Unit
MR_m 1	$n_{elems,x\&y}$	2	-
	$n_{elems,z}$	4	-
	$d_{x\&y}$	0.5	mm
	d_z	2	mm
	$n_{elems,H8}$	16	-
MR_m 2	$n_{elems,x\&y}$	4	-
	$n_{elems,z}$	8	-
	$d_{x\&y}$	0.25	mm
	d_z	1	mm
	$n_{elems,H8}$	128	-
MR_m 4	$n_{elems,x\&y}$	8	-
	$n_{elems,z}$	16	-
	$d_{x\&y}$	0.125	mm
	d_z	0.5	mm
	$n_{elems,H8}$	1,024	-

Table 2.3.: Mesoscale mesh refinement parameters

Figure 2.8 shows the results of the mesh refinement for the RVEs. The x-axis shows the Mesoscale Mesh Refinement number, MR_m. The y-axis shows the load as a percentage of the load for the Mindlin-Reissner analysis at $MR_M = 2$. When comparing the FE^2 model with a MR shell model, the results are a lot more accurate than in Section 2.3.1, where MR shell models are compared to 3D models. Again, expected downward convergence occurs for the cantilever bending beam and three-point bending beam. The cantilever extension beam shows exact results, irrespective of the MR_m number. Strains due to extension are generally constant over the height of a beam. The strains from the macroscale are applied constantly over the height of the RVE. For out-of-plane shear strain, this is generally not the case. However, for extension, this is not a problem, and the resulting stiffness components for extension will be exact. For bending, the strain over the height of the RVE is also constant; however, contractions due to the non-zero Poisson's ratio will influence the bending stiffness components slightly, resulting in a stiffer response. The cantilever bending beam and three-point bending beam show good results for convergence.

Figure 2.9 shows the non-zero, non-exact, normalised components of the stiffness matrix, extracted from the FE^2 analyses. Components related to the extensional strains ϵ_{xx}, ϵ_{yy} and $2\epsilon_{xy}$, are exact and not shown in the results. The bending stiffness component ($2\kappa_{xy}$,$2\kappa_{xy}$) also gives exact results, irrespective of the mesoscale mesh refinement, and is also not shown in the results. The bending stiffness component (κ_{yy},κ_{yy}) and shear stiffness component (γ_y,γ_y) are not shown because these have the same value as components (κ_{xx},κ_{xx}) and (γ_x,γ_x), respectively. All components are converging downwards, as expected for a mesh refinement. The components related to bending, (κ_{xx},κ_{xx}) and (κ_{xx},κ_{yy}), initially have a higher value and seem to converge to the exact value; however, the component related to shear (γ_x,γ_x) starts out lower than the exact value and converges away from the exact value, resulting in a weaker response of the model for shear-dominated cases. This could be explained by the RVE width influence, covered in Section 2.3.3. Interestingly, the bending stiffness components are initially non-exact. This is in contrast to Wieringa's work [23], where both the extension and the bending stiffness components are exact. There could be two reasons for the bending stiffness component being exact in Wieringa's work. The first is that the Pois-

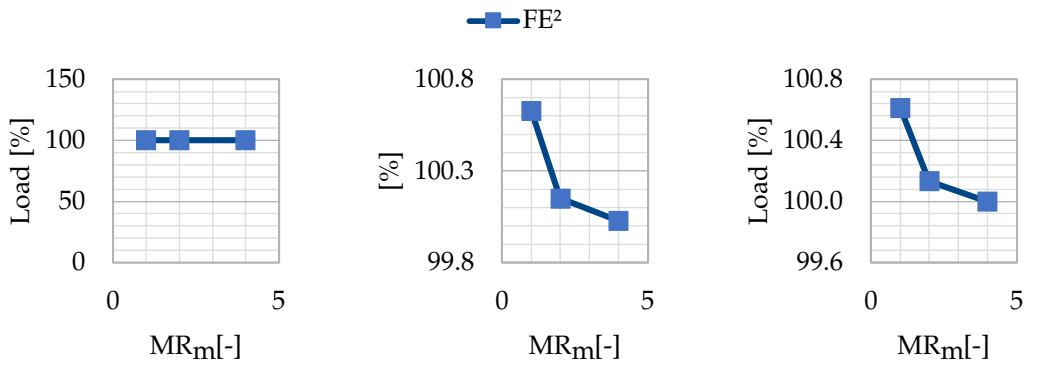

(a) Cantilever extension beam (b) Cantilever bending beam (c) Three-point bending beam

Figure 2.8.: Load-MR_m number for the mesoscale mesh refinement

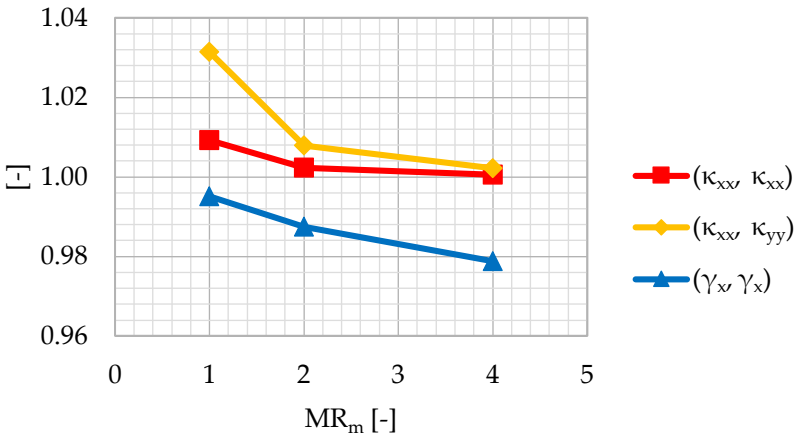

Figure 2.9.: Normalised stiffness matrix components with corresponding MR_m number

son ratio in Wieringa's work was taken at 0. The RVE will not contract over the height, thus leading to exact values for the bending stiffness. A second explanation could be that the values of the bending stiffness components in Wieringa's work differ so little that they are rounded up to the same value.

2.3.3. RVE Width Sensitivity Study

Lastly, the influence of the width of the RVE is explored. A fixed number of elements in the x and y directions is applied. To save on computational time, the RVE has only 2 elements in the x and y directions. The work of Herwig and Wagner [8] shows that applying only 2 elements in the x and y directions is enough to properly capture the proposed deformations for the RVE. Again, the aspect ratio of 4 for height to width is applied. Now, *WR* is the *Width Refinement* number, where doubling the WR results in halving the element size in x, y, and z directions and, as such, the widths in x and y directions. The amount of elements in the x and y directions will remain at 2, however, the elements in the z direction will become twice as much, so that the height of the RVE will still be the same as the thickness of the laminate. As the WR increases, the RVE will become more narrow. On the macroscale, the same MR_M number is applied as for the mesoscale mesh refinement: $MR_M = 2$. Table 2.4 shows the RVE width refinement parameters.

	Variable	Value	Unit		Variable	Value	Unit
WR 1	RVE_{width}	0.4	mm	WR 8	RVE_{width}	0.05	mm
	$n_{elems,x\&y}$	2	-		$n_{elems,x\&y}$	2	-
	$n_{elems,z}$	10	-		$n_{elems,z}$	80	-
	$d_{x\&y}$	0.2	mm		$d_{x\&y}$	0.025	mm
	d_z	0.8	mm		d_z	0.1	mm
	$n_{elems,H8}$	40	-		$n_{elems,H8}$	320	-
WR 2	RVE_{width}	0.2	mm	WR 16	RVE_{width}	0.025	mm
	$n_{elems,x\&y}$	2	-		$n_{elems,x\&y}$	2	-
	$n_{elems,z}$	20	-		$n_{elems,z}$	160	-
	$d_{x\&y}$	0.1	mm		$d_{x\&y}$	0.0125	mm
	d_z	0.4	mm		d_z	0.05	mm
	$n_{elems,H8}$	80	-		$n_{elems,H8}$	640	-
WR 4	RVE_{width}	0.1	mm				
	$n_{elems,x\&y}$	2	-				
	$n_{elems,z}$	40	-				
	$d_{x\&y}$	0.05	mm				
	d_z	0.2	mm				
	$n_{elems,H8}$	160	-				

Table 2.4.: RVE width refinement parameters

Figure 2.10 shows the results of the RVE width refinement. The x-axis now shows the Width Refinement number, WR. The y-axis again shows the load as a percentage of the load of the Mindlin-Reissner analysis at $MR_M = 2$. Again, the results for the cantilever extension beam are exact. The load-WR number for the cantilever bending beam and three-point bending beam converges downwards to the exact value quite well.

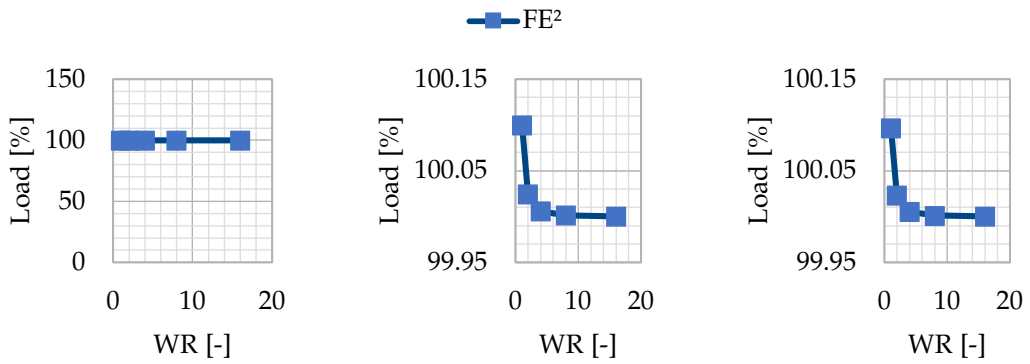

(a) Cantilever extension beam (b) Cantilever bending beam (c) Three-point bending beam

Figure 2.10.: Load-WR number

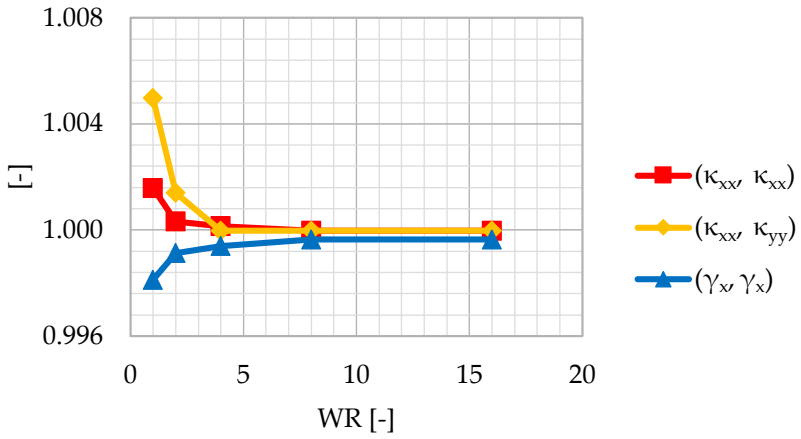

Figure 2.11.: Normalised stiffness matrix components with corresponding WR number

Figure 2.11 shows the non-zero, non-exact, normalised components of the stiffness matrix, extracted from the FE^2 analyses. Both bending stiffness components, (κ_{xx},κ_{xx}) and (κ_{xx},κ_{yy}), converge downwards to the exact value, whereas the shear stiffness component (γ_x,γ_x) converges upwards to the exact value. Initially, a wide RVE does not properly extract the shear and bending stiffness components. Bending stiffness components are overly stiff, whereas the shear stiffness components will be less stiff. As the width of the RVE decreases, both the bending stiffness and shear stiffness components will converge to the exact value. Due to the downward convergence of the bending stiffness components and the upward convergence of the shear stiffness components, load-MR number and load-WR number graphs can converge with a single oscillation, as seen later in Section 3.3.

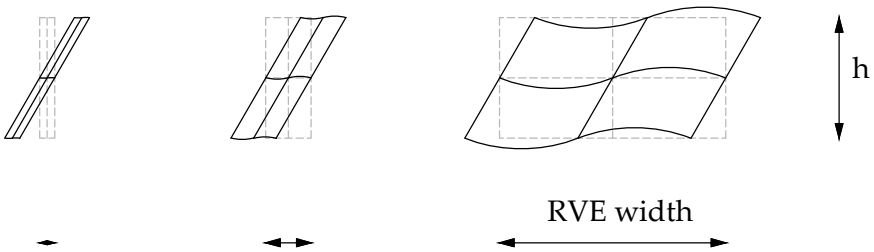

Figure 2.12.: RVE width influence on shear deformation

Figure 2.12 shows a simplified 2D response of the shear deformation within the RVE as the width undergoes refinement. Owing to the unconstrained nature of the RVE's top and bottom surfaces, these regions exhibit a tendency towards bending. When a narrow RVE is employed, this bending will be limited; however, when applying a wide RVE, bending deformations become dominant in the RVE, impeding the accurate capture of shear deformations. This phenomenon explains the observed upward convergence of the shear stiffness in Figure 2.11. A wide RVE predominantly exhibits minimal shear deformation, while a narrow RVE exhibits a more pronounced and accurate representation of shear deformation.

2.4. Concluding Remarks

The multiscale framework coupling Mindlin-Reissner shell elements and 3D solid RVEs has been tested on numerous load cases and compared to regular Mindlin-Reissner shell analyses. Overall, the FE^2 analyses show good convergence for the components of the stiffness matrix.

Based on the results of the macroscale mesh refinement, it is evident that comparing regular Mindlin-Reissner analyses to 3D DNS analyses gives better results when consistent assumptions are made for both models. However, Mindlin-Reissner shell elements are based on assumptions that are not always realistic. The cantilever bending and extension beams are more consistent than the three-point bending beam, resulting in a more accurate result.

Furthermore, both the Mindlin-Reissner and 3D DNS analyses are sensitive to mesh refinement; however, the 3D DNS analysis is more sensitive due to the additional dimension. The macroscopic mesh sensitivity has to be taken into account. A macroscopic mesh refinement number, MR_M, of at least 4 will be used.

The mesoscale mesh refinement also proved the mesh sensitivity of the RVEs; however, results differ quite little. For the mesoscale mesh, 2 elements in x and y directions and an aspect ratio of 4 for height to width will be applied.

Lastly, but most importantly, the influence of the width of the RVEs has been explored. Results show that the stiffness components for bending and shear are dependent on the width of the RVE, both converging to exact values as the width decreases. The widths (with respect to the height) of the RVE will also have to be taken into account. An RVE height of 8 mm and a width of 0.05 mm in the x and y directions will be used for further analyses. This results in an aspect ratio of 160.

3. Computational Homogenisation for Anisotropic Material

In this chapter, the multiscale framework presented in the previous chapter, Chapter 2, will be tested for anisotropic material. First, a number of composite ply configurations are presented. Then, the analytical values for the components of the stiffness matrix, or the *ABDH matrix*, will be calculated. Each ply configuration will be tested on the load cases presented in Section 2.2 and compared to 3D DNS analyses. Again, for each load case and ply configuration, a mesh sensitivity study on macroscale and mesoscale will be performed, following the same mesh refinement parameters from Table 2.2 and Table 2.3, respectively. The influence of the RVE widths will also be explored following Table 2.4. The results of the analyses will be presented, and lastly, they will also be discussed.

3.1. Ply Configurations

Three different composite ply configurations will be analysed in this chapter. The following ply configurations will be analysed for each load case:

- 0
- $0/90_2/0$
- 45/-45

Figure 3.1 and Table 3.1 show the ply configurations and orthotropic material properties of the plies, respectively.

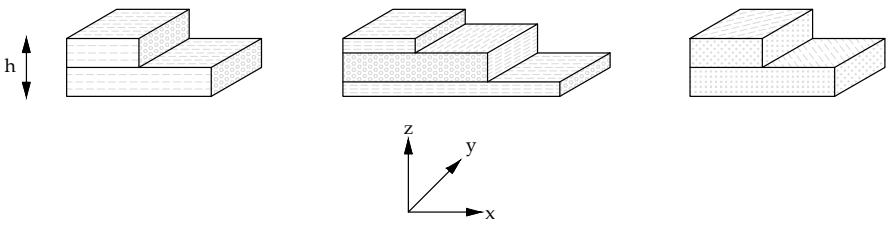

(a) 0 (b) $0/90_2/0$ (c) 45/-45

Figure 3.1.: Ply configurations

	Variable	Value	Unit
Orthotropic material properties	E_1	122,700	N/mm^2
	E_2	10,100	N/mm^2
	E_3	10,100	N/mm^2
	ν_{12}	0.25	-
	ν_{23}	0.45	-
	ν_{31}	0.25	-
	G_{12}	5,500	N/mm^2
	G_{23}	3,480	N/mm^2
	G_{31}	5,500	N/mm^2

Table 3.1.: Parameter list

3.2. ABDH Matrix

The material stiffness matrix used in Mindlin-Reissner analyses for composite laminates with orthotropic plies is called an ABDH matrix. As the name suggests, this matrix consists of 4 sub-matrices, namely:

1. the A-matrix, which determines the membrane stress-strain relationship,
2. the B-matrix, which couples the membrane stresses and strains to the bending stresses and strains,
3. the D-matrix, which determines the bending stress-strain relationship,
4. and the H-matrix, which determines the shear stress-strain relationship.

Note that for isotropic material, there are no components in the stiffness matrix that couple the extension and bending.

Following the layer numbering for laminates in Figure 3.2, the ABDH matrix can be defined as [18]:

$$\mathbf{ABDH} = \begin{bmatrix} \mathbf{A}_{3x3} & \mathbf{B}_{3x3} & \mathbf{0}_{3x2} \\ \mathbf{B}_{3x3} & \mathbf{D}_{3x3} & \mathbf{0}_{3x2} \\ \mathbf{0}_{2x3} & \mathbf{0}_{2x3} & \mathbf{H}_{2x2} \end{bmatrix} \tag{3.1}$$

with

$$\mathbf{A} = \begin{bmatrix} A_{11} & A_{12} & A_{16} \\ A_{12} & A_{22} & A_{26} \\ A_{16} & A_{26} & A_{66} \end{bmatrix}, \qquad \mathbf{B} = \begin{bmatrix} B_{11} & B_{12} & B_{16} \\ B_{12} & B_{22} & B_{26} \\ B_{16} & B_{26} & B_{66} \end{bmatrix} \tag{3.2a}$$

$$\mathbf{D} = \begin{bmatrix} D_{11} & D_{12} & D_{16} \\ D_{12} & D_{22} & D_{26} \\ D_{16} & D_{26} & D_{66} \end{bmatrix}, \qquad \mathbf{H} = \begin{bmatrix} H_{44} & H_{45} \\ H_{45} & H_{55} \end{bmatrix} \tag{3.2b}$$

and

$$A_{ij} = \sum_{k=1}^{N} \bar{Q}_{ij}^{(k)}(z_{k+1} - z_k), \qquad B_{ij} = \frac{1}{2}\sum_{k=1}^{N} \bar{Q}_{ij}^{(k)}(z_{k+1}^2 - z_k^2) \tag{3.3a}$$

$$D_{ij} = \frac{1}{3}\sum_{k=1}^{N} \bar{Q}_{ij}^{(k)}(z_{k+1}^3 - z_k^3), \qquad H_{ij} = \sum_{k=1}^{N} \bar{Q}_{ij}^{(k)}(z_{k+1} - z_k) \tag{3.3b}$$

where $\bar{Q}^{(k)}$ is the plane stress version of the material stiffness matrix of the k^{th} composite ply, as defined in Equation 1.25 for a 3D orthotropic ply.

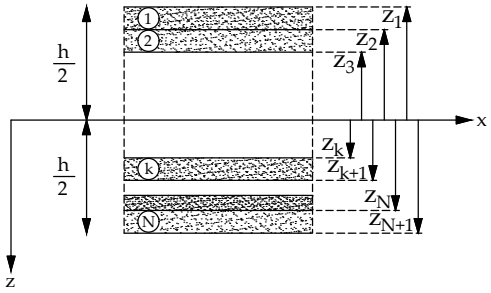

Figure 3.2.: Layer numbering for laminates, adapted from [18]

3.3. Results

The same macroscale and mesoscale mesh refinement studies as in Section 2.3.1 and Section 2.3.2 are performed for the different composite ply configurations in Section 3.3.1 and Section 3.3.2, respectively. The influence of the width of the RVE will again be explored in Section 3.3.3, following the width refinement parameters of Section 2.3.3.

3.3.1. Macroscale Mesh Sensitivity Study

Similar mesh sensitivity studies on macro- and mesoscales as in Section 2.3.1 and Section 2.3.2 are performed for the different composite ply configurations. On the macroscale, a beam with dimensions L_x = 100 mm, L_y = 4 mm, and h = 8 mm is discretized following the parameters from Table 2.2. Again, MR_M is the *Macroscale Mesh Refinement* number, where doubling the MR_M results in doubling the amount of elements in the x, y, and z directions.

Figure 3.3, Figure 3.4 and Figure 3.5 show the results of the mesh refinement for the Mindlin-Reissner and 3D analyses for the ply configurations 0, $0/90_2/0$, and 45/-45, respectively. The x-axis shows the Macroscale Mesh Refinement number, MR_M. The y-axis shows the load as a percentage of the load for the 3D analysis at MR_M = 8.

Again, all the analyses show a downward convergence of the force to the MR_M number, with the 3D analyses converging at a steeper rate for the cantilever bending beam and the three-point bending beam. Only the cantilever beam in extension for ply configuration 0 shows a larger force for the 3D analysis than for the MR shell analysis. This could again be explained by the extra stiffening effect of constraining the beam in z over the full height at the clamp. Furthermore, it is clear from Figure 3.3c and Figure 3.4c that the 3D analyses for the three-point bending beams with ply configurations 0 and $0/90_2/0$ haven't fully converged yet to a proper value at $MR_M = 8$.

The ply configurations 0 and $0/90_2/0$ perform reasonably well for the cantilever beams in extension and bending compared to the 3D analyses. The cantilever beams in extension differ by only 0.01% and 0.27% at $MR_M = 8$ for the ply configurations 0 and $0/90_2/0$, respectively. For the cantilever beam in bending, these values are 0.99% and 0.52%. Larger differences occur for the three-point bending beam. The ply configuration 0 has a difference of 13.39% at $MR_M = 8$, and the ply configuration $0/90_2/0$ differs by 10.63%. Moreover, the ply configuration 45/-45 differs quite a bit for all three load cases. For the cantilever beam in extension, this difference is 10.83%. For the cantilever beam in bending, the difference is 13.26%. Lastly, for the three-point bending beam, the difference is 15.63%. This could be due to the coupling of extension and bending that occurs. For the Mindlin-Reissner analyses, the ply configurations 0 and $0/90_2/0$ have trivial B-matrices, whereas the 45/-45 ply configuration's B-matrix is non-zero for the components coupling ϵ_{xx} to $2\kappa_{xy}$ and κ_{xx} to $2\epsilon xy$, and ϵ_{yy} to $2\kappa_{xy}$ and κ_{yy} to $2\epsilon_{xy}$. The 3D analyses will have localised deformations over the height, resulting in lower stiffness compared to the Mindlin-Reissner analyses, for which deformations over the height are constrained.

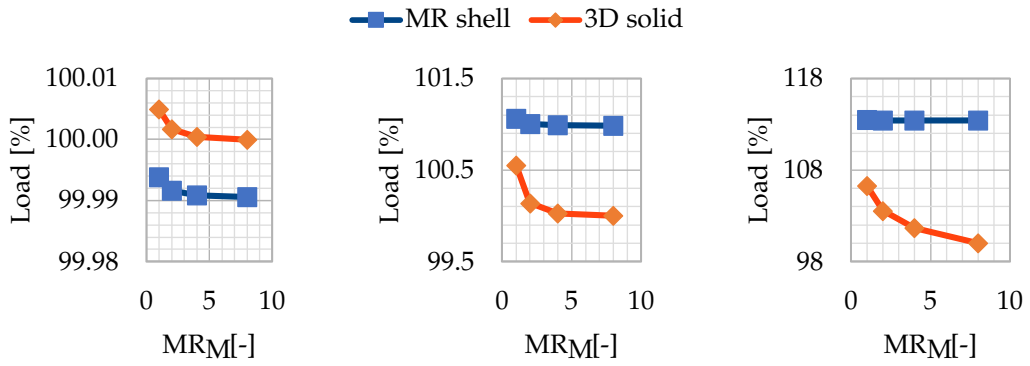

(a) Cantilever extension beam (b) Cantilever bending beam (c) Three-point bending beam

Figure 3.3.: Load-MR_M number for the macroscale mesh refinement, 0

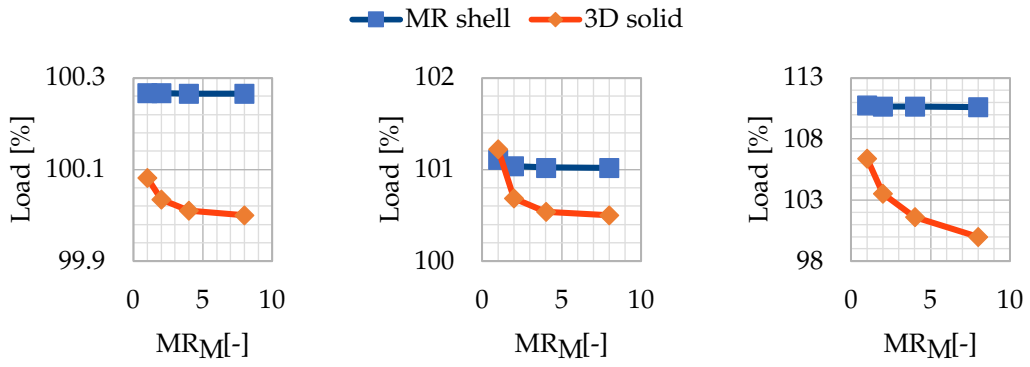

(a) Cantilever extensions beam (b) Cantilever bending beam (c) Three-point bending beam

Figure 3.4.: Load-MR_M number for the macroscale mesh refinement, $0/90_2/0$

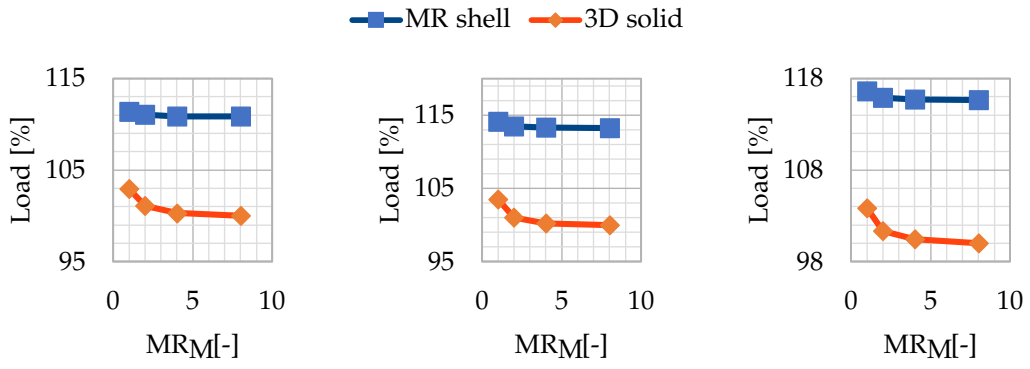

(a) Cantilever extension beam (b) Cantilever bending beam (c) Three-point bending beam

Figure 3.5.: Load-MR_M number for the macroscale mesh refinement, 45/-45

3.3.2. Mesoscale Mesh Sensitivity Study

For the mesoscale mesh refinement, the MR_M number of the macroscale is again set at MR_M = 2, so 100 elements in the x-direction and 4 elements in the y-direction. RVEs with dimensions L_x = L_y = 1 mm and h = 8 mm will be discretized following the parameters from Table 2.3. Again, an aspect ratio of 4 is applied for the height-to-width ratio of the elements. Now, MR_m is the *Mesoscale Mesh Refinement* number for the mesoscale mesh.

Figure 3.6, Figure 3.7, and Figure 3.8 show the results of the mesh refinement for the RVEs compared to the Mindlin-Reissner shell analyses for the ply configurations 0, $0/90_2/0$, and 45/-45, respectively. The x-axis shows the Mesoscale Mesh Refinement number, MR_m. The y-axis shows the load as a percentage of the load for the Mindlin-Reissner analysis at MR_M = 2. The load-to-MR_m number properly converges downward; however, it is often too far below the exact value. For the cantilever beam in extension with ply configurations 0 and $0/90_2/0$, the load is exact, regardless of the MR_m number; however, this is not the case for the cantilever beam in extension with ply configuration 45/-45. This is due to the non-zero values of the B-matrix not being exact as well; however, this difference is minimal. All values are reasonably close to the exact values.

Figure 3.9 shows the non-zero, non-exact, normalised components of the stiffness matrix for the three ply configurations. The results are similar to those for isotropic material from Figure 2.9, where stiffness components related to shear converge downwards below the exact value. Furthermore, stiffness components in the weaker direction, (κ_{yy},κ_{yy}) compared to (κ_{xx},κ_{xx}), and (γ_y,γ_y) compared to (γ_x,γ_x), for ply configurations 0 and $0/90_2/0$, converge at a much steeper rate.

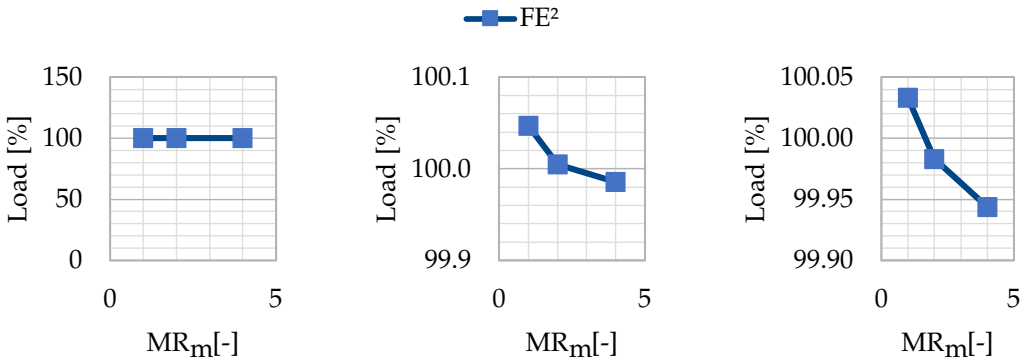

(a) Cantilever extension beam (b) Cantilever bending beam (c) Three-point bending beam

Figure 3.6.: Load-MR_m number for the mesoscale mesh refinement, 0

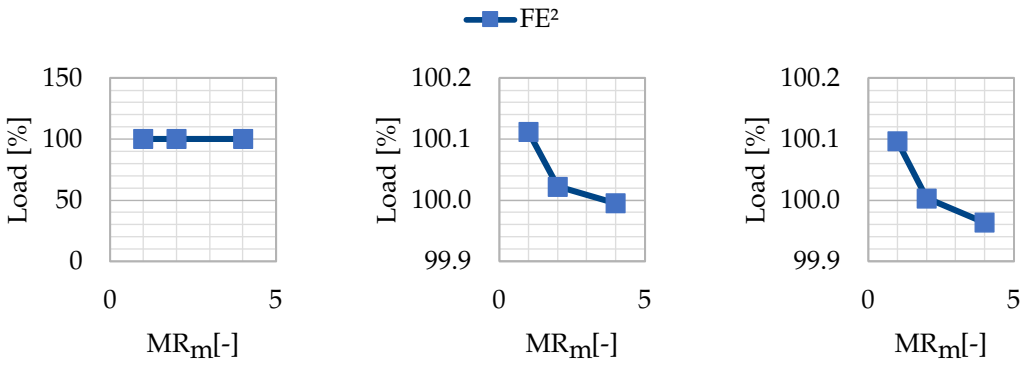

(a) Cantilever extension beam (b) Cantilever bending beam (c) Three-point bending beam

Figure 3.7.: Load-MR_m number for the mesoscale mesh refinement, $0/90_2/0$

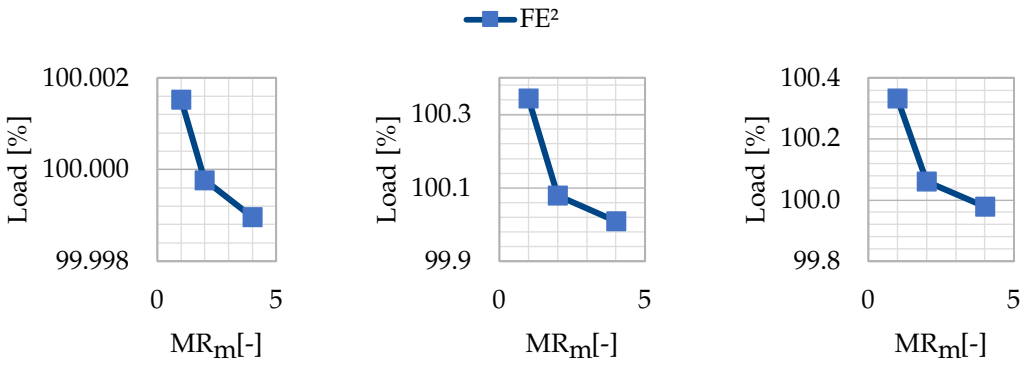

(a) Cantilever extension beam (b) Cantilever bending beam (c) Three-point bending beam

Figure 3.8.: Load-MR_m number for the mesoscale mesh refinement, 45/-45

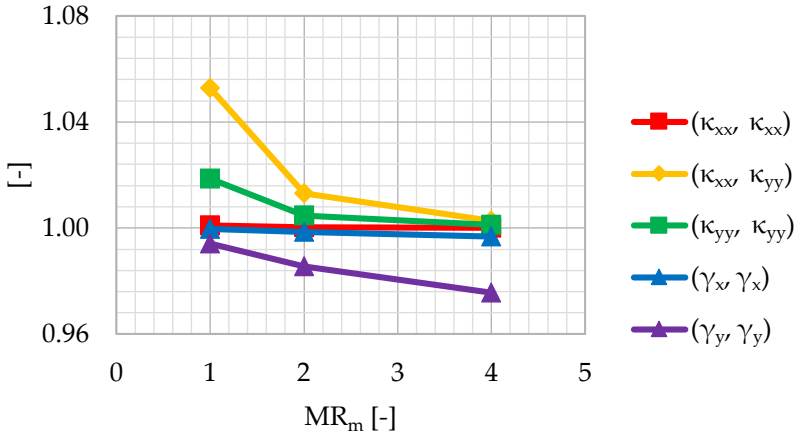

(a) 0

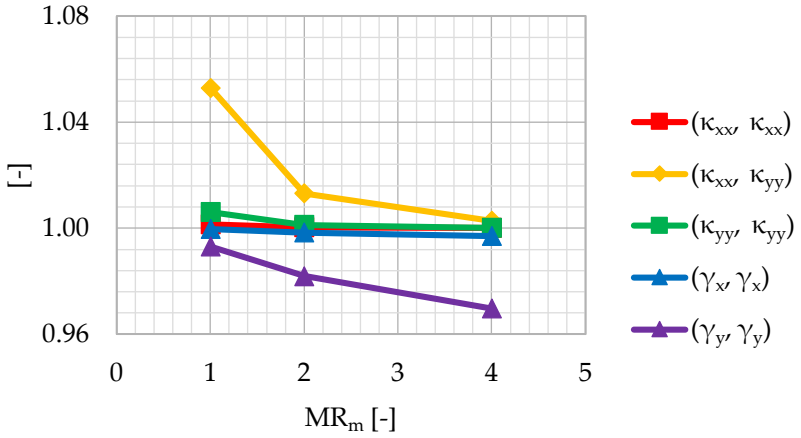

(b) $0/90_2/0$

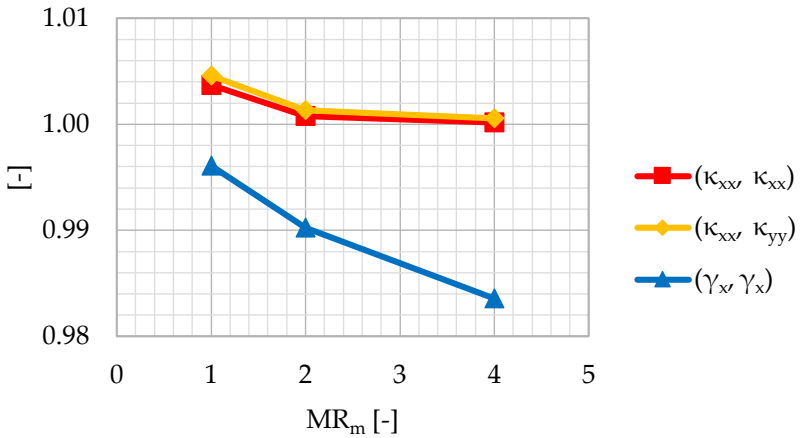

(c) 45/-45

Figure 3.9.: Normalised stiffness matrix components with corresponding MR_m number

3.3.3. RVE Width Sensitivity Study

The influence of the width of the RVE for anisotropic material is explored. Again, a fixed number of elements in x and y directions is applied: $n_{elems,x\&y} = 2$. The same aspect ratio of 4 for the height-to-width ratio is applied. *WR* is the *Width Refinement* number, where doubling the WR results in halving the element size in x, y, and z directions. On the macroscale, the same MR_M number is applied as for the mesoscale mesh refinement: $MR_M = 2$. Table 2.4 shows the RVE width refinement parameters. For the analyses of the ply configuration $0/90_2/0$, at WR = 1, the number of elements in z-direction, $n_{elems,z}$, will be 16 instead of 10, and the element size in z-direction, d_z, will be 0.5 instead of 0.8, so that the proper height for each ply can be described.

Figure 3.10, Figure 3.11 and Figure 3.12 show the results of the RVE width refinement compared to the Mindlin-Reissner shell analyses for the different ply configurations. The x-axis now shows the Width Refinement number, WR. The y-axis again shows the load as a percentage of the load of the Mindlin-Reissner analysis at $MR_M = 2$. The cantilever beams in extension show exact results for the ply configurations 0 and $0/90_2/0$. For ply configuration 45/-45, see Figure 3.12a, the load-WR number converges with a single oscillation at the start. This could again be explained due to the extension and bending coupling for the 45/-45 ply configuration. Due to the occurrence of bending in the element, there will be a shear force as well. As mentioned in Section 2.3.3, reducing the width of the RVE results in upward convergence for only the shear stiffness components, whereas the other stiffness components converge downward. This could result in the phenomenon observed in Figure 3.12a, where the value for the load first moves downward to a value lower than 100% as the RVE becomes more narrow, only to continue converging back upward to the exact value of 100%. All other graphs show proper convergence of the load with respect to the WR number. Reducing the RVE width results in more accurate results.

Figure 3.13 shows the non-zero, non-exact, normalised stiffness matrix components for the different ply configurations. Again, the results are similar to those of the isotropic material, see Figure 2.11. The shear components of the stiffness matrix converge upwards to the exact value, whereas other components converge downwards. Furthermore, stiffness matrix components in weaker directions have a steeper convergence rate than the components in the strong direction.

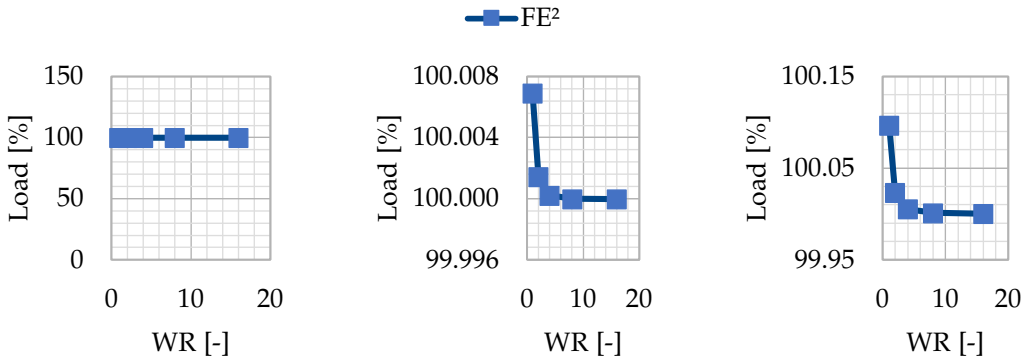

(a) Cantilever extension beam (b) Cantilever bending beam (c) Three-point bending beam

Figure 3.10.: Load-WR number, 0

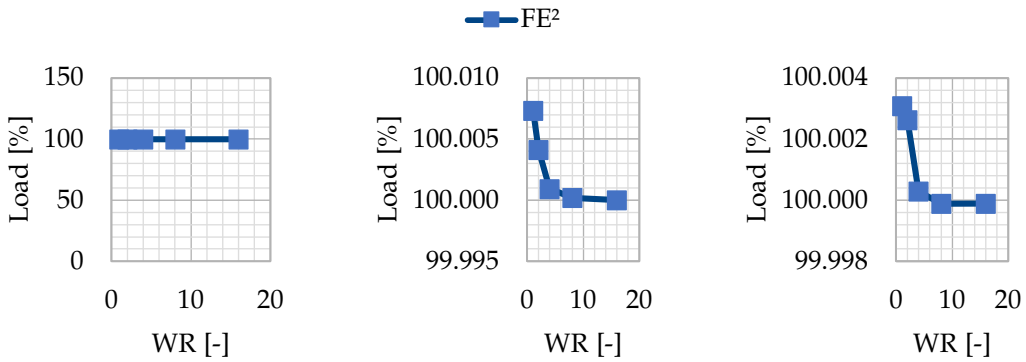

(a) Cantilever extension beam (b) Cantilever bending beam (c) Three-point bending beam

Figure 3.11.: Load-WR number, $0/90_2/0$

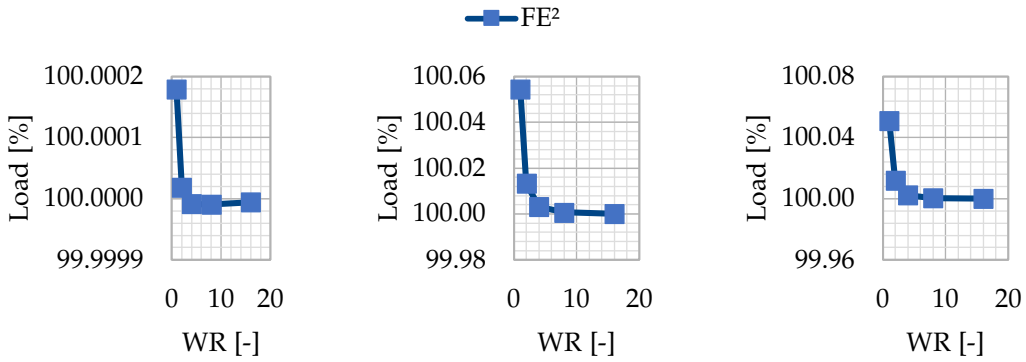

(a) Cantilever extension beam (b) Cantilever bending beam (c) Three-point bending beam

Figure 3.12.: Load-WR number, 45/-45

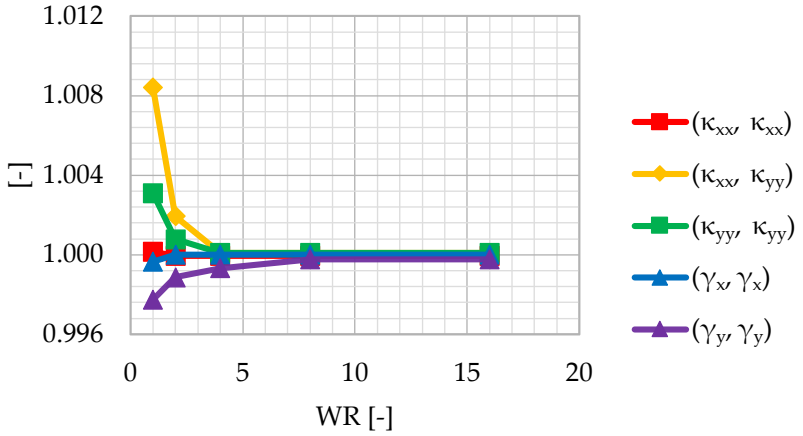

(a) 0

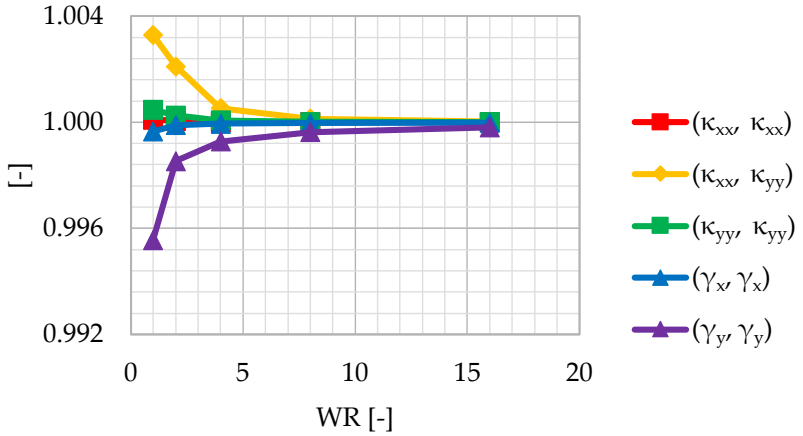

(b) $0/90_2/0$

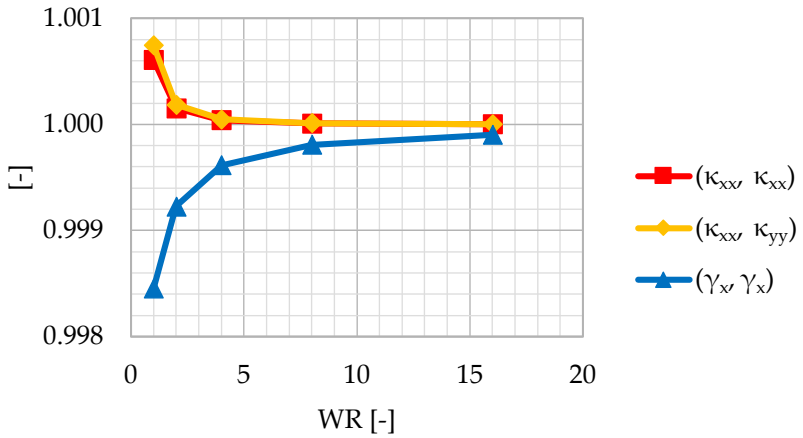

(c) 45/-45

Figure 3.13.: Normalised stiffness matrix components with corresponding WR number

3.4. Concluding Remarks

The multiscale framework coupling Mindlin-Reissner shell elements and 3D solid RVEs has been tested on numerous load cases with different ply configurations and compared to 3D and Mindlin-Reissner shell analyses. For anisotropic material, the FE^2 analyses also show good convergence for the components of the stiffness matrix; however, larger differences occur when comparing these analyses to 3D analyses due to larger local deformations over the height. When applying isotropic material, these local deformations are far less extreme due to the relatively higher shear stiffness components. Furthermore, composite laminates with orthotropic ply configurations can have a strong and a weak direction, resulting in relatively much larger local deformations in the weaker directions. This will all result in larger differences in the comparison of 3D and Minlin-Reissner shell analyses. Large local deformations occurring over the height cannot be recreated with the Mindlin-Reissner analyses; thus, results will diverge more from the 3D analyses. Furthermore, the macroscale mesh refinement shows that 3D analyses sometimes require significantly more elements to get a proper converged result, whereas the Mindlin-Reissner shell analyses converge with much fewer elements. However, the Mindlin-Reissner shell elements can show much stiffer responses.

For the mesoscale, a mesh sensitivity study and a width sensitivity study have been performed for composite laminates with different ply configurations. Both analyses show the dependency of the RVE with respect to mesh and width size. For the mesoscale mesh, 2 elements in x and y directions and an aspect ratio of 4 for height to width will be applied. Furthermore, a sufficiently narrow RVE needs to be implemented, or else the derived shear stiffness components will be too low. An aspect ratio of 160 for height to width of the RVE will be applied.

4. Inclusion of a Single Discrete Crack at the Mesoscale

In this chapter, a single delamination over the height of the RVEs is introduced to the multiscale framework. Again, the macro- and mesoscale models will be formulated, and the coupling between them will be explained. New load cases will be presented, on which the multiscale framework will be tested. Different ply configurations will be applied as well for these load cases. The results of the analyses will be compared to those of 3D DNS analyses. The chapter will again end with the results and the concluding remarks.

4.1. Model Formulation

To describe delamination on the macroscale in a shell model, a new type of element is introduced, namely *Shell-Interface-Shell elements*, or *SIFS elements*, adapted from Herwig and Wagner [8]. Section 4.1.1 gives the formulation for these SIFS elements on the macroscale. The mesoscale model, formulated in Section 4.1.2, describes the three-dimensional *coupled Representative Volume Elements*, or *cRVEs*, that include interface elements. Lastly, Section 4.1.3 will describe the coupling between the macro- and mesoscales.

4.1.1. Macroscale Model

On the macroscale, layered Mindlin-Reissner shell elements are applied, namely the *Shell-Interface-Shell*, or *SIFS elements*, introduced by Herwig and Wagner [8]. These elements consist of two identically shaped shell elements with an interface element connecting the two. Initially, these elements have the same displacements; however, as delamination occurs, the two shell elements will deform differently, describing the delamination. Figure 4.1 and Figure 4.2 show a single six-noded triangular SIFS element and a cantilever beam discretized with six-noded triangular SIFS elements. Displacements for these SIFS elements are also described only by x and y coordinates, just like the Mindlin-Reissner (MR) elements covered in Section 2.1.1. However, now there is a bottom shell, a top shell, and an interface. The displacements of a SIFS element can be described by the displacements of the bottom and top shells:

$$\mathbf{u_e}(\mathbf{x}) = \begin{bmatrix}\mathbf{u}^- & \mathbf{u}^+\end{bmatrix}^T \tag{4.1}$$

with

$$\mathbf{u}^- = \begin{bmatrix}u^- & v^- & w^- & \theta_x^- & \theta_y^-\end{bmatrix}^T \tag{4.2a}$$

$$\mathbf{u}^+ = \begin{bmatrix}u^+ & v^+ & w^+ & \theta_x^+ & \theta_y^+\end{bmatrix}^T \tag{4.2b}$$

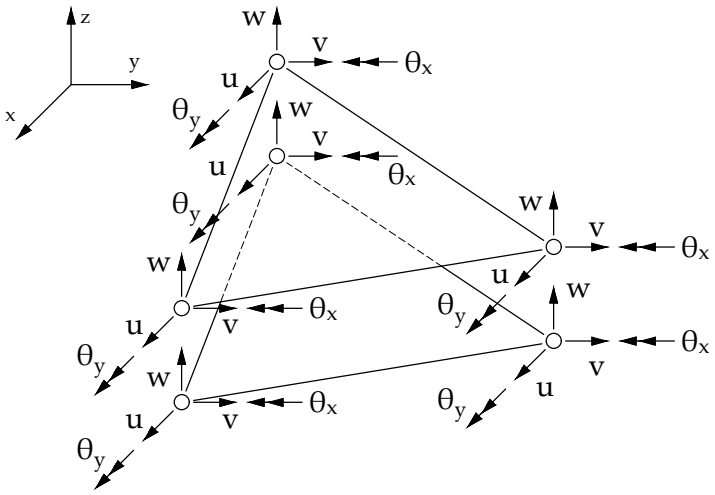

Figure 4.1.: Six-noded triangular SIFS element

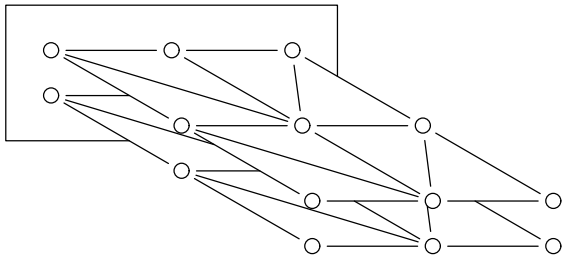

Figure 4.2.: Cantilever beam discretized with SIFS elements

where superscripts - and + denote the bottom and top shell, respectively. Just like MR shells, each shell of a SIFS element has five degrees of freedom. The nodal displacements of a SIFS element can then be defined as:

$$\mathbf{a_e} = \begin{bmatrix} \mathbf{a_e^-} & \mathbf{a_e^+} \end{bmatrix}^T \tag{4.3}$$

with

$$\mathbf{a_e^-} = \begin{bmatrix} a_1^u & a_1^v & a_1^w & a_1^{\theta x} & a_1^{\theta y} & \dots & a_n^u & a_n^v & a_n^w & a_n^{\theta x} & a_n^{\theta y} \end{bmatrix}^T \tag{4.4a}$$

$$\mathbf{a_e^+} = \begin{bmatrix} a_{n+1}^u & a_{n+1}^v & a_{n+1}^w & a_{n+1}^{\theta x} & a_{n+1}^{\theta y} & \dots & a_{2n}^u & a_{2n}^v & a_{2n}^w & a_{2n}^{\theta x} & a_{n2}^{\theta y} \end{bmatrix}^T \tag{4.4b}$$

The strains of a SIFS element introduce a new variable, namely the jump that describes delamination $[\![\mathbf{u}]\!]$. Both the bottom and the top shell of a SIFS element have the same strains as an MR element; however, now displacement jumps corresponding to the interface element are introduced as additional deformations. The strains of a SIFS element can be defined as:

$$\boldsymbol{\epsilon}_e = \begin{bmatrix} \boldsymbol{\epsilon}^- & \boldsymbol{\epsilon}^+ & [\![\mathbf{u}]\!] \end{bmatrix}^T \tag{4.5}$$

with

$$\boldsymbol{\epsilon}^- = \begin{bmatrix} \epsilon_{xx}^- & \epsilon_{yy}^- & 2\epsilon_{xy}^- & \kappa_{xx}^- & \kappa_{yy}^- & 2\kappa_{xy}^- & \gamma_x^- & \gamma_y^- \end{bmatrix}^T \tag{4.6a}$$

$$\boldsymbol{\epsilon}^+ = \begin{bmatrix} \epsilon_{xx}^+ & \epsilon_{yy}^+ & 2\epsilon_{xy}^+ & \kappa_{xx}^+ & \kappa_{yy}^+ & 2\kappa_{xy}^+ & \gamma_x^+ & \gamma_y^+ \end{bmatrix}^T \tag{4.6b}$$

$$[\![\mathbf{u}]\!] = \begin{bmatrix} [\![u]\!]_n & [\![u]\!]_{t,x} & [\![u]\!]_{t,y} \end{bmatrix}^T \tag{4.6c}$$

Following Equation 1.7 and Equation 1.44, the following $\mathbf{B_e}(\mathbf{x})$ can be found:

$$\begin{bmatrix} \boldsymbol{\epsilon}^- \\ \boldsymbol{\epsilon}^+ \\ [\![\mathbf{u}]\!] \end{bmatrix} = \begin{bmatrix} {\mathbf{B^S}^-}_{8x5n} & \mathbf{0}_{8x5n} \\ \mathbf{0}_{8x5n} & {\mathbf{B^S}^+}_{8x5n} \\ {\mathbf{N^{IF}}^-}_{3x5n} & {\mathbf{N^{IF}}^+}_{3x5n} \end{bmatrix} \begin{bmatrix} \mathbf{a}^- \\ \mathbf{a}^+ \end{bmatrix} \tag{4.7}$$

with

$$\mathbf{B^{S\pm}} = \begin{bmatrix} N_{i,x} & 0 & 0 & 0 & 0 & \dots & N_{j,x} & 0 & 0 & 0 & 0 \\ 0 & N_{i,y} & 0 & 0 & 0 & \dots & 0 & N_{j,y} & 0 & 0 & 0 \\ N_{i,y} & N_{i,x} & 0 & 0 & 0 & \dots & N_{j,y} & N_{j,x} & 0 & 0 & 0 \\ 0 & 0 & 0 & N_{i,x} & 0 & \dots & 0 & 0 & 0 & N_{j,x} & 0 \\ 0 & 0 & 0 & 0 & N_{i,y} & \dots & 0 & 0 & 0 & 0 & N_{j,x} \\ 0 & 0 & 0 & N_{i,y} & N_{i,x} & \dots & 0 & 0 & 0 & N_{j,y} & N_{j,x} \\ 0 & 0 & N_{i,x} & N_i & 0 & \dots & 0 & 0 & N_{j,x} & N_j & 0 \\ 0 & 0 & N_{i,y} & 0 & -N_i & \dots & 0 & 0 & N_{j,y} & 0 & -N_j \end{bmatrix} \tag{4.8a}$$

$$\mathbf{N^{IF-}} = \begin{bmatrix} -N_1 & 0 & 0 & 0 & 0 & \dots & -N_n & 0 & 0 & 0 & 0 \\ 0 & -N_1 & 0 & 0 & 0 & \dots & 0 & -N_n & 0 & 0 & 0 \\ 0 & 0 & -N_1 & 0 & 0 & \dots & 0 & 0 & -N_n & 0 & 0 \end{bmatrix} \tag{4.8b}$$

$$\mathbf{N^{IF+}} = \begin{bmatrix} N_{n+1} & 0 & 0 & 0 & 0 & \dots & N_{2n} & 0 & 0 & 0 & 0 \\ 0 & N_{n+1} & 0 & 0 & 0 & \dots & 0 & N_{2n} & 0 & 0 & 0 \\ 0 & 0 & N_{n+1} & 0 & 0 & \dots & 0 & 0 & N_{2n} & 0 & 0 \end{bmatrix} \tag{4.8c}$$

where subscripts i and j in $\mathbf{B^{S\pm}}$ correspond to node 1 to node n for the bottom shell $S-$, and node $n+1$ to node $2n$ for the top shell $S+$, respectively.

Subsequently, the internal force vector, element stiffness matrices, and global stiffness matrix can be assembled following Equation 1.10 to Equation 1.13.

4.1.2. Mesoscale Formulation

On the mesoscale, 3D solid elements and interface elements are applied. Section 1.4 and Section 1.7 cover the formulation of these elements. A new term for these RVEs, which include interface elements, is introduced in the work of Herwig and Wagner [8], namely *coupled Representative Volume Elements*, or *cRVEs*. Figure 4.3 shows the mesoscale cRVE, consisting of eight-noded brick elements and eight-noded interface elements. Again, only these cRVEs will initially capture the material properties and thickness of the laminate.

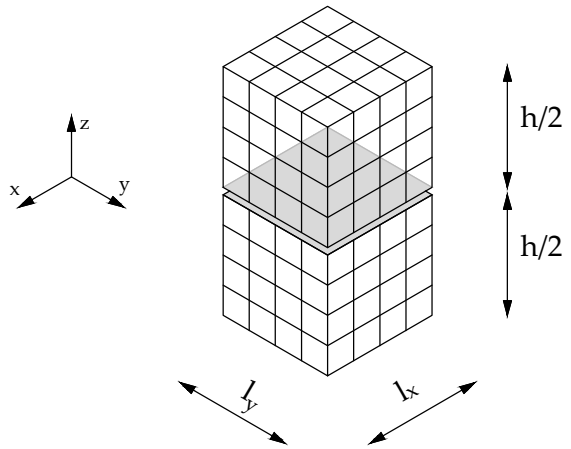

Figure 4.3.: cRVE with 3D solid and interface elements

4.1.3. Scale Coupling

The macro- and mesoscales are again coupled by setting boundary conditions on the cRVE. The boundary conditions set on the cRVE are a combination of the boundary conditions applied in the works of Gruttman and Wagner [7], and Herwig and Wagner [8]. These boundary conditions are a set of linear boundary conditions and periodic boundary conditions.

Similar to Section 2.1.3, linear boundary conditions constraining the horizontal degrees of freedom, u and v, are applied over the edges of the cRVE. However, now the cRVE has a bottom and a top part, split by the interface elements. This bottom and top part correspond to the bottom and top parts of the SIFS element. Furthermore, the linear boundary conditions will need to capture the transverse jumps described by the interface elements. Another linear boundary condition needs to fix the cRVE in the z-direction. Seeing as a cRVE has interface elements capable of describing a jump in the normal direction, fixing the cRVE in the z-direction will be done differently than in Section 2.1.3. Now, instead of a single node in the middle of the cRVE, there are two nodes, which are both part of the same interface elements. The linear boundary condition will need to describe the normal jump between the

bottom and top parts of the cRVE. The linear boundary conditions on the cRVE are defined as:

$$\begin{bmatrix} u_b \\ v_b \end{bmatrix}_m^- = \begin{bmatrix} x & 0 & \frac{1}{2}y & xz & 0 & \frac{1}{2}yz & z & 0 & 0 & -\frac{1}{2} & 0 \\ 0 & y & \frac{1}{2}x & 0 & yz & \frac{1}{2}xz & 0 & z & 0 & 0 & -\frac{1}{2} \end{bmatrix}_m \begin{bmatrix} \boldsymbol{\epsilon}^- \\ [\![\mathbf{u}]\!] \end{bmatrix}_M \tag{4.9a}$$

$$\begin{bmatrix} u_b \\ v_b \end{bmatrix}_m^+ = \begin{bmatrix} x & 0 & \frac{1}{2}y & xz & 0 & \frac{1}{2}yz & z & 0 & 0 & +\frac{1}{2} & 0 \\ 0 & y & \frac{1}{2}x & 0 & yz & \frac{1}{2}xz & 0 & z & 0 & 0 & +\frac{1}{2} \end{bmatrix}_m \begin{bmatrix} \boldsymbol{\epsilon}^+ \\ [\![\mathbf{u}]\!] \end{bmatrix}_M \tag{4.9b}$$

$$\begin{bmatrix} w_{mid}^- \\ w_{mid}^+ \end{bmatrix}_m = \begin{bmatrix} -\frac{1}{2} & 0 & 0 \\ +\frac{1}{2} & 0 & 0 \end{bmatrix} [[\mathbf{u}]]_M \tag{4.9c}$$

Note that this linear boundary condition describing the normal jump, Equation 4.9c, violates the Hill-Mandel macro-homogeneity principle, see Equation 1.6. The average strain (normal jump) in the cRVE isn't necessarily equal to the strain on the macroscale. Applying a linear boundary condition that does satisfy this Hill-Mandel principle will constrain the cRVE in the vertical direction for all the interface nodes. This, however, will also prevent the two shell parts of the cRVE from bending properly and thus overconstrain the cRVE. Appendix B of Wieringa's thesis [23] shows how this constant normal jump in the cRVE influences the stiffness components for Timoshenko beam elements. The cRVE will no longer be able to properly capture the extensional stiffness, which will be overly stiff. This work will continue with the linear boundary condition that only constrains a single duplicate node in the middle of the cRVE.

Lastly, the cRVE will also need to be constrained from rotation about the x and y axes. This is done by setting the periodic boundary conditions described in Section 2.1.3, see Equation 2.14.

Figure 4.4 shows the proposed deformations of the cRVE, following the applied boundary conditions. Note that the top and bottom parts of the cRVE have the same strains applied to them ($\boldsymbol{\epsilon}^- = \boldsymbol{\epsilon}^+$); however, this does not have to be the case.

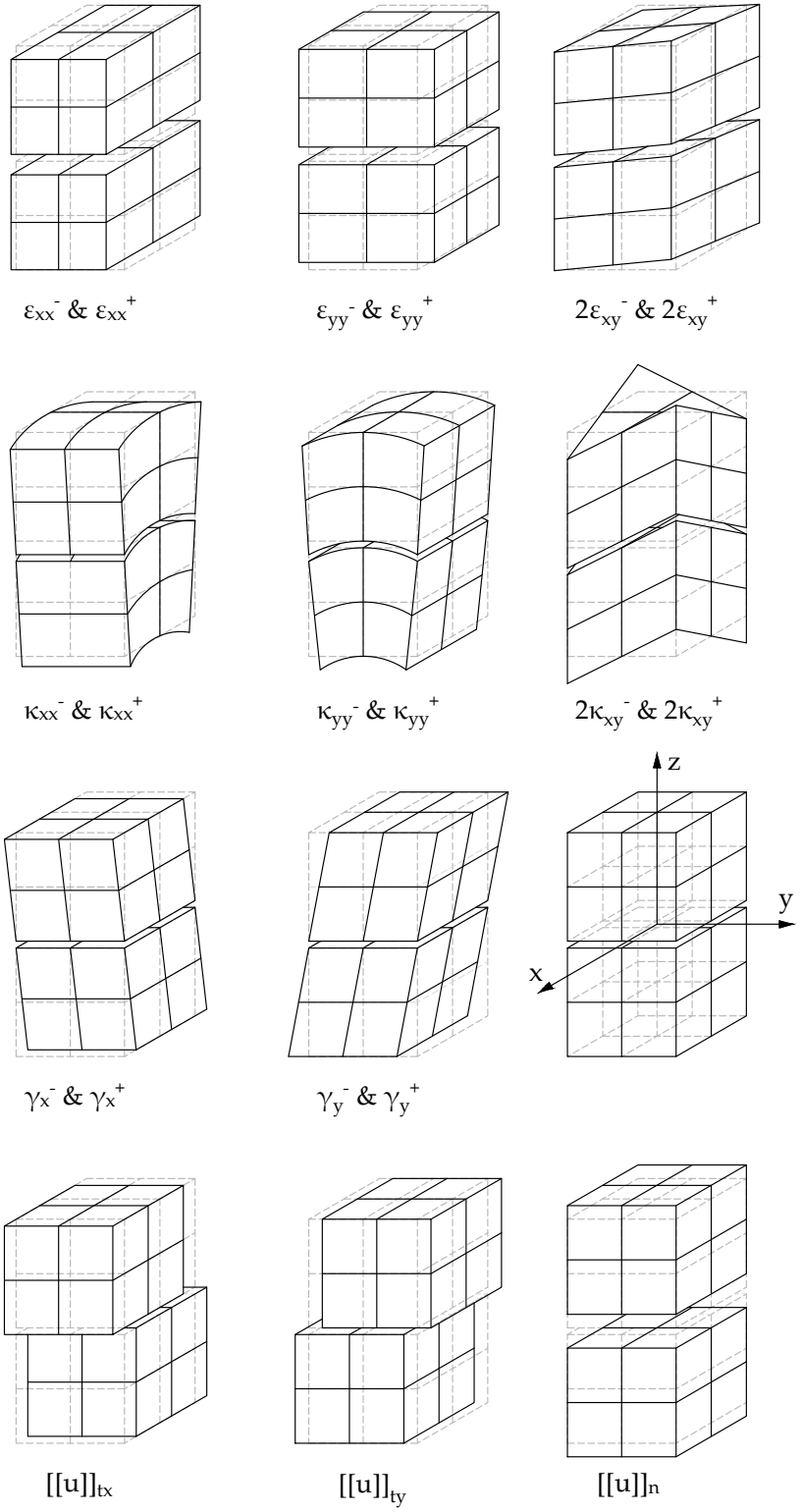

Figure 4.4.: cRVE kinematics

4.2. Load Cases

To verify the multiscale framework with the inclusion of delamination, several load cases are introduced, which will be tested on the framework. Firstly, Unit Tests will be performed to determine whether the proposed TSL is properly incorporated. Unit Tests for both Mode-I and Mode-II delamination will be performed, as well as a Mixed-Mode Unit Test. The Unit Test will consist of a single SIFS element with an area of 1 mm^2. The bottom nodes of the SIFS elements will be constrained in all degrees of freedom. For the Mode-I Unit Test, only the degree of freedom w of the top nodes will have a prescribed deformation. The other degrees of freedom will be constrained. For the Mode-II Unit Tests, only the degree of freedom u or v of the top nodes will have a prescribed deformation. The other degrees of freedom will be constrained. Lastly, for the Mixed-Mode Unit Test, the degrees of freedom u, v, and w will have the same prescribed deformation. All other degrees of freedom will be constrained.

To further verify the multiscale framework, three additional load cases will be analysed and compared to 3D DNS analyses. The following load cases will be analysed:

- Double Cantilever Beam Test (DCB)
- End-Notched Flexure Test (ENF)
- Single-Leg Bending Test (SLB)

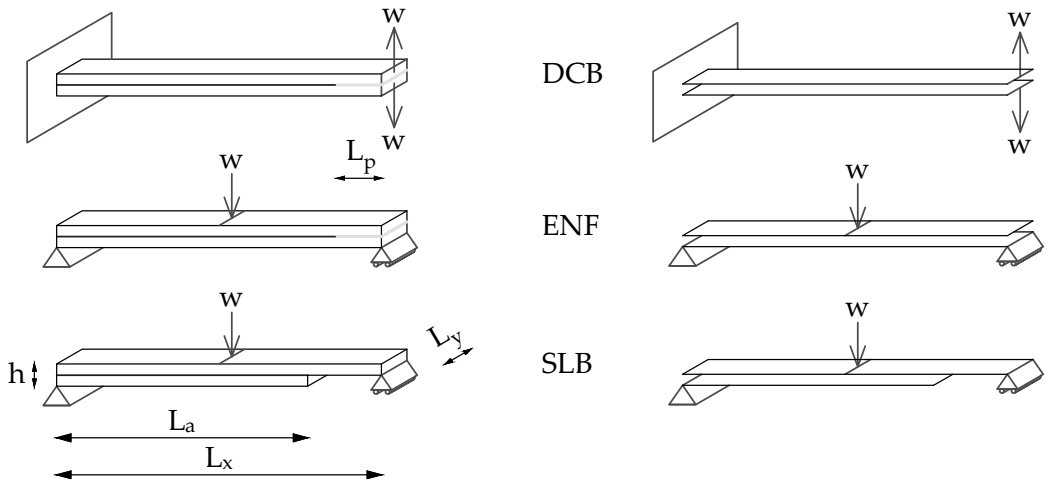

(a) Load cases for 3D analyses

(b) Load cases for FE^2 analyses

Figure 4.5.: Load cases

Figure 4.5 shows the load cases that will be analysed. Table 4.1 shows the geometry of the beams for the three additional load cases and the interlaminar material properties for the interface. The intralaminar properties of the material are taken from Table 2.1 for the isotropic ply configuration and Table 3.1 for the other ply configurations. Four different ply configurations will be analysed for each load case. The following ply configurations will be analysed:

- Isotropic
- 0
- $0/90_2/0$
- 45/-45

Double Cantilever Beam Test
A *Double Cantilever Beam Test*, or *DCB Test*, is often performed to determine Mode-I interlaminar fracture toughness in a laminate [2]. A beam is clamped at one end, whereas the other end is loaded at the top and bottom surfaces in opposite directions, splitting the laminate in two. Typically, an initial pre-crack is applied to control where the delamination will occur. The top of Figure 4.5a shows the configuration for the 3D analyses of the DCB Tests. For the 3D analyses, the beam will be clamped at one end by setting deformations at the surface u, v, and w to 0. On the other end, the top half and bottom half of the surface area will have a prescribed deformation w in opposite direction. The top of Figure 4.5b shows the configuration for the SIFS analyses of the DCB Tests. For the SIFS analyses, the beam will also be clamped at one end by setting the deformations u, v, w, and θ_x to 0. The other end will have a prescribed deformation of w on the top and bottom edges in opposite directions.

End-Notched Flexure Test
An *End-Notched Flexure Test*, or *ENF Test*, is often performed to determine Mode-II interlaminar fracture toughness in a laminate [1]. A beam is subjected to three-point bending, as described in Section 2.2, to induce a delamination. The beam will also typically have an initial pre-crack to control where the delamination will occur. The middle of Figure 4.5a shows the configuration for the 3D analyses of the ENF Tests. For the 3D analyses, the boundary and loading conditions for the ENF Test are similar to those of the three-point bending beam, described in Section 2.2. The middle of Figure 4.5b shows the configuration for the SIFS analyses of the ENF Tests. For the SIFS analyses, only the bottom edges at x = 0 and x = L will be supported in w, where at x = 0, the bottom edge is also supported in u and v. Furthermore, the top shell will be loaded with a prescribed deformation w at x = L/2.

Single-Leg Bending Test
A *Single-Leg Bending Test*, or *SLB Test*, is performed to determine Mixed-Mode interlaminar fracture properties in a laminate [13]. The SLB Test is similar to the ENF Test, in which a three-point bending test is performed on a beam. However, for an SLB Test, a segment of the bottom part of the beam is removed at an edge. The bottom of Figure 4.5a shows the configuration for the 3D analyses of the SLB Tests. For the 3D analyses, the beam is supported in u, v, and w at the left bottom edge and in w at the right bottom edge. The bottom of Figure 4.5b shows the configuration for the SIFS analyses of the SLB Tests. For the SIFS analyses, the beam is supported in u, v, and w on the bottom left edge and in w on the top right edge. Both 3D and SIFS analyses will have a prescribed deformation of w in the middle of the beam's span at the top.

	Variable	Value	Unit
Geometry	L_x	100	mm
	L_y	1	mm
	L_p	10	mm
	L_a	70	mm
	h	8	mm
Interlaminar material properties	K_d	50,000	N/mm^3
	F_n	80	N/mm^2
	F_t	100	N/mm^2
	G_I	0.969	N/mm
	G_{II}	1.719	N/mm
	η_l	2.284	-
cRVE geometry	width	0.05	mm
	$n_{elems,x\&y}$	2	-
	$n_{elems,z}$	80	-
	$d_{x\&y}$	0.025	mm
	d_z	0.01	mm
DCB	$n_{elems,x}$	400	-
	$n_{elems,y}$	4	-
	$n_{elems,z}$	32	-
	d_x	0.25	mm
	d_y	0.25	mm
	d_z	0.25	mm
ENF	$n_{elems,x}$	200	-
	$n_{elems,y}$	2	-
	$n_{elems,z}$	16	-
	d_x	0.5	mm
	d_y	0.5	mm
	d_z	0.5	mm
SLB	$n_{elems,x}$	200	-
	$n_{elems,y}$	2	-
	$n_{elems,z}$	16	-
	$n_{elems,a}$	140	-
	d_x	0.5	mm
	d_y	0.5	mm
	d_z	0.5	mm

Table 4.1.: Parameter list

4.3. Results

Unit Tests and three additional load cases are tested for the FE^2 framework. Section 4.3.1 covers the results of the Unit Tests for Mode-I, Mode-II, and Mixed-Mode delamination. These results are compared to analytical values. Section 4.3.2, Section 4.3.3 and Section 4.3.4 cover the results of the DCB, ENF, and SLB Tests, respectively. These results are compared to the results of 3D DNS analyses.

4.3.1. Unit Tests

Unit Tests in Mode-I, Mode-II, and Mixed-Mode are performed to determine whether the FE^2 framework properly follows the TSL proposed by Turon. Analytical solutions are derived from Section 1.7. For Mode-II, two Unit Tests were performed, namely for x and y directions. The results of these analyses have the same exact output (both for the analytical and the FE^2 analyses) and are therefore only shown once.

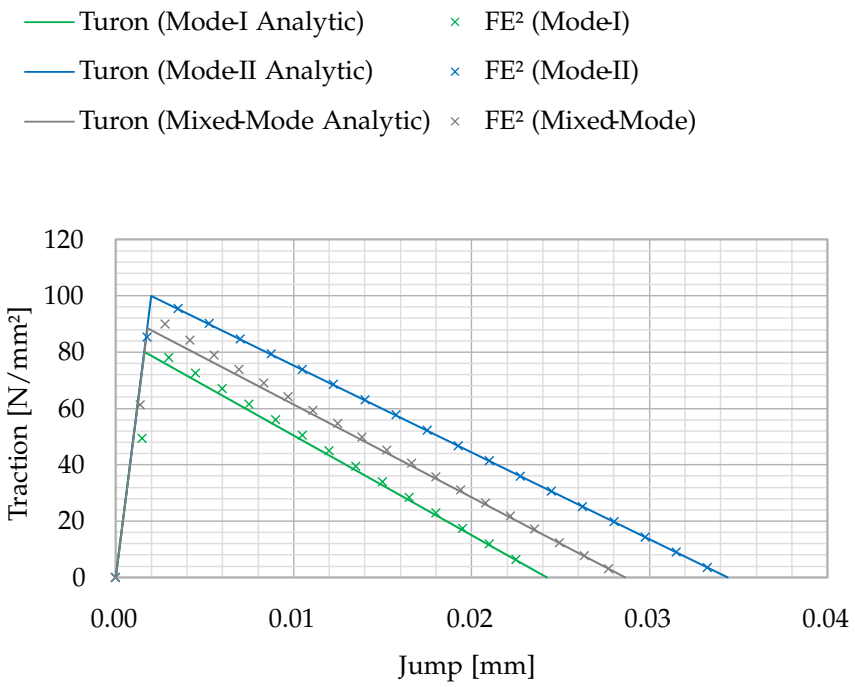

Figure 4.6.: Load-displacement graph for Unit Tests

Figure 4.6 shows the load-displacement graph for the Unit Tests in Mode-I, Mode-II, and Mixed-Mode in the form of tractions on the surface area of the shell elements and the jump of the two shell elements. The FE^2 analyses follow the analytical values quite well; however, they are not exact. For Mode-I and Mixed-Mode delamination, there are notable differences in the values of the load-displacement graph. These differences are also there for the Mode-II delamination, however much smaller and not noticeable in the graph. The differences can

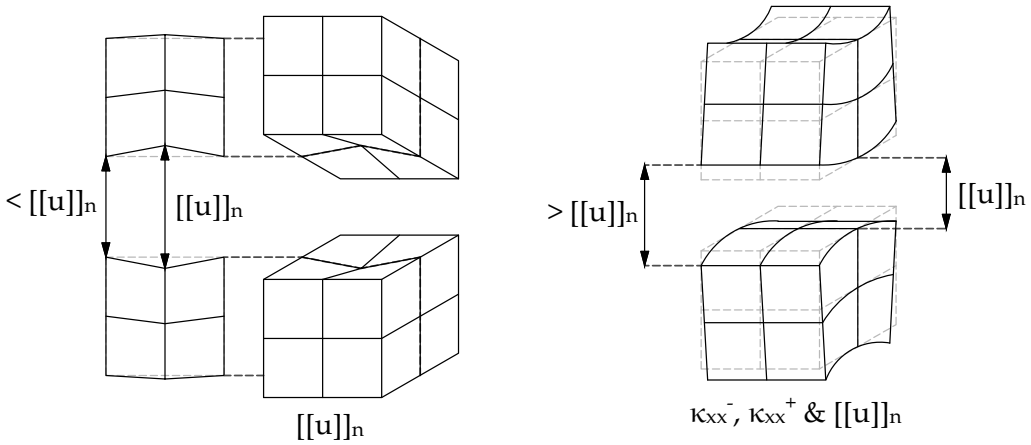

(a) Mode-I delamination with cross-section (b) Mode-I delamination and bending

Figure 4.7.: Deformation modes of the cRVE

be explained by the violation of the Hill-Mandel macro-homogeneity principle. For Mode-I, only the two middle nodes of the interface are subjected to the normal jump. This results in a lower initial dummy stiffness, K_d, which can be seen in the graph. A similar explanation can be given for the initial dummy stiffness in the transverse directions, as only the boundary nodes are subjected to the transverse jumps. To satisfy the Hill-Mandel macro-homogeneity principle, all the nodes that belong to interface elements should be subjected to normal and transverse jumps. However, in doing so, the cRVE will not be able to properly capture the bending deformation. Figure 4.7 shows how the cRVE truly deforms under pure Mode-I delamination and how it will deform under a combination of Mode-I delamination and bending in opposite directions of the two shell parts.

4.3.2. Double-Cantilever Beam

DCB Tests with different ply configurations are performed to determine the accuracy of a Mode-I-dominated load case. Two types of DCB Tests are performed to verify the multiscale framework's accuracy and to show the model's limitations.

Figure 4.8 shows the load-displacement graph for DCB Tests without an initial pre-crack. Note that the ASTM Standard for performing DCB Tests requires the beam to have a pre-crack [2]. Immediately, it is clear that the FE^2 analyses are not following the same path as the 3D DNS analyses for the anisotropic ply configurations. The load-displacement curves are initially much stiffer and reach a higher ultimate load than the 3D DNS analyses. However, once the model is sufficiently damaged, the FE^2 analyses perform quite well.

The main reason for the large differences in the analyses can be explained by the model formulations of the macroscale models. The FE^2 analyses with SIFS elements incorporating

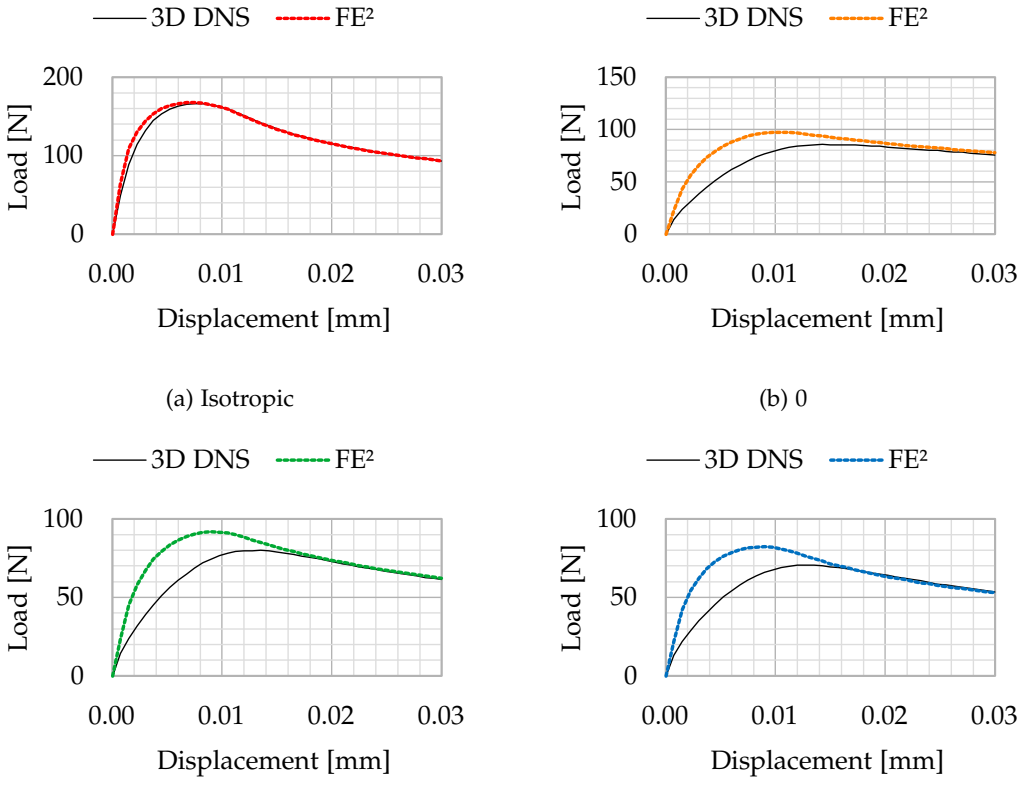

(a) Isotropic

(b) 0

(c) $0/90_2/0$

(d) 45/-45

Figure 4.8.: Load-displacement graphs for DCB Tests with different ply configurations without a pre-crack

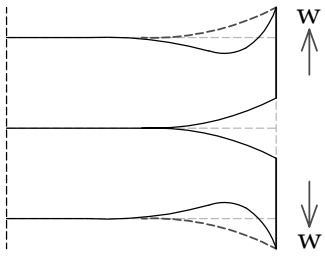

Figure 4.9.: Local deformation in DCB Test without a pre-crack

Mindlin-Reissner shell elements assume a constant displacement over the height of the element, whereas this is not the case for the 3D DNS analyses. This, in turn, results in stiffer outcomes for the shell elements. Figure 4.9 shows how a large local deformation over the height will occur for the 3D DNS analyses; however, for shell elements, this deformation is constrained. These local deformations in the 3D DNS analyses are due to the relatively low values of the material properties related to the vertical displacement (E_3, G_{23}, and G_{31}), which also explains why the isotropic analysis shows better results due to the relatively higher values for these material properties. Initially, shear forces at the end of the beam are tearing the plies apart; however, once a sufficient delamination length is achieved, these forces are overshadowed by the resulting moments. The bottom and top delaminated plies act as lever arms for the forces to create extra bending moments in the interface. Once the bending moments take over, the results are much more accurate. The shear forces will no longer result in large local deformations over the beam height.

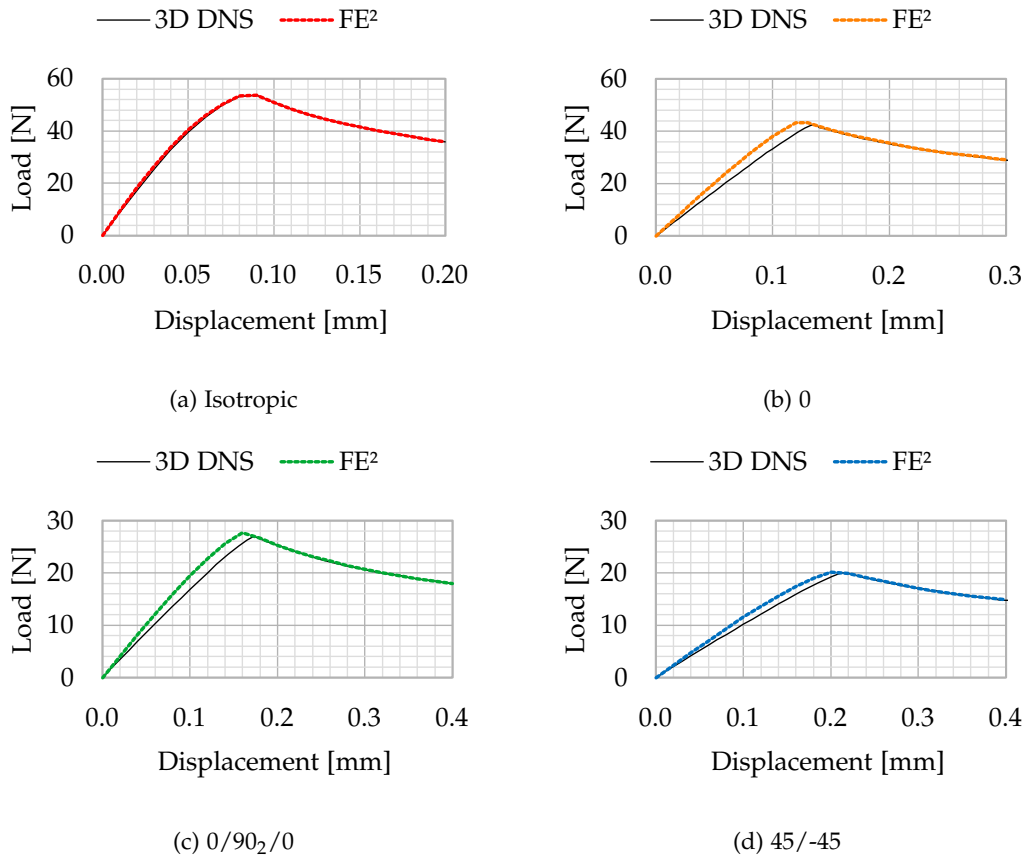

(a) Isotropic

(b) 0

(c) $0/90_2/0$

(d) 45/-45

Figure 4.10.: Load-displacement graphs for DCB Tests with different ply configurations with a pre-crack

Figure 4.10 shows the load-displacement graph for DCB Tests with an initial pre-crack. Now, the FE^2 analyses are much more accurate compared to the DCB without the pre-crack. It is, however, still noticeable that the initial stiffness is a bit on the higher side and that the maximum load is also a bit higher for the FE^2 analyses. This is still due to the same difference

in kinematic assumptions for the macroscale models. However, now the differences in initial stiffness and maximum load are significantly smaller and within an acceptable range of about 10%.

DCB without pre-crack				
		Control	Steps	Iterations
Isotropic	3D DNS FE^2	Displacement Displacement	40 40	87 87
0	3D DNS FE^2	Displacement Displacement	40 40	78 85
$0/90_2/0$	3D DNS FE^2	Displacement Displacement	40 40	67 83
45/-45	3D DNS FE^2	Displacement Displacement	40 40	110 95
DCB with pre-crack				
		Control	Steps	Iterations
Isotropic	3D DNS FE^2	Arc-length Displacement	20 20	66 58
0	3D DNS FE^2	Arc-length Displacement	53 30	136 99
$0/90_2/0$	3D DNS FE^2	Arc-length Displacement	37 20	95 77
45/-45	3D DNS FE^2	Arc-length Displacement	54 20	166 96

Table 4.2.: Convergence properties DCB

Another interesting aspect of the DCB analyses are the convergence properties. Table 4.2 shows some of these properties for the DCB analyses. The analyses for the DCB without an initial pre-crack all found a converged solution when applying the same displacement-controlled increment. The total number of iterations for the 3D DNS and FE^2 analyses does not differ much between these analyses. For the DCB analyses with an initial pre-crack, most of the 3D DNS analyses did not find a converged solution with the displacement control method. The arc-length method was applied to find converged solutions. Now, when comparing the 3D DNS analyses with the FE^2 analyses, the number of steps and iterations starts to differ. The FE^2 analyses converged with relatively large load increment steps and fewer iterations. This results in faster analyses for the FE^2 analyses.

4.3.3. End-Notched Flexure

ENF Tests with different ply configurations are performed to determine the accuracy of a Mode-II-dominated load case. The 3D DNS analyses are performed with an arc-length solver to capture the snapback behaviour of the models. This arc-length method is, however, not within the scope of this work and is not implemented for the FE^2 analyses. Figure 4.11 shows the results of the ENF Tests. The load-displacement graphs for the ENF Tests show three distinct paths, namely the initial stiffness, the delamination, and the secondary stiffness. Only Figure 4.11c for the $0/90_2/0$ ply configuration shows part of the delamination path for the FE^2 analysis. This is due to the fact that the FE^2 analysis uses the displacement

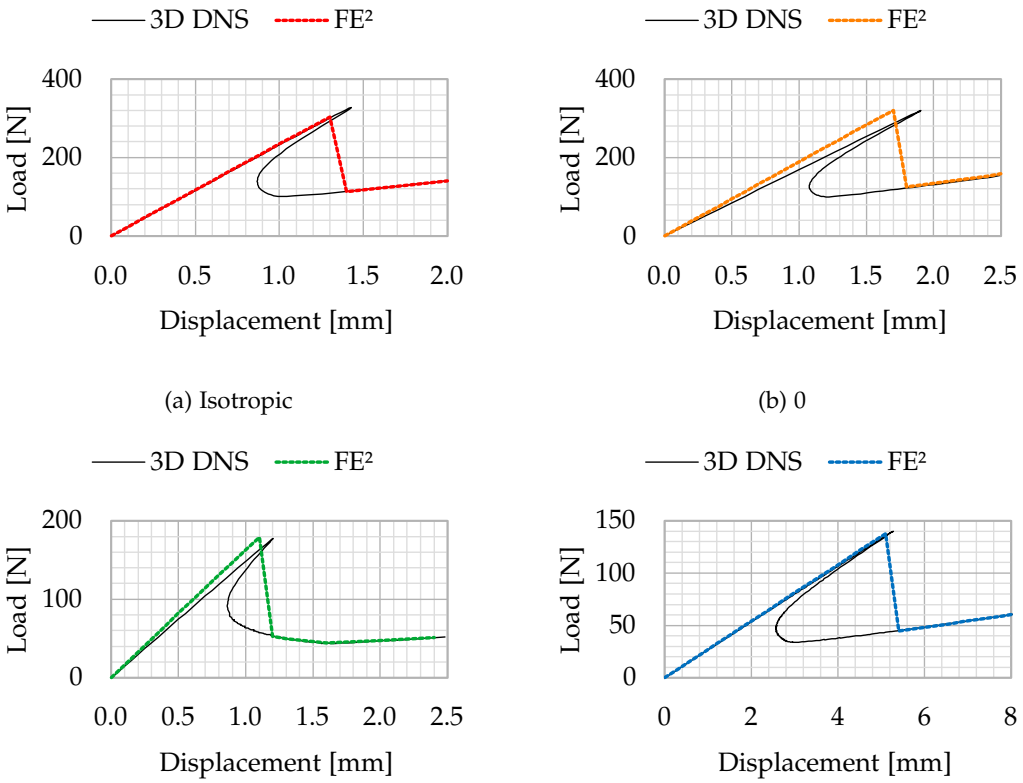

(a) Isotropic

(b) 0

(c) $0/90_2/0$

(d) 45/-45

Figure 4.11.: Load-displacement graphs for ENF Tests with different ply configurations

		Control	Steps	Iterations
Isotropic	3D DNS	Arc-length	81	254
	FE^2	Displacement	20	88
0	3D DNS	Arc-length	101	353
	FE^2	Displacement	25	100
$0/90_2/0$	3D DNS	Arc-length	131	462
	FE^2	Displacement	6	104
45/-45	3D DNS	Arc-length	301	976
	FE^2	Displacement	27	190

Table 4.3.: Convergence properties ENF

control method, and the delamination path is still occurring at the displacement increment after the peak load. All results show a higher initial stiffness for the FE^2 analyses. After the delamination occurs, the secondary stiffness of the FE^2 analyses is also higher than the 3D DNS analyses, but significantly less so. These differences can again be explained by the difference in kinematic assumptions for the macroscale models.

Table 4.3 shows convergence properties for the ENF analyses. The arc-length method is applied for the 3D DNS analyses to capture the snapback behaviour of the model. Due to the snapback behaviour of the ENF, many more time steps were necessary to fully capture this behaviour for the 3D DNS analyses. However, many more iterations were also necessary at the point of snapback for the FE^2 analyses. It is clear from the results in the table that the FE^2 analyses need a lot fewer iterations to find a converged solution. It is, however, unfair to compare these analyses when it comes to convergence, considering the 3D DNS analyses show much more elaborate results due to the capture of snapback behaviour.

4.3.4. Single-Leg Bending

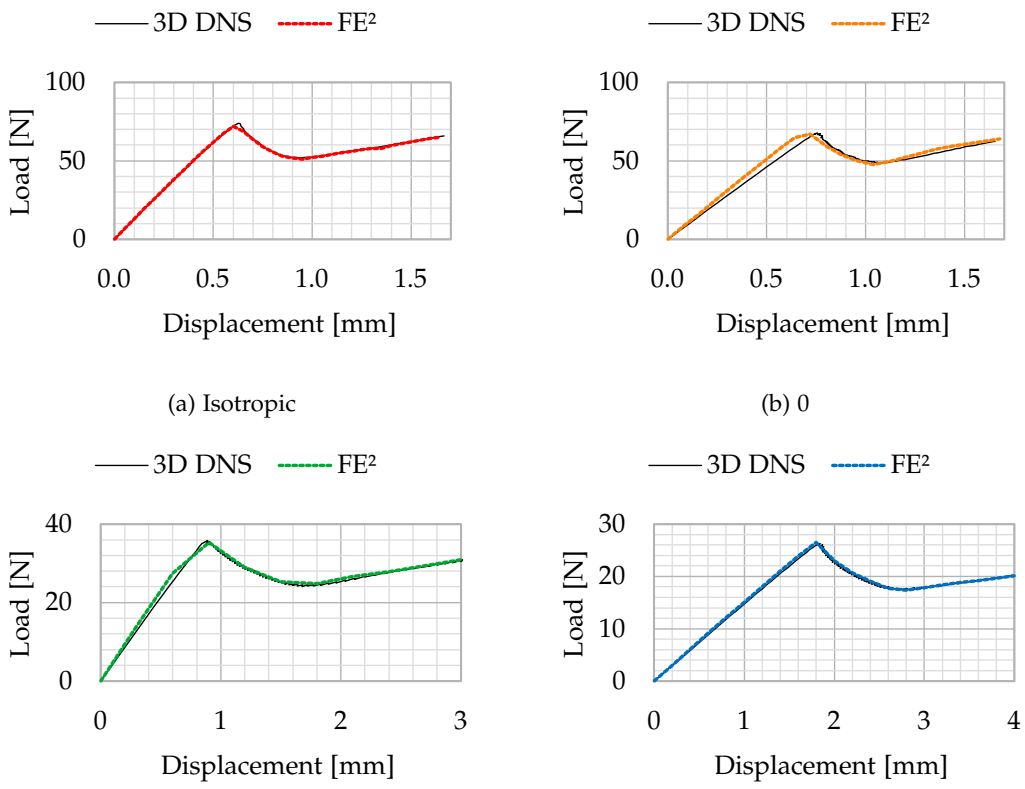

(a) Isotropic

(b) 0

(c) $0/90_2/0$

(d) 45/-45

Figure 4.12.: Load-displacement graphs for SLB Tests with different ply configurations

To include a load case that incorporates both Mode-I and Mode-II delamination, SLB Tests are performed for different ply configurations. The results of this Mixed-Mode test are shown in Figure 4.12. Only Figure 4.12b for the 0 ply configuration shows a noticeable difference in values; however, this difference is anything but significant. The FE^2 analyses show near-perfect results compared to the 3D analyses. It can be noted again, however, that the initial stiffness of the FE^2 analyses is slightly higher. This is again a consequence of the Mindlin-Reissner formulation, where the displacement over the height of the shell is constant.

		Control	Steps	Iterations
Isotropic	3D DNS	Arc-length	76	270
	FE^2	Displacement	17	130
0	3D DNS	Arc-length	120	441
	FE^2	Displacement	21	227
$0/90_2/0$	3D DNS	Arc-length	131	480
	FE^2	Displacement	10	133
45/-45	3D DNS	Arc-length	177	629
	FE^2	Displacement	20	153

Table 4.4.: Convergence properties SLB

Table 4.4 shows convergence properties for the SLB analyses. Just like for the 3D DNS analyses of the DCB with an initial pre-crack, applying a displacement-controlled increment did not lead to a converged solution for the 3D DNS analyses of the SLB. Again, to overcome this, the arc-length method was applied to find converged solutions for the 3D DNS analyses. Now, the FE^2 analyses show much better convergence properties. Not only do the FE^2 analyses find converged solutions with the displacement-controlled method, but far fewer steps and iterations are necessary to get a converged solution. For the SLB analyses, when comparing the 3D DNS analyses with the FE^2 analyses, the number of steps and iterations really starts to differ. The FE^2 analyses converged with relatively large load increment steps and fewer iterations, while still showing similarly accurate results as the 3D DNS analyses.

4.4. Concluding Remarks

The multiscale framework coupling SIFS elements and cRVEs with 3D solid and interface elements has been tested on numerous load cases and compared to analytical solutions or 3D DNS analyses. In general, the FE^2 analyses show similar results to the analytical solutions or the 3D DNS analyses; however, some significant differences can be observed.

For the Unit Tests, a lower initial dummy stiffness K_d is observed for all analyses. Primarily, the Mode-I dummy stiffness is notably lower for the FE^2 analyses due to the violation of the Hill-Mandel macro-homogeneity principle. This violation is, however, necessary to properly deform the bottom and top parts of the cRVE in bending. However, the differences in the initial dummy stiffness do not influence the model significantly, and accurate results are still obtained.

Furthermore, the FE^2 analyses for the DCB, ENF, and SLB Tests mostly show an initially higher stiffness. This is a consequence of the Mindlin-Reissner formulation, in which the vertical displacement is constant over the height of the shell, resulting in stiffer responses

than 3D analyses. The models of the 3D analyses can have a varying vertical displacement over the height of the model. The result of this phenomenon is especially noticeable for the analyses of the DCB Test without an initial pre-crack, where the initial stiffness is much higher for the FE^2 analyses. The DCB Test with an initial pre-crack, ENF, and SLB Tests show that the force at which the structure is permanently damaged is quite accurate; however, the displacement corresponding to this force is often a bit too low. This is a direct result of the stiffer FE^2 analyses.

Another important aspect of the multiscale framework is how the cRVE contributes to the convergence properties of the analyses. Some of the 3D DNS analyses needed many fine displacement increments or even the application of the arc-length method to converge, whereas the FE^2 analyses all converged without much configuring of the loading properties. Seeing as the cRVE needs to be sufficiently narrow to properly capture the shear stiffness components, the interface elements will also have a small surface area, contributing to better convergence properties. Furthermore, the FE^2 analyses showed better convergence properties as the load cases and ply configurations became more complex.

Overall, good results were obtained from the multiscale framework. The load-displacement graphs show similar paths for all analyses, with the exception of the DCB Test without an initial pre-crack due to inconsistent model kinematics.

5. ASTM Double-Cantilever Beam Test

In this chapter, Double-Cantilever Beam (DCB) Tests are performed following ASTM standards [2]. The configuration for the DCB Tests is determined following the sensitivity studies in Appendix A. DCB Tests will be performed for different ply configurations. The results of the DCB Tests will be compared to those of the 3D DNS analyses. The chapter will again end with the results and the concluding remarks.

5.1. Configuration

Following the sensitivity studies in Appendix A for the macroscale mesh, the mesoscale mesh, and the RVE width, the following mesh configuration is employed for the DCB Tests following the ASTM standards: Figure 5.1 shows the mesh configuration for the DCB Tests.

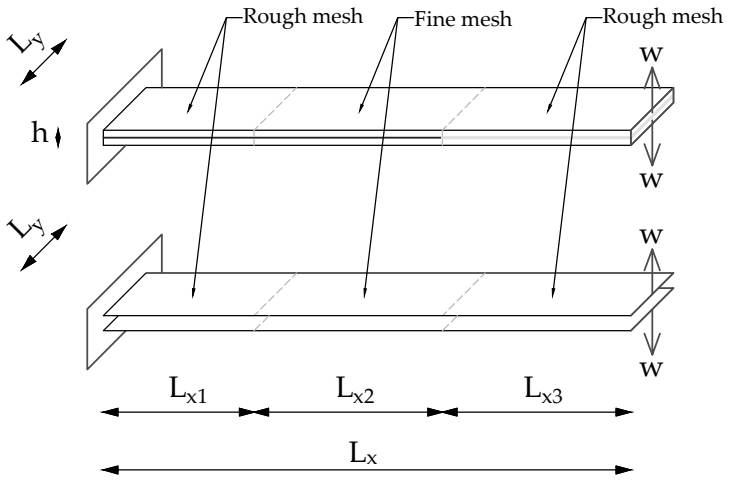

Figure 5.1.: Mesh configuration for the DCB Test

To save on computational time, the beam is divided into three parts over the length L_x, namely L_{x1} at the clamp, L_{Lx2} where the crack will propagate, and L_{x3} at the pre-crack. The area where the crack will initiate, L_{x2}, requires a finer mesh for accurate results compared to the area at the clamp, L_{x1}, and the pre-crack, L_{x3}. Table 5.1 shows the discretization parameters for the beam and the cRVE.

	Variable	Value	Unit
Mesh geometry	L_x	140	mm
	L_{x1}	40	mm
	L_{x2}	50	mm
	L_{x3}	50	mm
	L_y	20	mm
	h	4	mm
	$n_{elems,x1}$	20	-
	$n_{elems,x2}$	100	-
	$n_{elems,x3}$	25	-
	$n_{elems,y}$	10	-
	$n_{elems,z}$	8	-
	d_{x1}	1	mm
	d_{x2}	0.5	mm
	d_{x3}	1	mm
	d_y	2	mm
	d_z	0.5	mm
cRVE geometry	width	0.025	mm
	$n_{elems,x\&y}$	2	-
	$n_{elems,z}$	80	-
	$d_{x\&y}$	0.0125	mm
	d_z	0.05	mm

Table 5.1.: Parameter list

The following ply configurations will be analysed:

- Isotropic
- 0
- $0/90_2/0$
- 45/-45

The isotropic material properties, orthotropic material properties, and interlaminar material properties are taken from Table 2.1, Table 3.1, and Table 4.1, respectively.

5.2. Results

Figure 5.2 shows the load-displacement graphs for the DCB Tests. These graphs are very similar to the results in Section 4.3 for the DCB Tests with an initial pre-crack, see Figure 4.10. One notable difference, however, is the initial stiffness of the results. In Section 4.3, the FE^2 analyses show a higher initial stiffness, whereas the FE^2 analyses in Figure 5.2 show a lower initial stiffness when comparing these to the 3D analyses. This is likely due to the applied mesh. The analyses in Section 4.3 employ a relatively finer mesh than the analyses presented here. Considering that the 3D analyses show a steeper convergence rate than the Mindlin-Reissner analyses when refining the macroscale mesh, it is possible that the 3D analyses in this chapter have not yet converged enough. Although possible, employing a finer mesh will

result in significantly longer computational time. The additional analyses presented in this chapter truly show the significance of the multiscale framework when it comes to analysing structures with a complex material model on the meso- or microscale. For the 3D analyses, a significant number of elements are necessary to properly capture the stresses, strains, and deformations over the thickness of the structure. Additionally, the element aspect ratio also plays an important role, resulting in an even larger number of elements necessary.

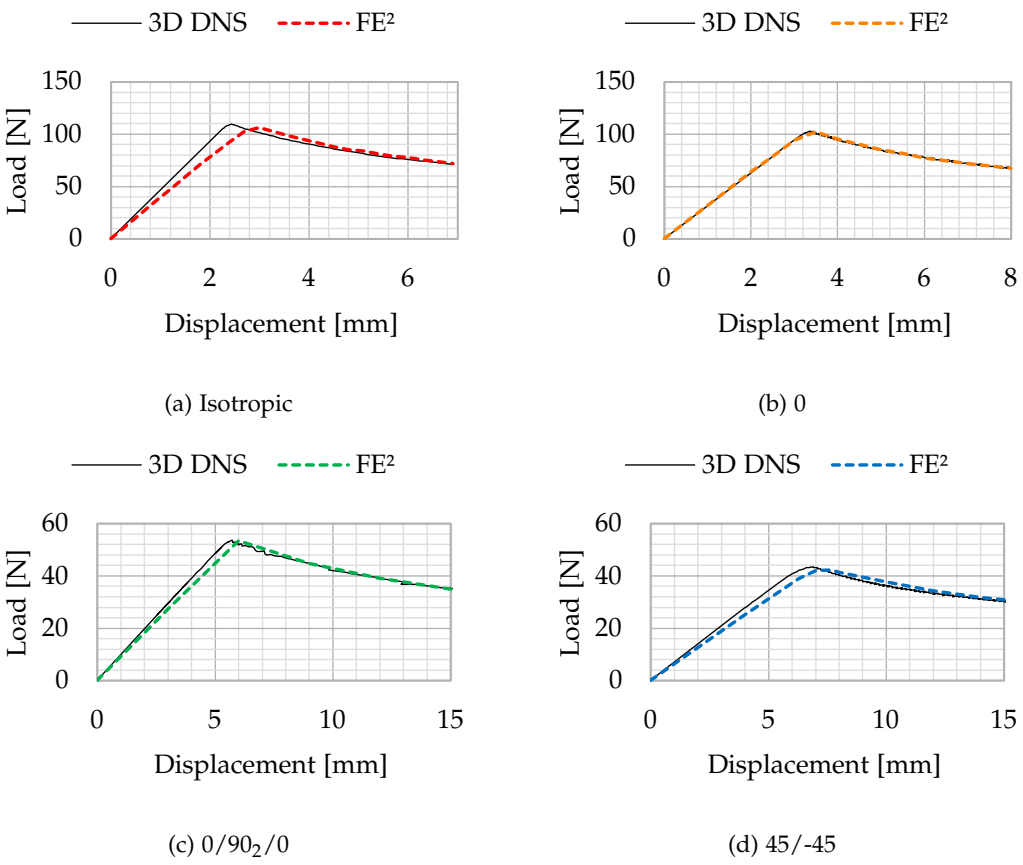

(a) Isotropic

(b) 0

(c) $0/90_2/0$

(d) 45/-45

Figure 5.2.: Load-displacement graphs for DCB Tests with different ply configurations with a pre-crack

5.3. Concluding Remarks

The multiscale framework presented in Section 4.1 has been tested following the ASTM standards for DCB Tests. Mesh configurations for the macro- and mesoscales are determined following the sensitivity studies presented in Appendix A. Again, the FE^2 analyses show great results when compared to those of the 3D DNS analyses. Another significant advantage can be found for the multiscale framework.

The FE^2 analyses show much better convergence properties due to the application of Mindlin-Reissner shell elements. Due to the element aspect ratio, many more elements are neces-

sary in 3D analyses, especially when analysing relatively thin structures. The cRVE on the mesoscale, however, can employ many elements over the thickness of the structure without needing to refine the macroscale mesh. Fewer elements will be necessary on the macroscale for the in-plane directions.

6. Conclusion

This thesis explored the applicability of a multiscale framework for delamination in composite laminates. A multiscale framework adopting the method of computational homogenisation has been developed for the modelling of delamination in composite laminates and has been tested for Mindlin-Reissner shell models. RVEs and cRVEs are coupled to shell and SIFS elements to determine the constitutive relation of the model. By applying a shell model instead of 3D solid elements, computational time can be greatly reduced due to the significant reduction in the necessary number of elements. Coupling a multiscale framework to this shell model can also greatly reduce computational time for applications with highly complex and non-linear material models.

First, 3D RVEs are coupled to the integration points of Mindlin-Reissner shell elements. On the mesoscale, the RVEs contain the material properties of the ply configuration. Results in this work show exact values for extension-related stiffness matrix components; however, this is not the case for the bending- and shear-related stiffness matrix components. The bending- and shear-related stiffness matrix components do converge towards the exact value when refining the mesoscale mesh and reducing the width of the RVEs. A narrow RVE is necessary for accurate results. An RVE was applied with a height of 8 mm and widths of 0.05 mm, resulting in a height-to-width ratio of 160. Applying this ratio gave accurate results.

In this work, heterogeneous materials consisting of composite laminates with different ply configurations are applied. These laminates consist of plies with orthotropic material properties and different ply orientations. Based upon the results of this work, applying a heterogeneous material at the mesoscale shows similar results as those for a homogeneous or isotropic material at the mesoscale. However, in some heterogeneous material cases, the stiffness matrix can have components related to the coupling of extension and bending. These components show exact values when refining the mesh or reducing the width of the RVE. Applying a heterogeneous material does not affect the multiscale framework differently than a homogeneous material.

When introducing a delamination to the framework, cRVEs are applied at the mesoscale. These cRVEs contain the material properties of the ply configuration and of the interface for the delamination. Each ply is modelled with continuum elements. The continuum elements describe the deformation of the plies. In between each ply, interface elements are applied. These interface elements describe the delamination in the cRVE.

Based on the results of this work, accurate results can be obtained when implementing delamination in the framework. The Unit Tests showed fairly accurate but non-exact results. This is due to the proposed boundary conditions on the cRVE not conforming to the Hill-Mandel macro-homogeneity principle. The normal jump is imposed as a linear boundary condition only applied to the two duplicated interface nodes in the middle of the cRVE. Therefore, the macroscopic normal jump is not equal to the volume average of the mesoscopic normal jump over the cRVE, resulting in slightly less accurate results. However, for the Unit Tests, the difference in results is negligible and only results in a slightly lower initial

dummy stiffness. The other load cases also show fairly accurate results, with the exception of the DCB Test without a pre-crack. However, the lack of accuracy of the results of the DCB Test without a pre-crack compared to the 3D DNS is not due to the mesoscopic behaviour but to the macroscopic behaviour. The multiscale framework applies Mindlin-Reissner shell elements, which have their own set of limitations compared to a 3D DNS. Different kinematic assumptions are made that influence the results of the analyses. When applying Mindlin-Reissner shell elements, the assumption is made that the vertical displacement over the height of the shell does not change. This is not the case for 3D solid elements. The shear stiffness and height of the shell have an influence on the vertical displacement over the height. Materials with lower shear stiffness or taller heights can experience a relatively large local deformation over the height of the shell. This displacement is constrained for shell elements, resulting in higher stiffness in the analysis. For load cases where this different kinematic assumption is negligible, the results of the multiscale framework will be quite accurate compared to the 3D DNS.

Finally, the major advantages and disadvantages of modelling the delamination of composites in a multiscale framework in comparison with monoscale DNS modelling are explored. The biggest advantage of modelling the delamination of composites in a multiscale framework in comparison with 3D DNS modelling is the expected computational time. Applying the multiscale framework instead of 3D DNS modelling can greatly reduce the time necessary to compute analyses. For complex ply configurations, this is even more so, as many elements will be necessary to describe the ply configuration over the height of the structure. For 3D analyses, this, in turn, will result in a large number of elements over the lengths of the structure as well, as a proper aspect ratio for the elements needs to be ensured. Additionally, for complex load cases and complex ply configurations, the FE^2 analyses in this work also show greater convergence properties. The FE^2 analyses were able to converge using large time steps with the displacement control method, whereas some of the 3D DNS analyses were not able to converge with this method.

A disadvantage of the multiscale framework in comparison to 3D DNS modelling is the extra expected memory necessary to run the analyses. For each element in the multiscale framework, an FE analysis is computed per time or load step, whereas the 3D DNS model only has one single FE analysis per time step. Due to this disadvantage, this work mostly applied unrealistic dimensions to the structures for the load cases. A supercomputer will be necessary to perform analyses for large shells. This is, however, also the case for 3D DNS analyses, due to the necessary computational power. Furthermore, a thin RVE or cRVE needs to be applied for accurate results. Considering that a proper aspect ratio needs to be applied for the elements in the RVE, this means that quite a lot of elements are necessary over the height of the cRVE. Lastly, a minor disadvantage of the multiscale framework in comparison with 3D DNS modelling is the limitation of the Mindlin-Reissner shell model on the macroscale. By applying Mindlin-Reissner shell elements, certain deformations in the model are constrained. This is, however, only for a few load cases.

Future Perspective

Although this work presents a viable multiscale framework for delamination in composite laminates, a number of subjects remain unresolved. The following propositions are made that could improve the accuracy and future extension of the multiscale framework:

cRVE Width The multiscale framework is limited by the cRVE width. A sufficiently narrow cRVE needs to be applied to obtain accurate results due to the influence of the width of the cRVE on the bending- and shear-stiffness matrix components. However, when applying a narrow cRVE and the proper aspect ratio of the elements of the cRVE, a lot of elements

are required over the height of the cRVE, resulting in more computational time and power necessary to perform the analyses. Different approaches, such as *Variationally Consistent Homogenisation* or the use of the *Irving-Kirkwood Theory*, could resolve the cRVE width dependency, resulting in fewer elements in the cRVEs and therefore less computational time and power.

cRVE Boundary Conditions Currently, the applied boundary conditions on the cRVE do not satisfy the Hill-Mandel macro-homogeneity principle. However, this was necessary to allow for proper bending in the two cRVE parts. Perhaps different boundary conditions could be found that satisfy the Hill-Mandel principle but also allow for proper bending of the cRVE. Additionally, there could be a set of boundary conditions that also reduce or eliminate the width dependency of the cRVE.

Arc-Length Method Results in this work show that some delaminations induce snapback behaviour. To capture this snapback behaviour, implementation of the arc-length method could prove beneficial for the multiscale framework.

Multiple Delaminations Another extension to the multiscale framework is the introduction of multiple delaminations within a cRVE, meaning multiple delaminations over the height of a shell. The theory necessary to implement this step is already laid out in this work; however, instead of two Mindlin-Reissner shells on the macroscale, n shells should be applied. The same goes for the corresponding plies within the cRVE.

Dynamic Loading and Machine Learning Finally, the last two steps for designing load protectors, defined in Section 1.2, need to be implemented to achieve the research goal, which is *to develop a numerical analysis tool for designing blast protectors made out of composite laminates*. These last two steps are the third and fourth steps. The third step is the implementation of dynamic loading, seeing as blast loads have a strong dynamic effect on the material. Optionally, the fourth step would be the introduction of Artificial Intelligence / Machine Learning to the framework to reduce computational time even more.

A. Additional Sensitivity Studies

A proper mesh size for the macro- and mesoscales needs to be determined for the DCB Tests in Chapter 5. Following the ASTM standards for Double-Cantilever Beams [2], a beam with a length of 140 mm, a width of 20 mm, and a height of 4 mm will be analysed. For simplicity's sake, the sensitivity studies for the macro- and mesoscale mesh and the RVE width will be performed on a cantilever beam in bending. Analyses will be performed for both the isotropic material model presented in Section 2.2 and the ply configurations presented in Section 3.1. First, a macroscale mesh sensitivity study is performed in Section A.1. This will be followed by a mesoscale mesh sensitivity study in Section A.2 and a width sensitivity study in Section A.3.

A.1. Macroscale Mesh Sensitivity Study

Similar mesh sensitivity studies on macro- and mesoscales, as in Section 2.3.1 and Section 2.3.2, are performed for the different ply configurations. On the macroscale, a beam with dimensions L_x = 100 mm, L_y = 20 mm, and h = 4 mm is discretized following the parameters from Table A.1. Again, MR_M is the *Macroscale Mesh Refinement* number as defined in Section 2.3.1, where doubling the MR_M results in doubling the number of elements in the x, y, and z directions.

Figure A.1 shows the results of the mesh refinement for the Mindlin-Reissner and 3D analyses for the ply configurations isotropic, 0, $0/90_2/0$, and 45/-45, respectively. The x-axis shows the Macroscale Mesh Refinement number, MR_M. The y-axis shows the load as a percentage of the load for the 3D analysis at MR_M = 4. All the analyses show a downward convergence of the force to the MR_M number, with the 3D analyses converging at a steeper rate. The analyses for the isotropic material and ply configuration 45/-45 show the largest deviations. To reduce computational time, a non-uniform mesh will be applied. A fine mesh will be employed at the start of the crack, whereas a rough mesh will be employed at the pre-crack and the clamp of the DCB. The macroscale mesh configuration is determined in Section 5.1.

	Variable	Value	Unit		Variable	Value	Unit
MR_M 1	$n_{elems,x}$	70	-	MR_M 4	$n_{elems,x}$	280	-
	$n_{elems,y}$	10	-		$n_{elems,y}$	40	-
	$n_{elems,z}$	4	-		$n_{elems,z}$	16	-
	d_x	2	mm		d_x	0.5	mm
	d_y	2	mm		d_y	0.5	mm
	d_z	1	mm		d_z	0.25	mm
	$n_{elems,T3}$	1,400	-		$n_{elems,T3}$	22,400	-
	$n_{elems,H8}$	2,800	-		$n_{elems,H8}$	179,200	-
MR_M 2	$n_{elems,x}$	140	-				
	$n_{elems,y}$	20	-				
	$n_{elems,z}$	8	-				
	d_x	1	mm				
	d_y	1	mm				
	d_z	0.5	mm				
	$n_{elems,T3}$	5,600	-				
	$n_{elems,H8}$	22,400	-				

Table A.1.: Macroscale mesh refinement parameters

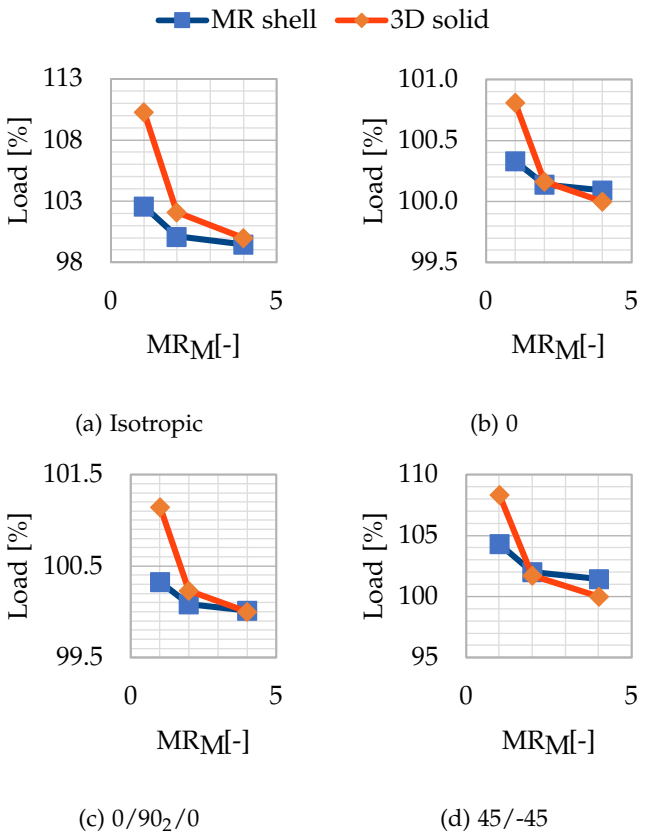

(a) Isotropic (b) 0

(c) $0/90_2/0$ (d) 45/-45

Figure A.1.: Load-MR_M number for the macroscale mesh refinement with different ply configurations

A.2. Mesoscale Mesh Sensitivity Study

For the mesoscale mesh refinement, the MR_M number of the macroscale is set at $MR_M = 1$, so 70 elements in the x-direction and 10 elements in the y-direction. RVEs with dimensions $L_x = L_y = 0.5$ mm and h = 4 mm will be discretized following the parameters from Table A.2. The aspect ratio for the height-to-width ratio of the elements within the RVE is set at 4. Now, MR_m is the *Mesoscale Mesh Refinement* number for the mesoscale mesh.

Figure A.2 shows the results of the mesoscale mesh refinement compared to the Mindlin-Reissner shell analyses for the different ply configurations. The x-axis shows the Mesoscale Mesh Refinement number, MR_m. The y-axis shows the load as a percentage of the load for the Mindlin-Reissner analysis at $MR_M = 1$. Similar results can be observed for the mesoscale mesh refinement in Section 2.3.2 and Section 3.3.2. The load-to-MR_m number properly converges downward; however, it sometimes converges to a value below the exact value.

Figure A.3 shows the non-zero, non-exact, normalised components of the stiffness matrix for the ply configurations. Again, the results are similar to those in Section 2.3.2 and Section 3.3.2. Bending stiffness components converge to the exact value, whereas shear stiffness components converge to a lower value.

As proven in Section 4.3, the number of elements in the x and y directions does not significantly contribute to the accuracy of the analyses. Therefore, RVEs with two elements in the x and y directions will be employed. The mesoscale mesh configuration is determined in Section 5.1.

	Variable	Value	Unit
MR_m 1	$n_{elems,x\&y}$	2	-
	$n_{elems,z}$	4	-
	$d_{x\&y}$	0.25	mm
	d_z	1	mm
	$n_{elems,H8}$	16	-
MR_m 2	$n_{elems,x\&y}$	4	-
	$n_{elems,z}$	8	-
	$d_{x\&y}$	0.125	mm
	d_z	0.5	mm
	$n_{elems,H8}$	128	-
MR_m 4	$n_{elems,x\&y}$	8	-
	$n_{elems,z}$	16	-
	$d_{x\&y}$	0.0625	mm
	d_z	0.25	mm
	$n_{elems,H8}$	1,024	-

Table A.2.: Mesoscale mesh refinement parameters

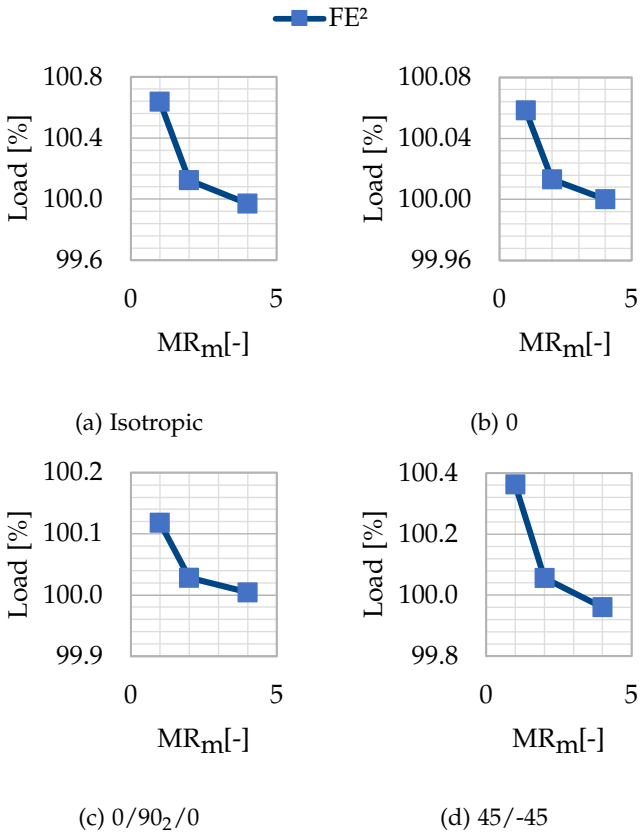

(a) Isotropic (b) 0

(c) $0/90_2/0$ (d) 45/-45

Figure A.2.: Load-MR_m number for the mesoscale mesh refinement with different ply configurations

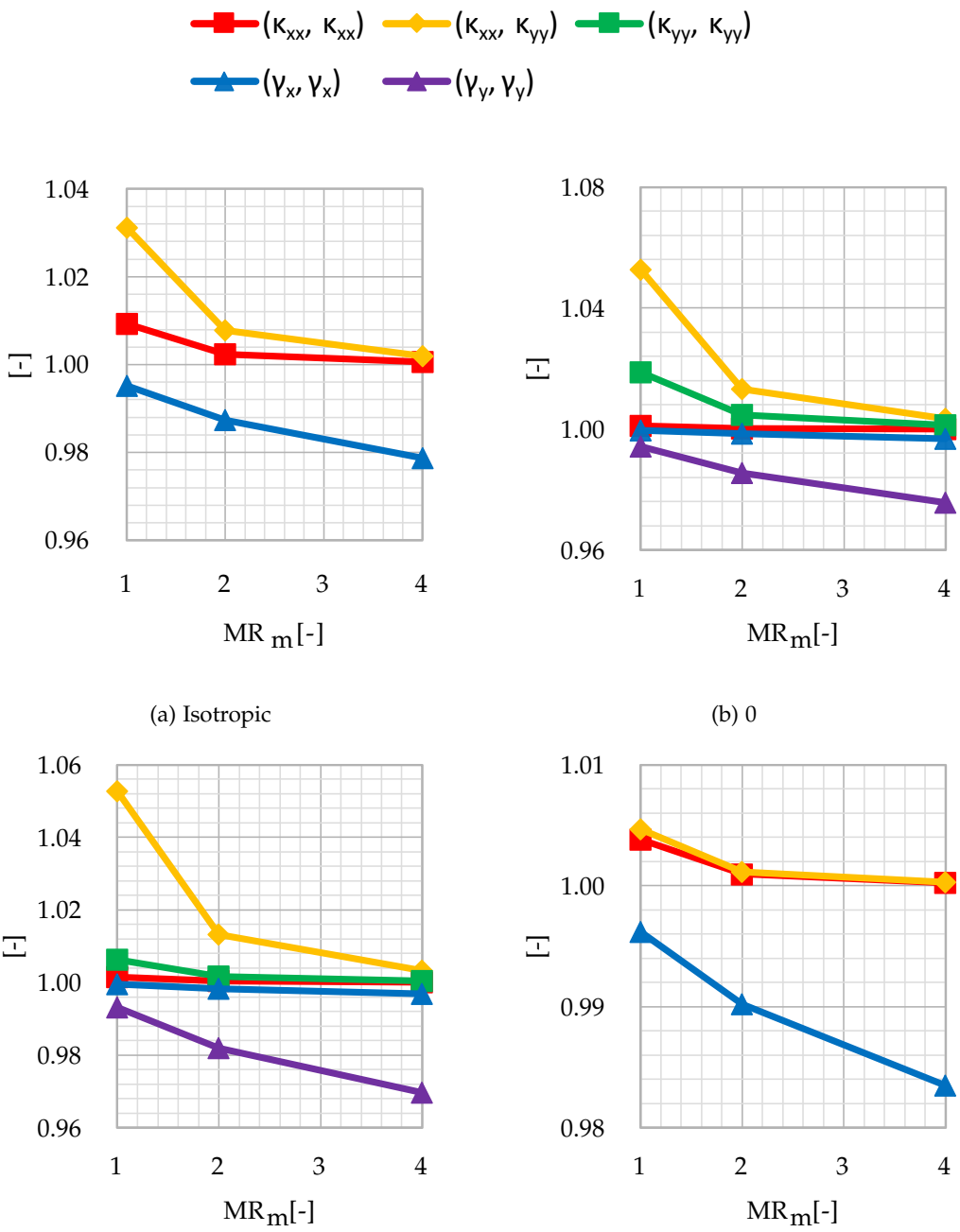

(a) Isotropic

(b) 0

(c) $0/90_2/0$

(d) 45/-45

Figure A.3.: Normalised stiffness matrix components with corresponding MR_m number

A.3. RVE Width Sensitivity Study

The influence of the width of the RVE is explored. A fixed number of elements in the x and y directions is applied: $n_{elems,x\&y} = 2$. An aspect ratio for the height-to-width ratio of 4 is employed. *WR* is the *Width Refinement* number, where doubling the WR results in halving the element size in the x and y directions. On the macroscale, the same MR_M number is applied as for the mesoscale mesh refinement: $MR_M = 1$. Table 2.4 shows the RVE width refinement parameters.

	Variable	Value	Unit		Variable	Value	Unit
WR 1	RVE_{width}	0.5	mm	WR 8	RVE_{width}	0.0625	mm
	$n_{elems,x\&y}$	2	-		$n_{elems,x\&y}$	2	-
	$n_{elems,z}$	4	-		$n_{elems,z}$	32	-
	$d_{x\&y}$	0.25	mm		$d_{x\&y}$	0.03125	mm
	d_z	1	mm		d_z	0.125	mm
	$n_{elems,H8}$	16	-		$n_{elems,H8}$	128	-
WR 2	RVE_{width}	0.25	mm	WR 16	RVE_{width}	0.03125	mm
	$n_{elems,x\&y}$	2	-		$n_{elems,x\&y}$	2	-
	$n_{elems,z}$	8	-		$n_{elems,z}$	64	-
	$d_{x\&y}$	0.125	mm		$d_{x\&y}$	0.015625	mm
	d_z	0.5	mm		d_z	0.0625	mm
	$n_{elems,H8}$	32	-		$n_{elems,H8}$	256	-
WR 4	RVE_{width}	0.125	mm				
	$n_{elems,x\&y}$	2	-				
	$n_{elems,z}$	16	-				
	$d_{x\&y}$	0.0625	mm				
	d_z	0.25	mm				
	$n_{elems,H8}$	64	-				

Table A.3.: RVE width refinement parameters

Figure A.4 shows the results of the RVE width refinement compared to the Mindlin-Reissner shell analyses. The x-axis now shows the Width Refinement number, WR. The y-axis again shows the load as a percentage of the load of the Mindlin-Reissner analysis at $MR_M = 1$. As expected, the load-to-WR number converges downward to the exact value.

Figure A.5 shows the non-zero, non-exact, normalised stiffness matrix components for the different ply configurations. The results are again similar to those of Section 2.3.3 and Section 3.3.3. Stiffness matrix components related to bending all converge downwards, whereas stiffness matrix components related to shear converge upwards to the exact values.

Due to the width dependence of the RVE, a sufficiently narrow RVE needs to be employed. This width of the RVE should have a proper ratio with the height. A width of 0.025 mm will be employed for the cRVE in Chapter 5.

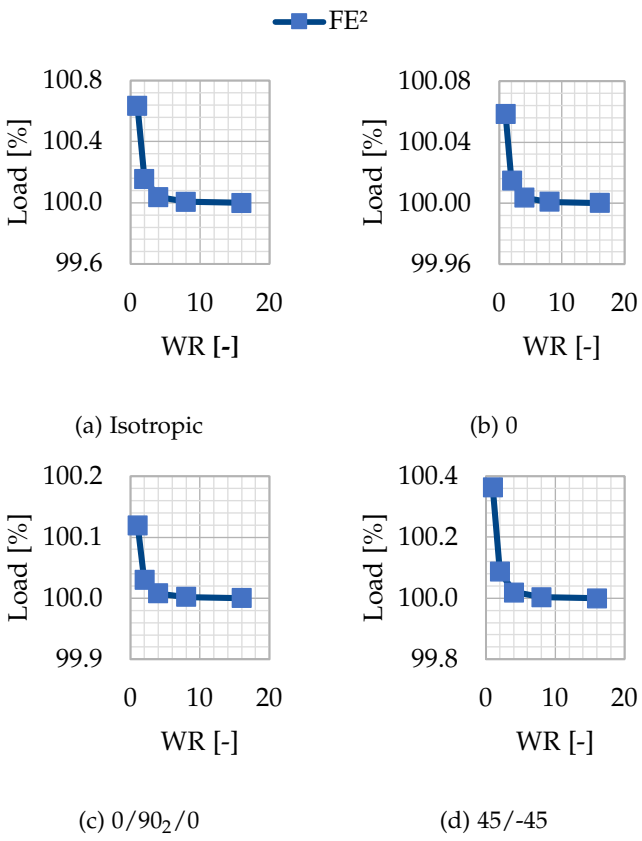

(a) Isotropic (b) 0

(c) $0/90_2/0$ (d) 45/-45

Figure A.4.: Load-WR number with different ply configurations

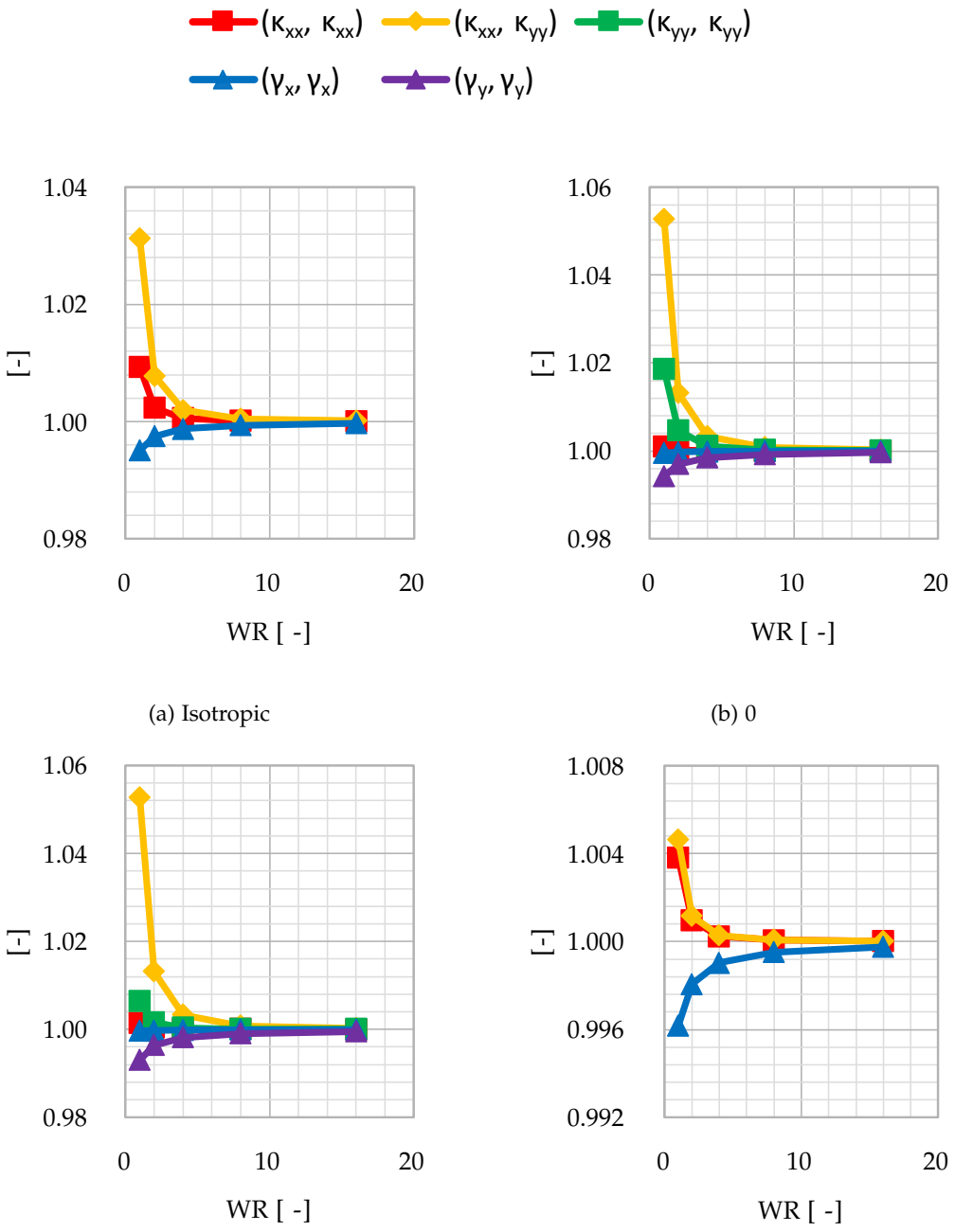

(a) Isotropic

(b) 0

(c) $0/90_2/0$

(d) 45/-45

Figure A.5.: Normalised stiffness matrix components with corresponding WR number

Bibliography

[1] ASTM (2019). Standard test method for determination of the mode ii interlaminar fracture toughness of unidirectional fiber-reinforced polymer matrix composites. Technical report, ASTM.

[2] ASTM (2022). Standard test method for mode i interlaminar fracture toughness of unidirectional fiber-reinforced polymer matrix composites. Technical report, ASTM.

[3] Benzeggagh, M. L. and Kenane, M. (1996). Measurement of mixed-mode delamination fracture toughness of unidirectional glass/epoxy composites with mixed-mode bending apparatus. *Composites Science and Technology*, 56(4):439–449.

[4] Bornstein, H. and Ackland, K. (2013). Evaluation of energy absorbing materials under blast loading. *WIT Transactions on Energy Sciences*, 77:125–136.

[5] Börjesson, E., Larsson, F., Runesson, K., Remmers, J. J. C., and Fagerström, M. (2023). Variationally consistent homogenisation of plates. *Computer Methods in Applied Mechanics and Engineering*, 413.

[6] Daniel, I. M. and Ishai, O. (2006). *Engineering Mechanics of Composite Materials*. Oxford University Press.

[7] Gruttmann, F. and Wagner, W. (2013). A coupled two-scale shell model with applications to layered structures. *International Journal for Numerical Methods in Engineering*, 94(13):1233–1254.

[8] Herwig, T. and Wagner, W. (2018). On a robust fe2 model for delamination analysis in composite structures. *Composite Structures*, 201:597–607.

[9] Hii, A. K. W. and El Said, B. (2022). A kinematically consistent second-order computational homogenisation framework for thick shell models. *Computer Methods in Applied Mechanics and Engineering*, 398.

[10] Kaczmarczyk, , Pearce, C. J., and Bićanić, N. (2007). Scale transition and enforcement of rve boundary conditions in second-order computational homogenization. *International Journal for Numerical Methods in Engineering*, 74(3):506–522.

[11] Kania, E. (2009). Developmental tendency of landmine protection in vehicle. *Modelling and Optimization of Physical Systems*.

[12] Kanouté, P., Boso, D. P., Chaboche, J. L., and Schrefler, B. A. (2009). Multiscale methods for composites: A review. *Archives of Computational Methods in Engineering*, 16(1):31–75.

[13] Krueger, R., Deobald, L., and Gu, H. (2020). A benchmark example for delamination growth predictions based on the single leg bneding specimen under fatigue loading. *Advanced Modeling and Simulation in Engineering Sciences*, 7(11).

[14] Müller, M., Klarmann, S., and Gruttmann, F. (2022). A new homogenization scheme for beam and plate structures without a priori requirements on boundary conditions. *Computational Mechanics*, 70:1167–1187.

[15] Nguyen, V. P. (2011). *Multiscale Failure Modelling of Quasi-Brittle Materials*. PhD thesis, Delft University of Technology.

[16] Oddy, C. and Bisschop, R. (2017). Multiscale modelling of heterogeneous beams. Master's thesis, Chalmers University of Technology.

[17] Ramasamy, A., Hill, A. M., Hepper, A. E., Bull, A. M. J., and Clasper, J. C. (2009). Blast mines: Physics, injury mechanisms and vehicle protection. *Journal of the Royal Army Medical Corps*, 155(4):258–264.

[18] Reddy, J. N. (2003). *Mechanics of Laminated Composite Plates and Shells*. CRC Press.

[19] Rocha, I. B. C. M. (2019). *Numerical and Experimental Investigation of Hygrothermal Aging in Laminated Composites*. PhD thesis, Delft University of Technology.

[20] Turon, A., Camanho, P. P., Costa, J., and Davila, C. G. (2005). A damage model for the simulation of delamination in advanced composites under variable-mode loading. *Mechanics of Materials*, 38(11):1072–1089.

[21] Van der Meer, F. P. (2010). *Computational Modeling of Failure in Composite Laminates*. PhD thesis, Delft University of Technology.

[22] Van der Meer, F. P. and Sluys, L. (2010). Mesh-independent modeling of both distributed and discrete matrix cracking in interaction with delamination in composites. *Engineering Fracture Mechanics*, 77(4):719–735.

[23] Wieringa, F. (2022). Multiscale finite element framework for delamination in composite laminates. Master's thesis, Delft University of Technology.

Colophon

This document was typeset using LaTeX, using the KOMA-Script class `scrbook`. The main font is Palatino.